Gao *et al. Chem. Synth.* **2025**, *5*, 22
**DOI:** 10.20517/cs.2024.96

**Chemical Synthesis**

**Review**

**Open Access**

# Selective heterogeneous photocatalytic activation for toluene oxidation: recent advances, challenges and perspective

**Shiqin Gao[1], Lisu Bai[1], Tao Gan[2,*], Bolun Wang[1,*]**

[1]State Key Laboratory of Inorganic Synthesis and Preparative Chemistry, College of Chemistry, Jilin University, Changchun 130012, Jilin, China.
[2]Shanghai Synchrotron Radiation Facility, Shanghai Advanced Research Institute, Chinese Academy of Sciences, Shanghai 201204, China.

[*]**Correspondence to:** Dr. Bolun Wang, State Key Laboratory of Inorganic Synthesis and Preparative Chemistry, College of Chemistry, Jilin University, 2699 Qianjin Street, Changchun 130012, Jilin, China. E-mail: wangbolun@jlu.edu.cn; Dr. Tao Gan, Shanghai Synchrotron Radiation Facility, Shanghai Advanced Research Institute, Chinese Academy of Sciences, Shanghai, 239 Zhangheng Road, Shanghai 201204, China. E-mail: gant@sari.ac.cn

**How to cite this article:** Gao, S.; Bai, L.; Gan, T.; Wang, B. Selective heterogeneous photocatalytic activation for toluene oxidation: recent advances, challenges and perspective. *Chem. Synth.* **2025**, *5*, 22. https://dx.doi.org/10.20517/cs.2024.96

**Received:** 13 Aug 2024 **First Decision:** 25 Oct 2024 **Revised:** 13 Nov 2024 **Accepted:** 19 Nov 2024 **Published:** 8 Feb 2025

**Academic Editor:** Feng Shi **Copy Editor:** Pei-Yun Wang **Production Editor:** Pei-Yun Wang

## Abstract

The conversion of toluene into high-value products without generating undesired $CO_2$ remains a critical challenge. Selective oxidation of toluene under visible light irradiation has emerged as a promising solution. This review offers a comprehensive interpretation of photocatalytic transformations in heterogeneous toluene oxidation. We start by outlining the basic mechanism of C–H bond activation of toluene and provide an overview of reactive oxygen species (ROS) within photocatalytic systems. Subsequently, we provide a summary of strategies that have been developed to enhance the conversion and selectivity of the heterogeneous photocatalytic system. Following this, advanced characterization techniques and density functional theory (DFT) calculations are discussed for understanding the structure-performance relationship of photocatalysts and the mechanisms underlying photocatalytic processes. Finally, we put forward a detailed discussion of current challenges and potential directions for future research, with the aim of offering valuable insights for this emerging field. We believe that this review will not only spark greater creativity in optimizing photocatalysts but also offer valuable insights for designing other C–H bond activation systems.

**Keywords:** Photocatalysis, toluene oxidation, C–H bond activation, benzaldehyde

## INTRODUCTION

Volatile organic compounds (VOCs) are organic chemicals with boiling points between 50 and 260 °C under atmospheric pressure (101.325 kPa), most of which are highly toxic and carcinogenic[1]. These compounds are primarily emitted from transportation, fuel combustion, industrial processes, and household activities, posing significant threats to the environment and human health even at very low concentrations. Toluene, a representative VOC component, has long been recognized as the most abundant and hazardous aromatic VOC worldwide, and its elimination is of great significance in reducing air pollution and ensuring human health[2]. Therefore, effective technologies must be developed to remove the toxic toluene from contaminated gas streams, enhancing the ambient air quality and safeguarding human health. To date, numerous studies and reviews have focused on the capture and/or direct decomposition of these hazardous molecules into harmless products (i.e., $CO_2$ and $H_2O$), aiming to control the inflow of toluene into the environment. To this end, various methods have been developed, including adsorption and condensation technology[3-7], photocatalytic oxidation technology[8-12], thermal-based catalytic oxidation technology[13-15], and non-thermal plasma-assisted catalytic technology[1,16-18]. Among them, catalytic oxidation stands out as a reliable and effective technology capable of converting pollutants into carbon dioxide and water in the presence of heat or light. While photocatalytic oxidation offers a promising, energy-saving approach for VOC degradation by using inexhaustible solar energy, its significant greenhouse gas production presents challenges for the widespread adoption of the technology, particularly in the context of the current climate crisis. Addressing this, the conversion of toxic toluene into high-value-added products without generating undesired $CO_2$ remains a critical consideration, and the selective oxidation of toluene into benzaldehyde under visible light irradiation has emerged as a viable solution in this context[19].

Benzaldehyde, the simplest aromatic aldehyde found in nature, is valued for its diverse applications including dyes, perfumes, pharmaceuticals, preservatives, plasticizers, and the food industry, holding significant importance in chemical markets[20,21]. Natural benzaldehyde, commonly found in products such as bitter almonds, apricot kernels, peaches, and prunes, can be released by enzymatic hydrolysis, accompanied by the production of a toxic by-product hydrogen cyanide, contributing to approximately 1.5% of the total annual world benzaldehyde production[22,23]. It is evident that natural sources are insufficient to meet the ever-increasing market demand. Therefore, synthesizing benzaldehyde on a large scale is imperative to meet the requirements of the global market, which exceeded 170,000 tons in 2022 and is forecasted to surpass 240,000 tons by 2032. Currently, benzaldehyde is primarily obtained under harsh conditions through two methods: (i) liquid-phase chlorination of toluene followed by hydrolysis; and (ii) vapor/liquid-phase direct oxidation of toluene[24]. The former route can yield large amounts of benzaldehyde; however, it suffers from several problems, including multiple steps and the use of environmentally unfriendly chlorine, resulting in equipment corrosion and organochlorine residues that limit its application in food and medicine, as well as significant environmental pollution from the discharge of large amounts of wastewater[25]. The direct vapor/liquid-phase oxidation of toluene, while considered as an alternative to producing benzaldehyde, generally results in the formation of a large amount of $CO_2$ and several oxygenated by-products due to the high temperatures and pressures required, necessitating limited toluene conversion to avoid the over-oxidation towards benzoic acid or $CO_2$[26].

In this context, research into photocatalytic toluene oxidation presents a highly selective, industrially available, and environmentally benign pathway for benzaldehyde production, utilizing dioxygen molecules as a green oxidant[27-29]. The mild reaction conditions (room temperature and atmospheric pressures) employed in photocatalytic processes not only effectively avoid the occurrence of side reactions but also mitigate the challenges commonly encountered in thermal catalysis, which often demand stringent reaction conditions to drive the reaction forward, unavoidably posing challenges to the equipment and leading to the

formation of unwanted by-products[30]. For example, the gas-phase oxidation of toluene typically occurs at temperatures ranging from 300 to 700 °C in the presence of suitable catalysts (primarily Ti/V/Mn-based oxide catalysts), along with oxygen and an inert gas[31-33]. To enhance the stability and selectivity of the system, elevated pressures are applied, and potassium sulfate is introduced within the thermal reactor. Despite substantial effort devoted to optimizing the process over the years, the conversion of toluene remains relatively low at approximately 15%, accompanied by the formation of multiple side products such as benzoic acid, carbon monoxide, and carbon dioxide, which not only reduce the efficiency of the reaction but also complicate the purification process, limiting the industrial viability of the method. In contrast, photocatalysis can trigger the dissociation of the sluggish C($sp^3$)–H bond within toluene at ambient temperature, substantially mitigating the generation of $CO_2$, ensuring high selectivity while maintaining suitable toluene conversion[34,35]. More recently, Shi *et al.* achieved remarkable success in photocatalytic toluene oxidation at room temperature using a Ni-doped monolayer $Bi_2WO_6$ (BWO) photocatalyst, which afforded a high toluene conversion rate of 4,560 $\mu mol \cdot g^{-1} \cdot h^{-1}$ and an impressive selectivity (> 90%) towards benzaldehyde, highlighting the potential of the photocatalytic method for efficient and selective benzaldehyde production[36].

Compared to homogeneous photocatalytic toluene oxidation systems, heterogeneous systems offer several advantages, including enhanced stability, ease of catalyst recovery, and improved efficiency in the photooxidation of toluene. In a typical heterogeneous photocatalytic toluene oxidation system [Scheme 1], the rational design of a photocatalyst lies at the core, influencing both the conversion of the substrates and the selectivity towards targeted aromatic benzaldehyde. Key factors to consider in photocatalyst design include the ability to adsorb $O_2$ and toluene molecules, optimal band gap structures, efficient light absorption, and the effective separation and transfer of photogenerated charge carriers[37-41]. Over the past decade, significant effort has been devoted to the study of photocatalytic toluene oxidation, with a primary focus on its complete degradation into carbon dioxide and water, treating toluene molecules as typical contaminants, resulting in a number of comprehensive reviews that highlight the advancements and growing interest in this field[28,29,42-46]. Given the recent surge in the discovery of novel photocatalysts and advancements in the selective photocatalytic oxidation of toluene to benzaldehyde, there is a pressing need for a critical review to guide the next step of research and development. In this timely review, we begin by outlining the basic mechanism of C–H bond activation of toluene and provide an overview of reactive oxygen species (ROS) commonly generated *in situ* within photocatalytic systems. Subsequently, we will provide a comprehensive summary of strategies that have been developed to date to enhance the conversion and selectivity of the photocatalytic system, including heterojunction construction, control of crystal facets and sizes, single-atom catalyst (SAC) fabrication, defect engineering, heteroatom doping, and novel photocatalyst design, aiming to elucidate the photocatalyst design protocols that will guide future development towards a low-cost, high-efficiency benzaldehyde synthesis system. Following this, advanced characterization techniques and density functional theory (DFT) calculations are discussed for understanding the structure-performance relationship of photocatalysts and the mechanisms underlying photocatalytic processes. Finally, we put forward a detailed discussion of current challenges and potential directions for future research, with the aim of offering valuable insights for this emerging field.

## PHOTOCATALYTIC MECHANISMS OF C–H BOND ACTIVATION

It is widely acknowledged that the cleavage of inert C($sp^3$)–H bonds in toluene [bond dissociation energy (BDE) = 88.5 ± 1.5 $kcal \cdot mol^{-1}$], affording hydrocarbon radicals as intermediates, represents the initial and rate-determining step in the photocatalytic activation of toluene[47-50]. In addition, understanding the efficiency of C–H bond activation by photogenerated holes and various ROS generated over the surface of distinct photocatalysts is critical for evaluating the overall performance of the photocatalytic system[51-55]. In

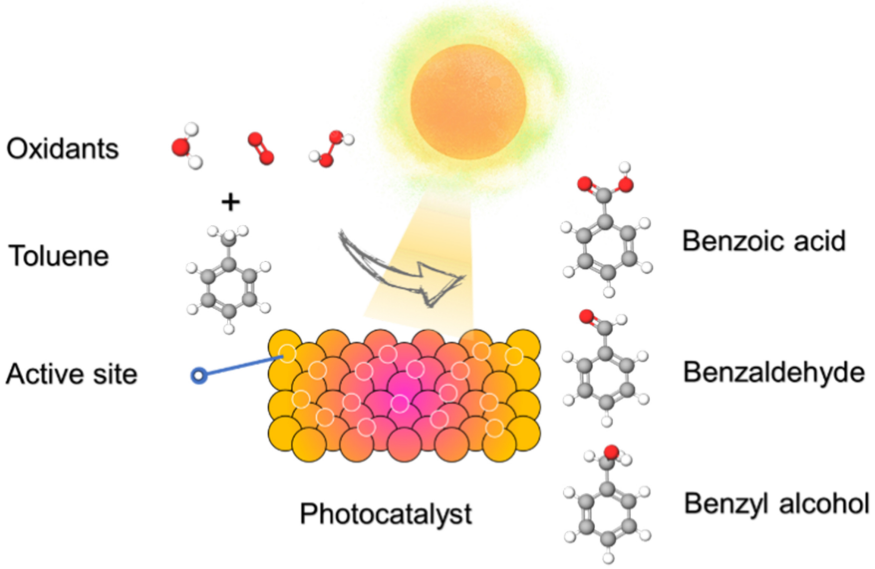


**Scheme 1.** The selective photooxidation of toluene over certain photocatalysts under light irradiation.

terms of the selectivity of the photocatalytic toluene conversion reaction, investigating the formation and properties of various ROS is of paramount significance. These highly reactive species are considered as the primary oxidants in photooxidation reactions, and a detailed understanding of their behavior can provide crucial insights for further optimizing the selectivity towards targeted benzaldehyde during photocatalysis. In this section, in regard to recent advances in heterogeneous photocatalytic toluene conversion systems, the mechanisms of C($sp^3$)–H bond dissociation and the behavior of various ROS species under light irradiation are detailed and discussed.

### Oxidation of toluene with photogenerated holes

During a typical photocatalytic process, the activation of inert C–H bonds can proceed through multiple mechanisms, with the direct involvement of photogenerated holes being particularly crucial[56-58]. When the photocatalyst is exposed to an appropriate light source, it could absorb photons with energy equal to or greater than its band-gap energy, resulting in the generation of photogenerated electrons and holes, where the electrons in the valence band of the semiconductor photocatalyst are excited into the conduction band (CB), leaving behind photogenerated holes in the valence band[59]. The photogenerated holes, with strong oxidative capability, can directly activate the C($sp^3$)–H bond in toluene molecules, resulting in the formation of benzyl radicals. Generally, toluene is trapped by photogenerated holes and the C($sp^3$)–H bond undergoes homolytic cleavage, leading to the formation of a benzyl radical and the concurrent generation of a proton. During the cleavage process of C($sp^3$)–H bonds, the toluene can be oxidized by a photogenerated hole into a benzyl radical and a proton. The obtained carbon radicals can rapidly interact with $O_2$, $^{\bullet}O_2^-$, or other ROS species, ultimately affording a series of oxygenated products, including benzyl alcohol, benzaldehyde, and benzoic acid. For example, Xue *et al.* synthesized $TiO_2$ supported single-atom yttrium photocatalyst for the selective photooxidation of toluene[60]. In comparison to pristine $TiO_2$, on which the generated benzaldehyde would be overoxidized by excess $^{\bullet}O_2^-$ to form benzoic acid and $CO_2$, resulting in poor selectivity towards benzaldehyde, the as-prepared $Y_1/TiO_2$ demonstrates a lattice oxygen-mediated mechanism for the selective oxidation of toluene molecules. It was revealed that the surface lattice $O^{2-}$ species could directly react with benzyl radicals to produce benzaldehyde. Moreover, benzaldehyde molecules would quickly desorb from the catalyst surface, effectively preventing the overoxidation of benzaldehyde to the benzoic acid and $CO_2$, thereby leading to superior photocatalytic performance in the selective toluene oxidation.

### Oxidation of toluene with superoxide radicals

When $O_2$ is employed within the photocatalytic system, it undergoes various transformation processes to form reactive ROS, which serve as primary oxidants for toluene oxidation[61]. One of the typical ROS is the superoxide ion radical, which is a radical anion[62]. In typical photocatalytic systems, photocatalysts with a CB edge level more negative than the $O_2/^{\bullet}O_2^-$ potential could deliver one photoactivated electron to the $\pi^*$ orbitals of oxygen molecules via the reduction pathway, thereby generating superoxide radicals [Equation (1)]. As a highly reactive oxidant, $^{\bullet}O_2^-$ could directly initiate the cleavage of C–H bonds or combine with the generated hydrocarbon radicals during the oxidation process to complete the photocatalytic cycle[35]. For instance, $^{\bullet}O_2^-$ could be generated over the as-prepared photochromic $Bi_2WO_{6-x}$/amorphous BiOCl (*p*-BWO) photocatalysts through two distinct pathways: (1) Direct reduction of oxygen molecules by photogenerated electrons from *p*-BWO, resulting in the formation of $^{\bullet}O_2^-$; and (2) photogenerated electrons initially captured by $[W_{(VI)}O_{6-x}]$, reducing the $W_{(VI)}$ to yield $W_{(V)}$, displaying photochromic phenomenon, which facilitates the separation of charge carriers. Subsequently, the obtained $W_{(V)}$ can be oxidized by $O_2$ to regenerate $W_{(VI)}$, accompanied by the generation of $^{\bullet}O_2^-$[47]. The obtained $^{\bullet}O_2^-$ subsequently combines with carbon radicals to form $C_6H_5CH_2OOH$ intermediates, ultimately yielding benzaldehyde as the main product.

$$O_2 + e^- \rightarrow {}^{\bullet}O_2^- \ [E^0 = -0.33 \text{ V } \textit{vs.} \text{ standard hydrogen electrode (SHE)}] \quad (1)$$

### Oxidation of toluene with hydroxyl radicals

Upon light irradiation, the adsorbed water molecules and the surface-bound hydroxyl groups on the photocatalysts could be oxidized by photogenerated holes, resulting in the generation of hydroxyl radical ($^{\bullet}OH$) [Equation (2)]. The obtained radicals subsequently interact immediately with the substrate molecules, further driving chemical reactions[63-66]. Although the mechanistic implications remain controversial, $^{\bullet}OH$ radicals are widely regarded as the most reactive species among all types of ROSs due to the powerful oxidative potential of the $^{\bullet}OH/H_2O$ pair, which allows for the facile dissociation of the inert chemical bond in the reactant molecules (e.g., methane, ethylbenzene, microplastics, *etc.*) and further converts them into highly value-added products[66-71]. However, given that the intermediates formed during photocatalysis are usually highly susceptible to overoxidation by $^{\bullet}OH$ radicals, which unavoidably leads to the nonselective oxidation of organic reactants into $CO_2$ and water, increasing attention has been paid to controlling the content of $^{\bullet}OH$ in the catalytic system and developing mild pathways for their production to improve the selectivity of targeted products while maintaining the conversion of reactant molecules. For example, Teng *et al.* investigated the mechanism of selective toluene oxidation using $Sb(CN)_3$-modified $sp^2$-c-COFs[48]. They revealed that the adsorbed water could be oxidized by the photogenerated holes to produce $^{\bullet}OH$ radicals, which would lead to the generation of benzyl alcohol. The generated benzyl alcohol can further react with benzaldehyde to form hemiacetal, catalyzed by Brönsted acid, which could be further oxidized to generate ester by the oxygen reduction reaction (ORR)-related ROS in the reaction system.

$$H_2O + h^- \rightarrow {}^{\bullet}OH + H^+ \ (E^0 = 2.38 \text{ V } \textit{vs.} \text{ SHE}) \quad (2)$$

### Oxidation of toluene with singlet oxygen species

Singlet oxygen ($^1O_2$), a reactive form of molecular oxygen with high energy and electrophilic properties, can be generated through the energy transfer from the triplet state of a photosensitizer to the ground state oxygen molecule ($^3O_2$) under light illumination, resulting in the formation of $^1O_2$ [Equations (3) and (4)][72-77]. Moreover, it has been proposed that the oxidation of $^{\bullet}O_2^-$ by photoactivated holes on suitable photocatalysts [e.g., $TiO_2$, ZnO, metal-organic frameworks (MOFs), covalent organic frameworks (COFs), polymers, and carbon-based nanomaterials] could also yield $^1O_2$ species [Equations (5) and (6)][78-82]. Effective heterogeneous photocatalysis using $^1O_2$ relies on satisfying two main criteria: (i) achieving efficient

photosensitization and (ii) ensuring adequate exposure of active sites within photocatalyst, which can be achieved through the construction of hierarchical pores within photocatalysts or by controlling the crystal dimensions and sizes of the photocatalysts, thereby facilitating rapid diffusion and transfer of reactants and products to and from catalytically active sites[83-87]. As a moderate oxidant, $^1O_2$ can effectively promote the oxidation of organic molecules while preventing overoxidation. For instance, Li *et al.* reported the interfacial synergy of Pd sites and defective oxygen sites within the as-prepared Pd/BiOBr photocatalysts could promote the selective photooxidation of toluene[88]. To investigate the ROS involved in the oxidation process, various scavengers [superoxide dismutase (SOD) to quench $^{\bullet}O_2^-$, carotene to quench $^1O_2$, catalase to quench $H_2O_2$, mannitol to quench $^{\bullet}OH$] were applied within the photocatalysis process. The results showed that when Pd/BiOBr was used as the photocatalyst, both $^{\bullet}O_2^-$ and $^1O_2$ were the major ROSs contributing to the selective production of benzaldehyde during the photocatalytic oxidation reaction. Furthermore, *in situ* electron spin resonance (ESR) detection using 2,2,6,6,-tetramethylpiperidine (TEMP) as a radical-trapping agent provided a more direct clue for the generation of $^1O_2$ during the reaction.

$$\text{Sensitizer} + h\nu \rightarrow \text{Sensitizer}^* \quad (3)$$

$$\text{Sensitizer}^* + O_2 \rightarrow \text{ROS} + \text{Sensitizer} \quad (4)$$

$$O_2 + e^- \rightarrow {}^{\bullet}O_2^- \ (E^0 = -0.33 \text{ V } \textit{vs.} \text{ SHE}) \quad (5)$$

$$^{\bullet}O_2^- + h^+ \rightarrow {}^1O_2 \ (E^0 = 2.53 \text{ V } \textit{vs.} \text{ SHE}) \quad (6)$$

The photocatalytic conversion of $O_2$ to ROS proceeds through complex pathways, such as energy transfer and electron transfer, and is influenced by the type of photocatalyst employed and the catalytic environment within the system[89-92]. Consequently, future efforts are expected to focus on the development of methods to control the $O_2$ activation process, aiming to achieve highly efficient and selective ROS generation. The selective generation of specific ROS is essential for understanding the underlying mechanisms and optimizing the performance and selectivity of photocatalytic systems, ensuring their effectiveness in various photocatalytic applications.

Although the specific reaction mechanism remains unclear, several key steps can be identified in the photocatalytic oxidation of toluene, providing readers with an overview of the photocatalytic mechanism: (i) Excitation of photocatalyst: Upon light irradiation, the photocatalyst absorbs photons, generating electron-hole pairs (i.e., $e^-/h^+$); (ii) Efficient charge separation: The photogenerated holes would trap the adsorbed toluene molecules, facilitating their activation; (iii) Homolytic cleavage of $C(sp^3)$–H bond: The reaction between the holes and the toluene molecules leads to the homolytic cleavage of $C(sp^3)$–H bond, resulting in the formation of benzyl radicals ($C_6H_5CH_2^{\bullet}$) and the release of protons ($H^+$); (iv) Reactivity of benzyl radicals: The generated benzyl radicals can react with various ROS generated in the photocatalytic system, such as hydroxyl ($^{\bullet}OH$) and superoxide radicals ($^{\bullet}O_2^-$), yielding a range of oxidation products, including benzyl alcohol, benzaldehyde, and benzoic acid; (v) Termination reactions: The overall reaction pathway may involve further reactions of benzyl radicals, leading to overoxidation products (e.g., CO and $CO_2$) depending on the specific reaction conditions and available ROS.

## MODIFICATIONS OF HETEROGENEOUS PHOTOCATALYSTS

In order to improve the photocatalytic activity of semiconductor photocatalysts employed in toluene photooxidation reactions, researchers have designed and adopted several modification strategies. Herein, we provide an overview on seven modification strategies, including heterojunction construction, crystal facet

engineering, crystal size control, SAC fabrication, defect engineering, heteroatom modification, *etc.*, to improve the photocatalytic efficiency. Herein, we summarized the photocatalytic performance of typical heterogeneous photocatalysts in recent publications, as listed in Supplementary Table 1.

### Heterojunction construction

To enhance the photocatalytic performance of a specific semiconductor material, two primary challenges must be noted and addressed: (i) the severe and rapid recombination of photogenerated charge carriers and (ii) the relatively long distance for charge carriers to migrate and transfer to reach the catalyst surface to activate the substrates[93,94]. In view of this, coupling two semiconductors with suitable band gaps to construct a heterostructure architecture is widely recognized as a promising strategy to shorten the diffusion length of charge carriers and prevent electron-hole recombination, thereby extending the lifetime of photogenerated charge carriers and enabling more timely and high-efficiency photocatalytic reactions[95-99]. Specifically, the quality of the interface within a heterostructure, such as contact area, chemical bonds, and interfacial electric fields (E-fields), determines the charge separation efficiency. In this section, we will discuss recent advances in the fabrication of various composite photocatalysts with well-designed heterostructures for the selective photooxidation of toluene.

In 2018, He *et al.* reported the synthesis of organic/inorganic $Cd_3(C_3N_3S_3)$/CdS [denoted $Cd_3(TMT)_2$/CdS] composite with typical porous structures and rich in heterostructures for the selective toluene photooxidation, synthesized via a facile hydrothermal procedure[100]. The *in situ* generation of porous CdS under elevated temperature offers abundant mesopores and macropores, enhancing the adsorption of reactants as the fabricated $Cd_3(TMT)_2$/CdS composite photocatalyst is used in the reaction systems. Moreover, the abundant heterostructures constructed by the direct contact of CdS and $Cd_3(TMT)_2$ promote an efficient separation of charge carriers. Consequently, the optimized $Cd_3(TMT)_2$/CdS synthesized at 155 °C with proper ratios of CdS to $Cd_3(TMT)_2$ demonstrated an excellent benzaldehyde formation rate of 787 $mmol \cdot g^{-1} \cdot h^{-1}$ without the need of organic solvent under visible-light irradiation ($\lambda \geq 420$ nm). Following this work, a $CdIn_2S_4$-CdS sheet-to-sheet heterojunction structure enriched with abundant defect-induced S-vacancies on the photocatalyst surface was achieved via a facile hydrothermal procedure, as reported by Tan *et al.*[101]. In the two-dimensional (2D) $CdIn_2S_4$-CdS composite photocatalyst, the photogenerated electrons could migrate from the CB of $CdIn_2S_4$ towards CB of CdS, leading to efficient spatial separation of photogenerated charge carriers. Additionally, the abundant S vacancies, characterized by their strong affinity for $O_2$ molecules, enable photogenerated electrons trapped in the vacancies to readily combine with $O_2$ to yield abundant $^{\bullet}O_2^-$, which serve as ROS for the oxidation of toluene molecules. Benefiting from the facile generation of $^{\bullet}O_2^-$ species, the obtained $CdIn_2S_4$-CdS showed excellent photocatalytic performance, achieving a toluene conversion as high as 80% and a selectivity towards benzaldehyde of 99% within a 6-h photocatalytic reaction under visible light irradiation ($\lambda \geq 420$ nm).

Metal halide perovskites (MHP), featuring excellent photoelectronic properties, sufficient redox potentials, and abundant surface active sites, have garnered special attention as efficient photocatalysts for various photocatalytic applications[102-106]. Further coupling MHP with appropriate semiconductor materials to construct heterojunction structures can enhance photocatalytic performance by promoting the efficient separation of the photogenerated charge carriers[107-109]. In this context, Cui *et al.* prepared $TiO_2/Cs_3Bi_2Br_9$ (CBB) composite photocatalyst via a simple solvent precipitation method[110]. The large specific surface area of $TiO_2$ provides substantial nucleation sites, effectively downsizing the CBB components from 1 μm in its pure microcrystal to 100 nm within the composite photocatalyst. Meanwhile, DFT calculations revealed a negative adsorption energy of $TiO_2$/CBB for toluene, indicating a strong adsorption capability of toluene molecules on the catalyst surface. The enhanced adsorption is conducive to the activation of adsorbed toluene and facilitates subsequent interaction with photogenerated charge carriers to form reaction

intermediates, thereby boosting the overall reaction kinetics. The obtained $TiO_2$/CBB was found to demonstrate a type-II heterojunction, which promotes the separation of charge carriers while inhibiting the undesired severe recombination during photocatalysis, affording an excellent production rate (9,692.5 μmol·$g^{-1}$·$h^{-1}$) with high selectivity (91%) for benzaldehyde. Following that, Zhou *et al.* reported the synthesis of $Cs_3Bi_2Br_{9-x}$@AgBr core-shell photocatalyst with abundant adsorption-redox sites via an *in situ* light-assisted $Ag^+$ insertion method [Figure 1A][111]. Experimental results and DFT calculations revealed that a type-II heterojunction structure was achieved within the resulting $Cs_3Bi_2Br_{9-x}$@AgBr photocatalyst [Figure 1B]. Benefiting from the enhanced spatial charge separation and the construction of unified adsorption-redox sites, which favors the adsorption and the activation of the substrates (i.e., toluene and oxygen molecules), the as-prepared $Cs_3Bi_2Br_{9-x}$@AgBr demonstrated an optimal production rate (5.61 mmol·$g^{-1}$·$h^{-1}$) of benzaldehyde, six times higher than the pure CBB, with high selectivity (91%) [Figure 1C].

In a typical type-II heterojunction, the improved separation of photogenerated charge carriers generally comes at the cost of jeopardizing the redox potentials when two coupled semiconductors with staggered band structures come into contact[112]. Regarding this, the step-scheme (S-scheme) heterojunction, consisting of an oxidation photocatalyst and a reduction photocatalyst, has emerged as a solution to efficiently separate photogenerated charge carriers while maximizing the oxidation and reduction potentials of the fabricated S-scheme photocatalyst[37,113-116]. More recently, Jiang *et al.* reported the development of $W_{18}O_{49}$/$CsPbBr_3$ heterostructure via the *in situ* hot-injection growth method [Figure 1D][117]. Experimental results and DFT simulations revealed that an internal E-field (IEF) was established upon the $W_{18}O_{49}$/$CsPbBr_3$ heterostructure due to the staggered Fermi level and band alignment [Figure 1E]. The IEF induced by the construction of S-scheme heterojunction would cause the accumulation of photogenerated electrons in the CB of the reducing $CsPbBr_3$ component, while the holes would accumulate in the VB of oxidizing $W_{18}O_{49}$ component, affording the fabricated $W_{18}O_{49}$/$CsPbBr_3$ with strong redox potentials, enabling the simultaneous photocatalytic activation of both toluene and carbon dioxide molecules. Consequently, the as-prepared $W_{18}O_{49}$/$CsPbBr_3$ exhibited a high production rate of benzaldehyde (1,546 μmol·$g^{-1}$·$h^{-1}$) with high selectivity (80%), and a high CO production rate (143 μmol·$g^{-1}$·$h^{-1}$) [Figure 1F].

### Control of crystal facets

Considering that photocatalytic reactions always occur on the surface of certain photocatalysts, where reaction molecules receive the photogenerated electrons/holes and undergo a series of intermediate steps to produce target product molecules, it is of significant importance to investigate the structures of the exposed surface (i.e., crystal facets) for the construction of high-efficiency photocatalytic materials[118-121]. The facet effect can influence the performance of the photocatalyst in the following ways: (i) the arrangements of the surface atoms on different facets determine the distinct adsorption and activation pattern of reaction molecules, thereby modulating catalytic activity and selectivity; (ii) different facets can exhibit varied electronic band structures, providing photogenerated electrons/holes with tunable redox abilities, thus affecting the conversion of the substrates the selectivity towards target molecules for a specific photocatalytic reaction; (iii) the charge transfer and separation differ from one crystal facet to another, resulting in diverse charge densities over different facets. To conclude, investigating the facet effect is vital for the development of efficient photocatalysts with high activity, selectivity and durability. Since the cleavage of C–H bond within toluene is dominated by ROS and the oxidative photogenerated holes, it is essential to precisely engineer the exposed crystal facets and analyze their role in the activation of C–H bond.

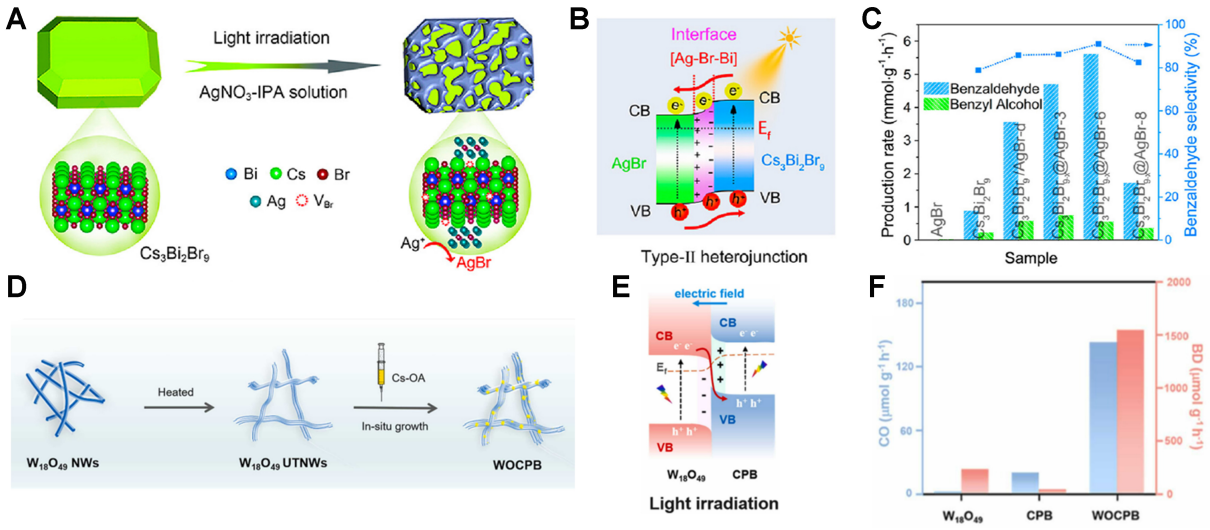


**Figure 1.** (A) Diagram depicting the synthetic process of the $Cs_3Bi_2Br_{9-x}$@AgBr core–shell heterojunction; (B) Mechanism of electron transfer in the $Cs_3Bi_2Br_{9-x}$@AgBr photocatalyst under light illumination; (C) Photocatalytic performance comparison of CBB, AgBr, and various $Cs_3Bi_2Br_{9-x}$@AgBr-X composites (where X = 3, 6, 8). Reprinted with permission. Copyright 2024, American Chemical Society[111]; (D) Diagram illustrating the preparation of the $W_{18}O_{49}$/$CsPbBr_3$ heterojunction; (E) Representation of the band structures between CPB and $W_{18}O_{49}$ under light irradiation. The $E_f$ bending at the interface was considered; (F) Photocatalytic toluene oxidation and $CO_2$ reduction over pure $W_{18}O_{49}$ ultrathin NWs, pure CPB, and WOCPB heterojunction. Reproduced with permission, Copyright 2024, Elsevier[117]. CBB: $Cs_3Bi_2Br_9$; CPB: $CsPbBr_3$; $E_f$: electric field; NWs: nanowires; WOCPB: $W_{18}O_{49}$/$CsPbBr_3$.

By adjusting the solution pH, Yang *et al.* prepared $Bi_2MoO_6$ samples with exposed {010} and {001} facets to investigate the facet effect of $Bi_2MoO_6$ photocatalyst in the selective photooxidation of toluene[122]. ESR measurements revealed that the self-induced IEFs are parallel to the {010} facet but perpendicular to the {001} facet of $Bi_2MoO_6$. Additionally, the diffusion distance was shorter in the {010} facet, ensuring efficient separation and transfer of photogenerated carriers in the $Bi_2MoO_6$ sample featuring the {010} facet. As a result, the as-prepared $Bi_2MoO_6$ sample dominated by the {010} facet exhibited a superior conversion rate of 375 μmol·$g^{-1}$·$h^{-1}$, which was 2.3 times higher than that dominated by the {001} facet (160 μmol·$g^{-1}$·$h^{-1}$) for C–H activation in toluene. Another work reported by Li *et al.* demonstrated that single-crystal oxygen-rich $Bi_4O_5Br_2$ nanosheets ($Bi_4O_5Br_2$ SCN) dominated by {10-1} crystal facets were superior to polycrystalline $Bi_4O_5Br_2$ nanosheets ($Bi_4O_5Br_2$ PCN) for the selective photooxidation of toluene[123]. DFT calculations indicated that the exposed{10-1} crystal facets of $Bi_4O_5Br_2$ favor the physical and chemical adsorption of $O_2$ molecules. In addition, the single-crystal structure with abundant surface oxygen defect sites was found to significantly facilitate the separation and transfer of photogenerated charge carriers. Benefiting from the advantages in charge carrier dynamics and the unique adsorption properties, the obtained $Bi_4O_5Br_2$ SCN featured an ultrahigh toluene conversion rate of 1,876.66 μmol $g^{-1}$ $h^{-1}$, 21-fold higher than the $Bi_4O_5Br_2$ PCN counterparts (88.22 μmol·$g^{-1}$·$h^{-1}$) under the blue light irradiation.

More recently, Zhou *et al.* reported that EC-BiOBr, featuring well-exposed {110} facets, exhibited excellent activity in the selective photocatalytic toluene oxidation[124]. DFT calculations and *in situ* Fourier transform infrared (FTIR) spectroscopy revealed that more Lewis acidic Bi sites were exposed on the {110} facets compared to {001} facets, which was found to be conducive to the oriented adsorption of toluene molecules [Figure 2A-F]. This directional adsorption of toluene on the exposed Lewis acid sites might facilitate the precise transfer of electrons from the C–H bond within toluene to the photogenerated holes ($h^+$), thereby achieving efficient photo-activation of toluene molecules. As a result, an optimal toluene conversion rate as high as 2,460 μmol·$g^{-1}$·$h^{-1}$ was achieved on the obtained EC-BiOBr, which is 11-fold higher as compared to

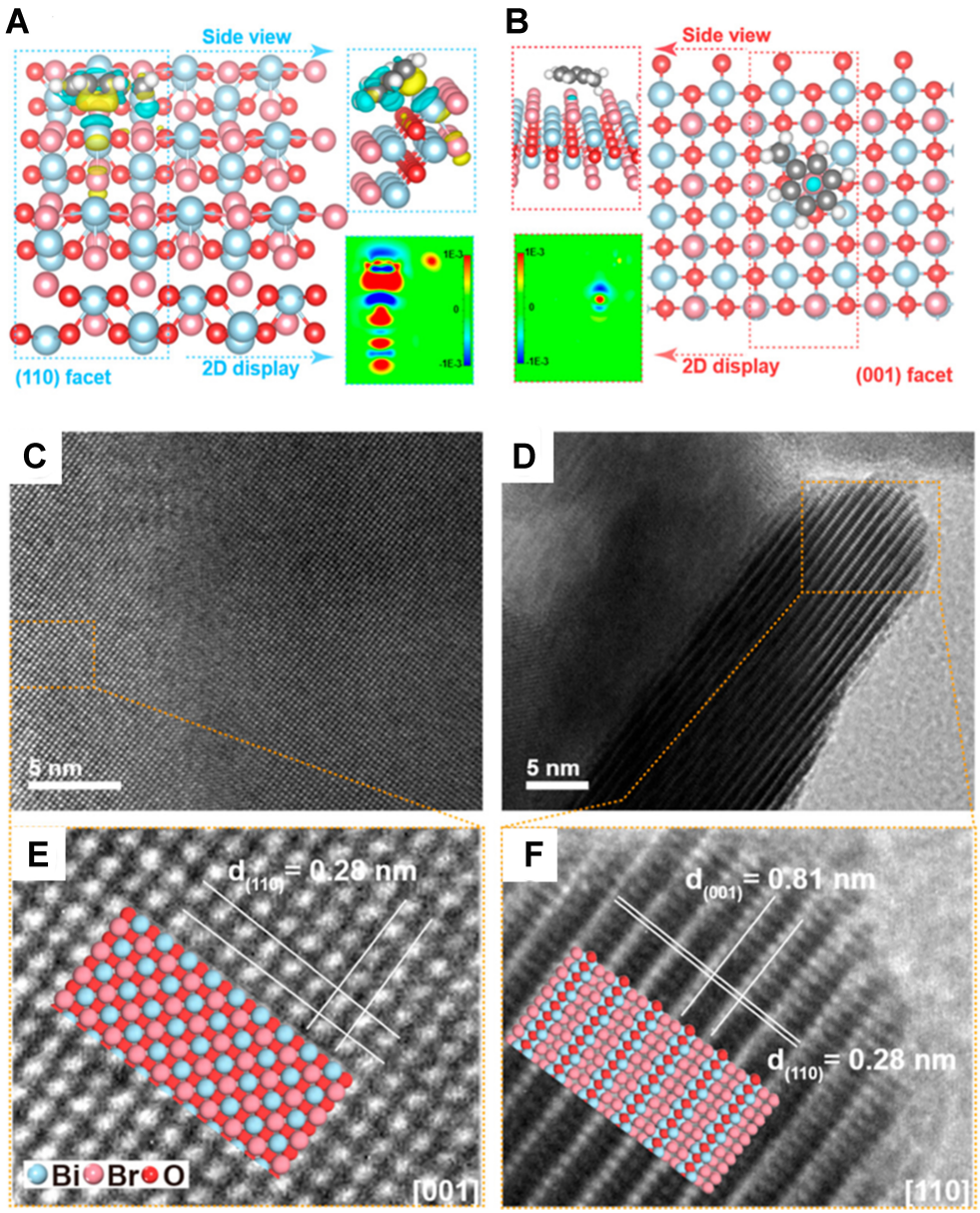


**Figure 2.** Charge difference distribution between different BiOBr crystal facets [(A) 110 facets and (B) 001 facets] and toluene (insets are the side views and 2D displays), with charge accumulation in cerulean blue (Prussian blue in 2D displays) and depletion in yellow (red in 2D displays). HRTEM images of BiOBr crystals with (001) planes (C,E), and a mixture of (001) and (110) planes (D,F). Reproduced with permission, Copyright 2024, American Chemical Society[124]. 2D: Two-dimensional; HRTEM: high-resolution transmission electron microscopy.

the (001) facet-exposed BiOBr (233 μmol·$g^{-1}$·$h^{-1}$).

### Control of crystal size

Controlling the size of semiconductor materials is an effective strategy for engineering efficient photocatalytic systems. Compared to three-dimensional (3D) bulk microcrystals, low-dimensional [i.e., two-, one- (1D), and zero-dimensional (0D)] nanosized photocatalytic materials exhibit significantly larger surface areas. This increase in surface area exposes more active sites and reduces the transfer distance of photogenerated carriers, thereby enhancing the charge separation efficiency. For instance, semiconductors

with 1D nanostructures [e.g., nanotubes, nanorods and nanowires (NWs)] promote charge transfer along their axis direction, leading to linearly polarized light emission, longer carrier lifetimes, and efficient charge separation. These attributes result in outstanding performance in a wide range of applications, such as flexible electronics, chemical sensing, optoelectronic, and photocatalytic devices[125-128]. Moreover, these nanostructures often exhibit unique morphologies due to crystal anisotropy, excitonic effects arising from reduced dielectric screening, and the preferential exposure of specific facets[129,130]. These characteristics can be fine-tuned to enhance the visible-light photocatalytic activity for the selective oxidation of toluene.

Two-dimensional nanosized semiconductor materials have garnered widespread application in the field of photocatalysis, owing to their large surface area, effective charge separation efficiency, and suitable energy band structure[131,132]. Halide perovskites nanoplates $Cs_4ZnSb_2Cl_{12}$ (CZS), averaging 9.7 nm in size, were found to demonstrate superior photocatalytic activity compared to their bulk counterparts, as reported by Mai *et al.*[133]. The size and morphology of the CZS could be precisely controlled by adjusting the starting materials, solvent composition, reaction temperature, and duration, enabling the formation of diverse nanostructures, including 0D CZS nanodots, 1D nanorods and NWs, 2D nanoplates, and 3D nanopolyhedra [Figure 3A]. By evaluating the photocatalytic activity of these CZS nanostructures, they discovered that reducing particle size could increase the surface area of the photocatalysts and induce a positive shift in the energy level of the valence band maximum (VBM), thereby enhancing the oxidation capability of these CZS nanocrystals [Figure 3B]. Compared to the 8.3 nm 0D nanodots, 9.7 nm 2D nanoplates exhibited superior catalytic performance for toluene oxidation to benzaldehyde (conversion rate = 1,998 $\mu mol \cdot g^{-1} \cdot h^{-1}$, selectivity towards benzaldehyde = 95%) [Figure 3C]. This enhancement was attributed to the anisotropic charge transport within the 2D CZS nanoplates, which inhibited charge recombination and prolonged the lifetime of the charge carriers. Moreover, these nanoplates exposed specific facets with reduced effective mass, further contributing to their enhanced catalytic activity.

Beyond the conventional colloidal synthesis of uniformly sized and shaped photoactive nanosized guest nanomaterials, employing porous materials such as mesoporous SBA-15 and microporous materials (e.g., silicates, carbons, polymers, COFs, and MOFs) to restrict the growth of these guest materials into low-dimensional nanostructures has proven to be a potent method for fabricating the robust and efficient photocatalysts[134-137]. This approach leverages the combined properties of both guest photoactive materials and porous host materials, benefiting the overall photocatalytic performance. In this context, Dai *et al.* reported the synthesis of CBB halide perovskite nanoparticles (2-5 nm) confined within the pore channels of SBA-15, resulting in a high surface to bulk ratio and increased exposure of catalytically active centers on the crystal surface[134]. DFT calculations further revealed that the formation of perovskite nanoclusters such as $Cs_{12}Bi_{14}Br_{54}$ could enhance charge separation and facilitate close interactions with hydrocarbon starting materials, thereby promoting the activation of stubborn C–H bonds [Figure 3D-G]. Consequently, the as-prepared CBB/SBA-15 demonstrated an optimal toluene conversion rate up to ca. 12,600 $\mu mol \cdot g_{cat}^{-1} \cdot h^{-1}$, significantly higher than that of pure CBB microcrystals (140 $\mu mol \cdot g_{cat}^{-1} \cdot h^{-1}$) [Figure 3H and I]. Taking advantage of the unique properties of microporous materials and the exceptional photoactive redox-catalytic properties of polyoxometalate (POM) nanoclusters, Yu *et al.* synthesized novel helical microporous nanorods (HMNRs) via a facile hydrothermal procedure, employing POM nanoclusters as the building blocks[138]. The obtained HMNRs demonstrated the unique helical microporous structures, acting as highly optimized nanoreactors for facilitating the interactions between substrates and active sites within the POM units. Additionally, the extended alkyl chains of the decyltrimethylammonium (TTA) surfactants on the surface of HMNRs further enhanced interaction between the toluene molecules and the catalytic active sites. These characteristics collectively led to an optimized conversion rate of the reaction, achieving an impressive 2,254 $\mu mol \cdot g^{-1} \cdot h^{-1}$, representing a 50-fold increase as compared to that of $K_6[\alpha\text{-}P_2W_{18}O_{62}] \cdot 14H_2O$.

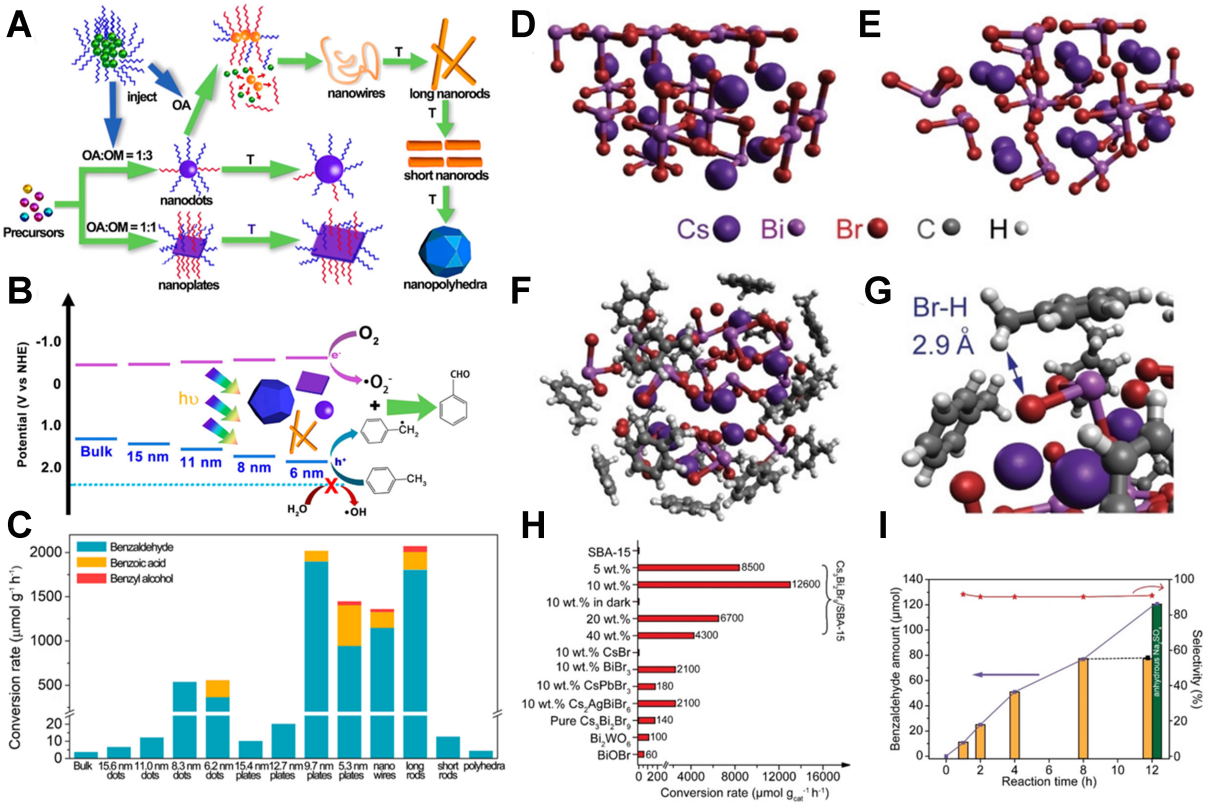


**Figure 3.** (A) Diagram illustrating the control of size and shape in CZS nanocrystals; (B) Energy level schematic of photogenerated carriers in CZS nanocrystals of varying sizes, along with the mechanism for photocatalytic toluene oxidation; (C) Conversion rate of toluene over CZS nanocrystals with different sizes and morphologies. Reproduced with permission, Copyright 2023, American Chemical Society[133]; (D) $Cs_{12}Bi_{14}Br_{54}$ cluster derived from crystal structure of CBB; (E) Optimized $Cs_{12}Bi_{14}Br_{54}$ cluster at the PBE-D3/def2-svp level; (F) Optimized geometry of the $Cs_{12}Bi_{14}Br_{54}$ cluster incorporating 17 toluene molecules; (G) Focus on a representative Br–H geometry; (H) Photocatalytic toluene oxidation over various photocatalysts; (I) Time-dependent toluene photooxidation over 10 wt % CBB/SBA-15 composite photocatalyst. Copyright 2020, Wiley-VCH[134]. CZS: $Cs_4ZnSb_2Cl_{12}$; CBB: $Cs_3Bi_2Br_9$; PBE: Perdew-Burke-Ernzerhof.

## Construction of SACs

Recently, SACs, characterized by uniform and isolated metal atoms/ions or mononuclear metal complexes anchored on suitable supporting material, have emerged as a hot topic in the field of photocatalysis[139-143]. Theoretically, SACs maximize metal utilization by achieving 100% dispersion of metal active centers on the supporting material surface, offering a distinct advantage for developing efficient and cost-effective heterogeneous catalysts. The flexibility in combining single-atom metal centers with various host materials, coupled with precise control over the local coordination environments, opens up extensive possibilities for designing highly efficient SACs. More importantly, the study of SACs provides a unique platform for in-depth understanding of photocatalytic reaction mechanism at the atomic and molecular levels[144-146]. This detailed insight would rationalize the design of SACs with optimized activity, selectivity, and stability, thereby pushing the boundaries of photocatalysis to new heights.

MOFs, comprising light-harvesting linkers and isolated metal ions/cluster nodes, represent a novel class of crystalline porous materials holding promise for various photocatalytic applications[147-149]. To enhance the light absorbance and ensure the active sites of MOFs possess appropriate redox potentials for breaking chemically inert C–H bonds under ambient conditions, Xu *et al.* incorporated $Fe^{3+}$ within the UiO-66 MOF materials by coordinatively binding them to Zr-oxo clusters, resulting in Fe-doped UiO-66 (Fe-UiO-66)[150].

The anchoring of single $Fe^{3+}$ ions onto UiO-66 induced an effective metal-to-cluster charge transfer (MCCT) process in the as-prepared Fe-UiO-66 photocatalyst. Unlike the traditional light-induced excitation mechanism of semiconductors, which relies on the energy band theory of semiconductors, the unique MCCT transition provides more stable charge separation states. This process not only extends the light absorbance of the Fe-UiO-66 photocatalyst into the visible light range but also facilitates the oriented transfer of photogenerated electrons from $Fe^{3+}$ to Zr-oxo clusters. In the photooxidation system, photogenerated holes oxidize water to produce $^{\bullet}OH$ radicals, initiating and driving the C–H activation of toluene, while the electrons reduce $O_2$ to $^{\bullet}O_2^-$ radicals, further promoting the conversion of toluene. This work represents the first report of using MOF-supported SACs for highly efficient photocatalytic C–H bond activation via an MCCT process.

More recently, Xue *et al.* reported the development of rare-earth single-atom Y anchored on $TiO_2$ ($Y_1/TiO_2$) via a facile impregnation strategy for the selective photocatalytic oxidation of toluene [Figure 4A][60]. The obtained $Y_1/TiO_2$ featured substantial atomically dispersed $Y_1^{\delta+}$-O-$Ti^{3+}$ interfacial sites, facilitating the generation of highly spin-polarized electrons, effectively inhibiting the recombination of the photogenerated electron-hole pairs and thus optimizing the separation of charge carriers [Figure 4B-D]. Mechanism investigations showed that the presence of uniformly dispersed $Y_1^{\delta+}$-O-$Ti^{3+}$ sites can promote the dual activation of both molecular oxygen and surface lattice oxygen to form highly ROS, thereby leading to an optimal photocatalytic activity (conversion rate = 850 μmol·$g^{-1}$·$h^{-1}$, selectivity towards benzaldehyde = 94.1%) for $Y_1/TiO_2$, as compared to anatase $TiO_2$ (conversion rate = 630 μmol·$g^{-1}$·$h^{-1}$, selectivity towards benzaldehyde = 64.1%) [Figure 4E and F]. Similarly, da Silva *et al.* prepared poly(heptazine imides) (PHI)-stabilized iron/manganese SACs through a simple cation exchange procedure[151]. Operando X-ray absorption spectroscopy (XAS) measurements revealed that the isolated metal sites could undergo oxidation to form high-valent oxo species (i.e., Fe=O and Mn=O) in the presence of photogenerated holes. Experimental results demonstrated that the obtained high-valent oxo species, rather than the conventional reactive free radicals (e.g., $^{\bullet}O_2^-$), were responsible for the efficient activation of C–H bonds followed by the formation of C–O bonds, leading to a high toluene conversion rate and high selectivity towards benzaldehyde.

In addition to facilitating the efficient transfer and separation of charge carriers, optimizing the surface kinetics of the photocatalyst through the creation of hydrophilic and oleophilic sites is crucial for C–H activation[152]. Regarding this, Teng *et al.* undertook the engineering of isolated hydrophilic C≡N-$Sb(CN)_3$ sites within hydrophobic $sp^2$ carbon-conjugated COFs ($sp^2$-c-COFs) specifically for toluene photooxidation[48]. The resulting Sb5-$sp^2$-c-COFs photocatalyst showcased a remarkable conversion rate of 2.248 mmol·$g_{catalyst}^{-1}$·$h^{-1}$ for toluene, representing a 54-fold increase compared to pristine $sp^2$-c-COFs. Moreover, it demonstrated an optimal selectivity of 80% for benzyl benzoate, along with impressive durability over multiple reaction cycles (five cycles, 5 h for one cycle). Mechanism investigation revealed that the superior photocatalytic activity of Sb5-$sp^2$-c-COFs photocatalyst could be attributed to the introduction of hydrophilic water-capturing C≡N-$Sb(CN)_3$ sites, which were found to enhance charge concentration and promote efficient charge separation in the presence of water.

The advancement of SACs offers valuable insights into the atomic-scale mechanisms of photocatalytic C–H bond activation. Nonetheless, achieving precise construction of uniform active sites on the photocatalyst surface poses challenges, as the exposure and reactivity of individual atom sites can vary significantly. Further research is necessary to explore the intricate engineering of truly active single-atom sites and comprehensively elucidate the structure-activity relationship using multiple state-of-the-art *in situ* and *ex situ* techniques.

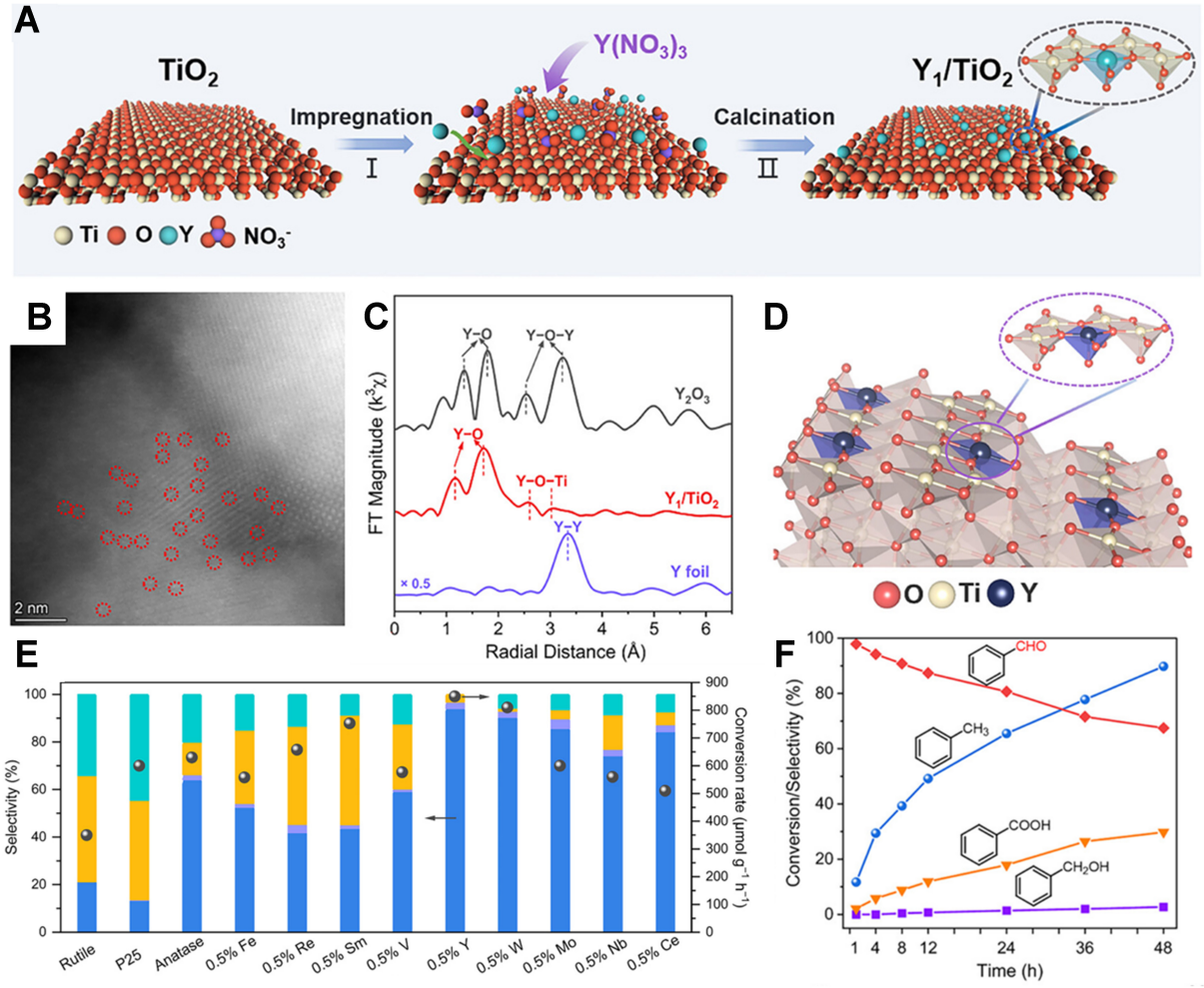


**Figure 4.** (A) Diagram showing the synthesis process of the $Y_1/TiO_2$ photocatalyst; (B) AC-HAADF-STEM image of the as-prepared $Y_1/TiO_2$; (C) Fourier-transformed EXAFS spectra at the Y K-edge; (D) Schematic model of $Y_1/TiO_2$ structure; (E) Photocatalytic toluene oxidation performance for various photocatalyst samples; (F) Photocatalytic toluene conversion and the selectivity for benzoic acid, benzyl alcohol, and benzaldehyde after 48-h of photocatalytic reaction. Copyright 2024, American Chemical Society[60]. AC-HAADF-STEM: Aberration-corrected high-angle-annular-dark-field scanning transmission electron microscopy; EXAFS: extended X-ray absorption fine structure.

## Defect engineering

The engineering of defects within a semiconductor crystal is widely recognized as an effective strategy for modulating the catalytic performance for specific photocatalytic reactions. The critical role of defects within semiconductors has been systematically investigated in many excellent review works[153-157]. In summary, the introduction of defect sites can influence the photocatalytic process in the following aspects: (i) defect sites can act as catalytically active sites, facilitating the adsorption and subsequent dissociation of substrate molecules; (ii) the creation of defects can facilitate the efficient transfer of photogenerated electrons between the semiconductor and the reactant molecules; (iii) the presence of defect sites can alter the band structure, extending the light absorption range and thereby promoting light utilization. Herein, with a focus on the photocatalytic activation of C–H bond in toluene, we provided a summary of recent advancements in several representative defective photocatalytic materials, aiming to illustrate how defect sites impact each step of the selective photocatalytic conversion of toluene towards benzaldehyde.

Dating back to 2018, Cao *et al.* reported the fabrication of $Bi_2WO_{6-x}$/amorphous BiOCl (*p*-BWO) nanosheets via a facile hydrothermal strategy[47]. The obtained *p*-BWO demonstrated a unique reversible photochromic phenomenon, which could be attributed to the rapid capture and consumption of photogenerated electrons by abundant [$W_{(VI)}O_{6-x}$] units exposed at the crystalline-amorphous boundaries [Figure 5A]. Comprehensive experimental results confirmed that the introduction of amorphous BiOCl resulted in the disruption of ordered W-O-W bridge bonds within $WO_6$ octahedral layers, replacing them with W=O terminal bonds, thereby generating numerous [$W_{(VI)}O_{6-x}$] active sites. These defect sites on the *p*-BWO surface trap and subsequently consume photogenerated electrons for $W_{(VI)}$ reduction towards $W_{(V)}$, while $W_{(V)}$ can be further regenerated to form $W_{(VI)}$ in the presence of oxygen molecules, completing the overall photochromism cycle [Figure 5B and C]. The unique photochromism phenomenon, induced by the construction of distorted [$W_{(VI)}O_{6-x}$] sites on the catalyst's outer boundaries, not only helps enhance the efficient separation of photogenerated charge carriers, but also shortens the electron transfer pathlength between photocatalysts and the substrates, thus endowing the *p*-BWO nanosheets with an impressive toluene conversion rate of 4,388 $\mu mol \cdot g^{-1} \cdot h^{-1}$ and high selectivity for benzaldehyde (> 80%) [Figure 5D].

While defect sites are crucial for the robust adsorption of reactant molecules, they might also result in strong interactions with product molecules, introducing unnecessary kinetic barriers that hinder the overall reaction process. Given this, Li *et al.* prepared ultrathin BWO nanosheets modified with moderate Bi defects (denoted as BT-48) via an optimized defect-doping strategy for the photoactivation of toluene[158]. DFT calculations and physiochemical measurements confirmed that the introduction of Bi defects can not only enhance the adsorption and activation of toluene but also facilitate the desorption of the benzaldehyde product. Moreover, the construction of Bi defects intricately modulates the local electronic structure of the BWO surface, which is conducive to promoting the separation and transfer of photogenerated charge carriers. These characteristics collectively contribute to an optimized production rate (6,781 $\mu mol \cdot g^{-1} \cdot h^{-1}$) with high selectivity (96%) for benzaldehyde achieved on the as-prepared BT-48 photocatalyst. More recently, Wang *et al.* reported the synthesis of amorphous BiOCl/$TiO_2$ (0.01BOC/$TiO_2$), in which only a small amount of BiOCl (0.01 mol) was strategically assembled on the surface of $TiO_2$[159]. In addition to constructing a type-II heterojunction at the interface of the composite photocatalyst [Figure 5E], which facilitates charge carrier separation and transfer, the amorphous BiOCl structure introduces abundant oxygen defect sites on its surface, further promoting the separation efficiency of charge carriers, thereby contributing to the overall improved photocatalytic performance. Moreover, the abundant oxygen defects in the amorphous BiOCl component exhibited strong adsorption and activation of $O_2$ molecules; in the meanwhile, the product benzaldehyde can be easily desorbed from the amorphous BiOCl surface, further enhancing the selectivity for benzaldehyde. Consequently, the as-prepared 0.01BOC/$TiO_2$ demonstrated an excellent production rate of 1.7 $mmol \cdot g^{-1} \cdot h^{-1}$ with high selectivity (80%) for benzaldehyde, outperforming the individual BiOCl and $TiO_2$ [Figure 5F].

It is widely acknowledged that coupling noble metal species with certain semiconductor materials results in the formation of an efficient Schottky barrier at the interface, effectively preventing the severe recombination of photogenerated charge carriers[160,161]. Furthermore, the incorporation of metal species would generate point defect sites (e.g., O- and S-vacancies) onto the semiconductor surface, which serve as highly active sites for diverse photocatalytic reactions. Regarding this, Li *et al.* fabricated a Pd/BiOBr composite photocatalyst by dispersing Pd nanoparticles onto the BiOBr flower-like sphere via a facile photo-deposition method[88]. Comprehensive experimental results revealed that the integration of Pd within the Pd/BiOBr leads to the formation of abundant O-vacancies on the BiOBr surface, enabling the efficient adsorption of both the oxygen and toluene substrates. As a result, the as-prepared Pd/BiOBr demonstrated an optimized toluene conversion rate (6,022.5 $\mu mol \cdot g_{cat}^{-1} \cdot h^{-1}$) and high selectivity (> 99%).

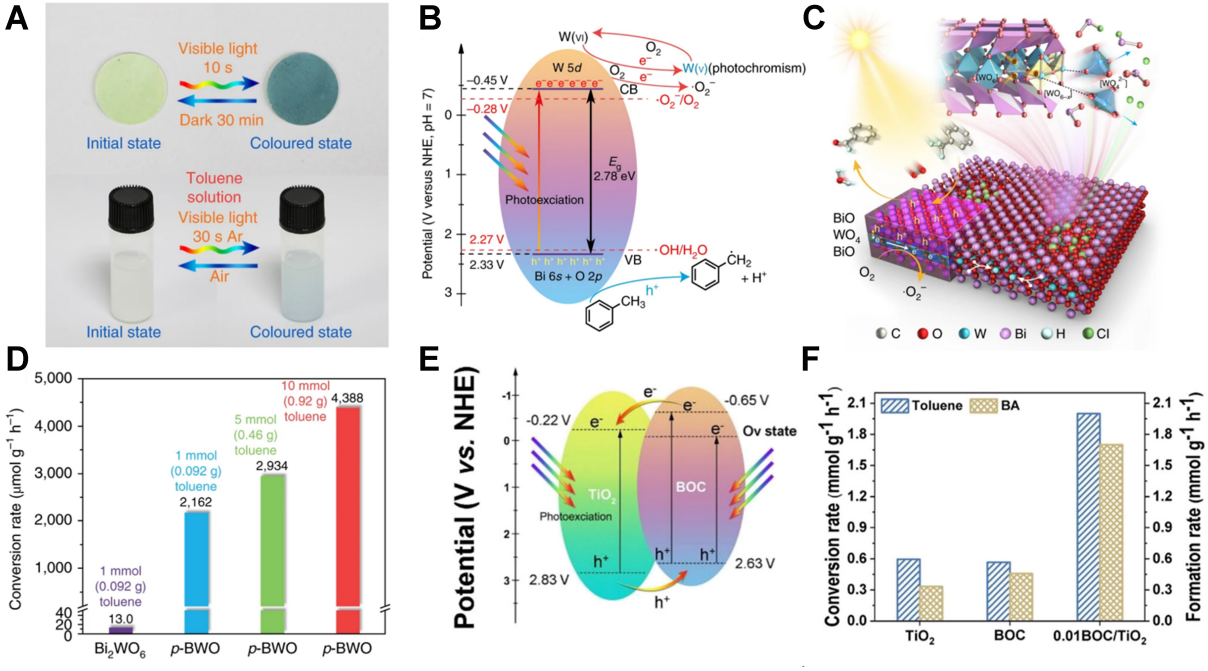


**Figure 5.** (A) Digital images showing *p*-BWO in its initial state versus its colored state; (B) Diagram illustrating the separation of photogenerated carriers in *p*-BWO, and the mechanism behind photocatalytic toluene oxidation and photochromism; (C) Schematic depiction of the microscopic structure and operational mechanism of *p*-BWO; (D) Toluene conversion rate for BWO, and *p*-BWO at varying substrate loadings. Reprinted with permission, Copyright 2018, Springer Nature[47]; (E) Illustration of the band structure for 0.01BOC/$TiO_2$; (F) Toluene conversion rate and the benzaldehyde formation rate for $TiO_2$, BOC, and 0.01BOC/$TiO_2$. Reproduced with permission, Copyright 2023, American Chemical Society[159]. *p*-BWO: Photochromic $Bi_2WO_{6-x}$/amorphous BiOCl; BOC: BiOCl; NHE: normal hydrogen electrode.

### Heteroatom doping

Doping heteroatoms, including F, B, N, P, and S atoms, into semiconductor materials is widely recognized as a potent strategy for modulating the local structures and electronic microenvironment of the active sites. Additionally, these dopants play a crucial role in determining the path of charge transfer, as some dopants have the ability to generate additional electronic states within the energy levels of the semiconductor hosts, thereby customizing the dynamics of charge transfer. In this section, we will explore how heteroatom dopants within different semiconductor materials influence the photocatalytic behavior of the fabricated photocatalyst.

Doping Nitrogen atoms into $Nb_2O_5$ nanomeshes semiconductors ($Nb_2O_5$-N) was found to significantly enhance the photocatalytic activity, resulting in a 37-fold increase in the benzaldehyde production rate (25 μmol·$g^{-1}$·$h^{-1}$) as compared to the commercial unmodified $Nb_2O_5$ (0.66 μmol·$g^{-1}$·$h^{-1}$), in the photocatalytic oxidation of toluene into benzaldehyde under visible light irradiation, as reported by Su *et al.* [Figure 6A][162]. Based on comprehensive experimental results, the superior photocatalytic performance can be attributed to the synergistic effect of the following reasons [Figure 6B]: (i) N-modification extends visible-light absorption range into the visible region; (ii) the nanomesh nanostructure promotes the transfer and separation of charge carriers, as demonstrated by transient photocurrent response spectra [Figure 6C]; (iii) the presence of $Nb^{4+}$ and oxygen vacancies created by N-doping enhances $O_2$ adsorption and subsequent activation. Recently, Ding *et al.* investigated several F-doping models within polymeric carbon nitride (PCN) using first-principles calculations[163]. Simulation results revealed that among various F-doping types in PCN, two stable and cooperative F-doping types were identified and analyzed. One involves the formation of a C($sp^3$)–F ($F_{corner}$ type) bond, and the other involves the replacement of an amino group

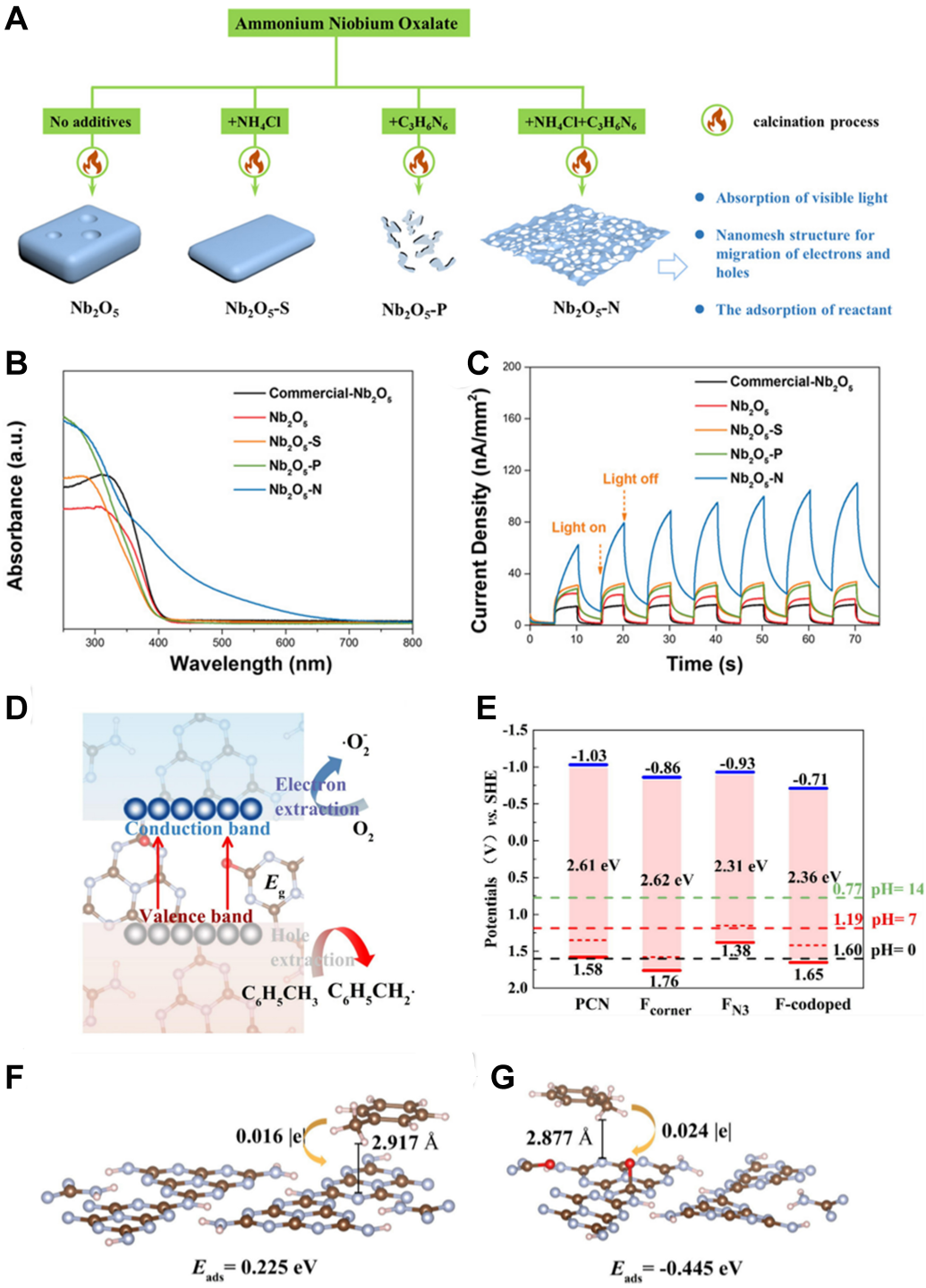


**Figure 6.** (A) Diagram illustrating and comparing various Nb-based photocatalysts; (B) UV-vis diffuse reflectance spectra for the as-synthesized Nb-based photocatalysts; (C) Transient photocurrent response spectra for the as-prepared Nb-based photocatalysts. Reprinted with permission, Copyright 2020, American Chemical Society[162]; (D) Diagram showing the photocatalytic oxidation of toluene over F-doped PCN photocatalysts; (E) Band-edge positions of both F-doped and pristine PCN relative to SHE; (F) Structure of toluene adsorbed onto pristine PCN, with $E_{ads}$ representing the toluene adsorption energy; (G) Structure of toluene adsorbed onto F-codoped PCN, with $E_{ads}$ representing toluene adsorption energy. Reproduced with permission, Copyright 2023, Elsevier[163]. UV-vis: Ultraviolet-visible spectroscopy; PCN: polymeric carbon nitride; SHE: standard hydrogen electrode.

-$NH_2$ by an F atom ($F_{N3}$ type), resulting in the formation of a covalent C–F bond. In the $F_{corner}$ and $F_{N3}$ co-doped PCN model, the $F_{corner}$ doping reduces the energy level of VBM, leading to a polarized distribution of excited electron-hole pairs, and increases the photogenerated hole distribution on F atoms, thereby strengthening the photocatalytic oxidation capacity and promoting the electron-hole separation efficiency. Meanwhile, the $F_{N3}$ doping contributes to a slight reduction in the band gap and improves the light-harvesting capability [Figure 6D and E]. Moreover, the adsorption behavior of toluene is greatly enhanced on the fabricated F-codoped PCN model ($E_{ads}$ = -0.445 eV) compared to pristine PCN model ($E_{ads}$ = -0.225 eV), further facilitating the subsequent activation of toluene on the photocatalytic active sites [Figure 6F and G]. However, due to limited computational resources, the study failed to account for the crucial factor of the concentration of different F-doping sites within PCN. Additionally, future research endeavors are expected to leverage more advanced theoretical methodologies and substantial computational resources to provide a more comprehensive picture for understanding the influence of various dopants on modulating the photocatalytic behavior of typical semiconductor materials.

### Development of novel photocatalysts

The quest for novel types of photocatalysts has long been a focal point in the field of photocatalysis[40,164,165]. Not only does it expand the family of available photocatalysts, but it also deepens our understanding of the intricate photocatalytic reaction mechanism, involving multiple steps throughout the overall reaction process (e.g., construction of photocatalytic active sites, generation of photogenerated charge carriers, separation and transfer of the charge carriers, adsorption and activation of substrates, stabilization and observation of reaction intermediates, and desorption of products). In this section, we will discuss several representative works on the development of novel photocatalysts, such as MOFs with novel topology, supramolecular $Pd_6L_4^{12+}$ porous materials, ultrathin rare earth (RE) oxide NWs, and lead halide perovskites with different ratios of A-site cations[49,166-170].

Recently, Khoo *et al.* designed and prepared a novel Fe-doped Zr-MOF featuring a (4,12)-connected **ith** topology [i.e., Nebraska porous framework (NPF)-520], incorporating rare $Zr_9$ nodes instead of the widely reported 12-connected $Zr_6$ nodes, for the selective photooxidation of toluene [Figure 7A and B][168]. The incorporation of $Fe^{III}$ induced a robust MCCT effect, resulting in a red shift in the ultraviolet-visible spectroscopy (UV-vis) and enhanced visible light absorption of the composite photocatalyst as compared to the pristine NPF-520 [Figure 7C]. Moreover, it was revealed that the selectivity of the products could be modulated by adjusting the water content in the photocatalysis reactor. In the presence of water, multiple ROS species (i.e., $^{\bullet}O_2^-$, and $^{\bullet}OH$) are generated, which could oxidize toluene into the partially oxidized derivatives, leading to the formation of benzyl alcohol, benzaldehyde, and benzoic acid [Figure 7D]. In contrast, in the absence of water in the reaction system, only toluene radicals are formed, which then combine with $^{\bullet}O_2^-$ to produce solely benzaldehyde, resulting in high selectivity for benzaldehyde production [Figure 7E]. Another work reported by Zhang *et al.* investigated the effect of amorphization on the photocatalytic performance of phosphonate-based MOF (FePPA) materials [Figure 7F][170]. In comparison to crystalline FePPA (c-FePPA), amorphous FePPA (a-FePPA) features more distorted metal nodes (i.e., Fe-oxo clusters), optimizing the electronic structure and thereby promoting the separation and transfer of charge carriers. Additionally, the presence of distorted Fe-oxo clusters provides the amorphous FePPA with enhanced Lewis acidity, thus promoting the adsorption and the subsequent activation of $O_2$ molecules. As a result, the obtained a-FePPA exhibited an excellent production rate (274 $\mu mol \cdot g^{-1} \cdot h^{-1}$) for benzaldehyde, much higher than the crystalline counterparts (112 $\mu mol \cdot g^{-1} \cdot h^{-1}$).

To mimic the concept of C–H bond activation within a natural enzyme's hydrophobic cavity, the construction of supramolecular cavities with diverse shapes, sizes, and electronic properties has been explored as a viable method for hosting photocatalytic reactions[171-173]. In this context, Das *et al.* employed a

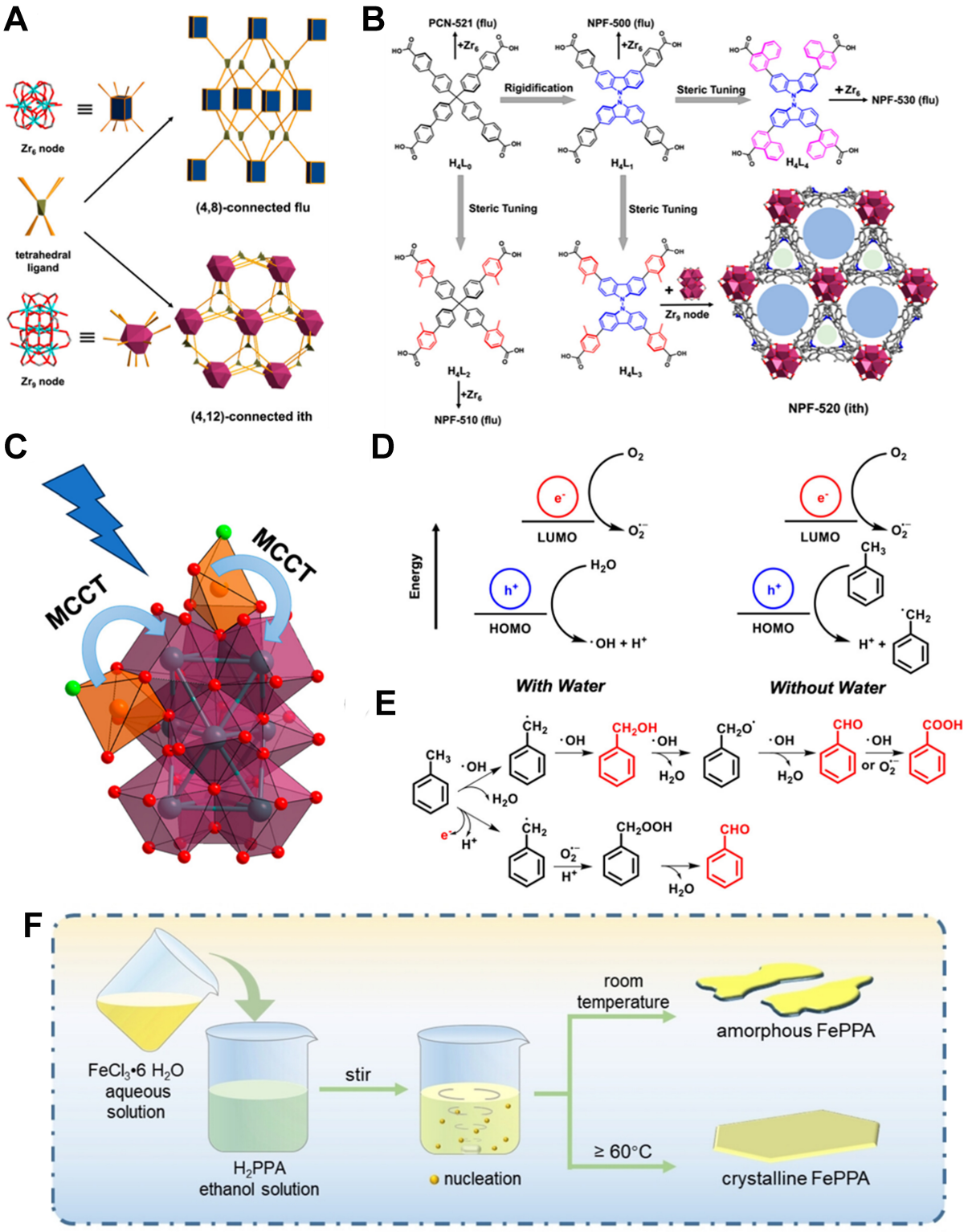


**Figure 7.** (A) Illustration showing the preparation of (4,8)-connected **flu** and (4,12)-connected **ith** topologies from a tetrahedral ligand, involving $Zr_6$ and $Zr_9$ nodes, respectively; (B) Stepwise process for the rigidification and steric modification of tetrahedral ligands to create NPF-520 with **ith** topology; (C) Diagram depicting the charge transfer mechanism from $Fe^{III}$ to Zr-oxo cluster in the $Fe^{III}$-decorated $Zr_9$ node (with Zr in violet, O in red, Fe in orange, and Cl in green); (D) Development of reaction intermediates when water is present versus in an anhydrous environment; (E) Proposed pathway for the photocatalytic oxidation of toluene. Reprinted with

permission, Copyright 2023, American Chemical Society[168]; (F) Diagram illustrating the synthesis of both amorphous and crystalline FePPA photocatalysts. Reproduced with permission, Copyright 2024, Wiley-VCH[170]. NPF: Nebraska porous framework.

cationic $Pd_6L_4^{12+}$ (L = ligand) nanocage to encapsulate toluene molecules and convert them into benzaldehyde under visible light irradiation[49]. Comprehensive measurements revealed that the C–H bond in toluene can be preorganized and polarized within the water-soluble cationic $Pd_6L_4^{12+}$ nanocavities. This preorganization facilitates the photoactivation of toluene molecules via an ultrafast proton-coupled electron transfer (PCET) reaction under ambient conditions. Further investigation indicated that the preorganization was induced by the strong E-fields generated by the electrostatic field of the six $Pd^{2+}$ ions in the $Pd_6L_4^{12+}$ nanocage. Modulating the E-fields was proposed as a promising approach to enable selective bond polarization in complex polyatomic molecules encapsulated within the well-designed nano-hosts.

Metal-halide perovskites have emerged as highly effective photocatalysts due to their exceptional light-harvesting capabilities, suitable band gaps, and excellent charge transfer properties. They have been successfully employed within several photocatalytic processes, demonstrating significant potential for selective photoactivation of various organic/inorganic molecules[174-177]. The substitution of B-site $Pb^{2+}$ cations with $In^{3+}$, $Sb^{3+}$, $Bi^{3+}$ has been widely investigated due to their low toxicity and their beneficial effects on optimizing the band gap structures, thereby improving light-harvesting ability and redox potentials of photogenerated charge carriers. However, A-site cation substitution is rarely considered, as these cations do not directly participate in the construction of the perovskite band gaps. Regarding this, Zhang *et al.* prepared lead-free $A_2Sb_2Br_9$ perovskite nanocrystals with varying ratios of Cs and $CH_3NH_3$ (MA) to explore how changes in the A-site composition influence the photocatalytic behavior of the fabricated perovskite photocatalysts[166]. Experimental results revealed that the distortion of [$SbBr_6$] octahedron in the as-prepared $Cs_xMA_{3-x}Sb_2Br_9$ increases with the incorporation of larger MA ions. The A-site-induced distortion facilitates the electron depletion of Sb-sites and accumulation on the Br-sites, resulting in decreased ability on the C–H bond activation and reduced stability for photocatalytic toluene oxidation. The work elucidated the relationship between A-sites induced octahedron distortion and photocatalytic performance, offering new insights for designing highly efficient halide perovskite-based photocatalysts.

Ultrathin inorganic NWs have garnered significant attention, showcasing unique chemical/physical properties as their diameters decrease to only a few crystal cells. However, their controlled and facile preparation remains a great challenge. In this context, Fu *et al.* developed a novel and general method, which enables the synthesis of a series of RE oxide ultrathin NWs at atmospheric pressure and low temperature (50 °C), assisted by POM[167]. The low temperature was found to prevent crystal growth in the 2D/3D directions, leading to the formation of 1D NWs, while the introduction of POM facilitated the smooth 1D growth of 0D monomers. The as-prepared RE oxide NWs exhibited polymer-like behaviors, displaying high viscosity and rheological properties, and novel structure of nanosized red blood cells (RBCs) could be obtained through electro-spinning using only concentrated NWs without the addition of any polymers. Moreover, the Ce-Mo-O NWs were found to be a potential photocatalyst, affording an excellent toluene conversion rate and durability in photocatalytic toluene oxidation reaction.

In the above content, we have provided a systematic description and classification of different modification methods for the fabrication of efficient photocatalysts used in toluene photooxidation, along with an analysis of the characteristics associated with each method. To facilitate a more intuitive comparison between different modification methods. Table 1 presents the characteristics of different methods achievable in various photocatalytic systems. This comprehensive summary enables researchers to identify the most suitable approach based on their specific research needs.

**Table 1. Characteristics of different strategies for the development of photocatalysts used in selective toluene oxidation**

| Modification strategies | Synthetic method | Photocatalyst | Characteristics | Ref. |
|---|---|---|---|---|
| Heterojunction construction | Anti-solvent precipitation method | $CsPbBr_3$/*d*-BiOBr | 1. Enhanced electron transfer<br>2. Enhanced adsorption of toluene | [178] |
| | Hot-injection method | $W_{18}O_{49}$/$CsPbBr_3$ | 1. Enhanced charge carrier separation<br>2. Achieve $CO_2$ reduction to CO simultaneously | [117] |
| | Anti-solvent precipitation method | $TiO_2$/$Cs_3Bi_2Br_0$ | 1. Enhanced electron transfer<br>2. Enhanced adsorption of toluene | [110] |
| | *In-situ* light-assisted $Ag^+$ insertion method | $Cs_3Bi_2Br_{9-x}$@AgBr | 1. Enhanced charge carrier separation<br>2. Unified adsorption/redox sites for toluene and oxygen | [111] |
| | Anti-solvent precipitation method | CBB/g-$C_3N_4$ | 1. Enhanced charge carrier separation<br>2. Separated adsorption/redox sites for toluene and oxygen | [108] |
| Control of crystal facets | Crystal facet control strategy | (110) facet-exposed BiOBr | 1. Enhanced adsorption of toluene<br>2. Oriented arrangement of toluene | [124] |
| | Crystal facet control strategy (pH dependent) | (010) facet-exposed $Bi_2MoO_6$ | 1. Enhanced charge carrier separation<br>2. Enhanced light absorbance range | [122] |
| | Solvothermal method | (101) facet-exposed defective $Bi_4O_5Br_2$ | 1. Enhanced adsorption of oxygen<br>2. Enhanced charge carrier separation | [123] |
| | Crystal facet control strategy | (001) facet-exposed | 1. Enhanced charge carrier separation<br>2. Enhanced light absorbance range | [179] |
| Control of crystal sizes | Hot-injection method | $Cs_4ZnSb_2Cl_2$ nanoplates | 1. Increased oxidation ability<br>2. Strong quantum confinement effect<br>3. Enhanced surface area | [133] |
| | Incipient wetness impregnation method | CBB/SBA-15 | 1. Enhanced charge carrier separation<br>2. More accessible active sites<br>3. Close contact with toluene | [134] |
| | Colloidal method | Ce-Mo-O oxide NWs | 1. Universality of the preparation method<br>2. Excellent reusability | [167] |
| | Hydrothermal method | HMNRs | 1. Enhanced contact with toluene<br>2. Excellent reusability<br>3. Facile preparation process | [138] |
| Construction of SAC | Incipient wetness impregnation method | $Y_1/TiO_2$ | 1. Enhanced charge carrier separation<br>2. Enhanced adsorption of oxygen<br>3. Lattice oxygen-mediated toluene oxidation pathway | [60] |
| | Cation exchange method | Fe/Mn-PHI | 1. High selectivity towards benzaldehyde<br>2. High-valent metal-oxygen species-initiated toluene oxidation pathway | [151] |
| | Simultaneous polymerization and crystallization method | $Sb(CN)_3$-modified $sp^2$-c-COFs | 1. Enhanced charge carrier separation<br>2. Increased hydrophilicity of photocatalyst leads to the improved generation of ROS | [48] |
| | Microwave-assisted preparation method | Fe-UiO-66 | 1. Unique MCCT leads to extended light absorbance<br>2. Enhanced charge carrier separation | [150] |
| Defect engineering | Hydrothermal method | BWO nanosheets | 1. Enhanced adsorption of reactants<br>2. Enhanced desorption of benzaldehyde<br>3. Enhanced charge carrier separation | [158] |
| | Solvothermal method, Photodeposition process | Pd/BiOBr | 1. Enhanced charge carrier separation<br>2. Enhanced adsorption of reactants | [88] |
| | Hydrothermal method | BiOCl/$TiO_2$ | 1. Enhanced charge carrier separation<br>2. Enhanced adsorption of oxygen | [159] |
| | Hydrothermal method | $Bi_2WO_{6-x}$/amorphous BiOCl | 1. Enhanced charge carrier separation<br>2. Photochromism materials used in photocatalysis | [47] |
| Heteroatom doping | Calcination method | N-modified $Nb_2O_5$ | 1. Enhanced light absorption range<br>2. Enhanced charge carrier separation<br>3. Enhanced adsorption of reactants | [162] |
| | First-principle calculations | F-doped PCN | 1. Enhanced adsorption toluene<br>2. Enhanced light absorption range<br>3. Enhanced charge carrier separation | [163] |

| | | | | |
|---|---|---|---|---|
| Discovery of novel photocatalysts | Solvothermal method | NPF-520-$Fe^{III}$ | 1. Enhanced light absorption range<br>2. Enhanced charge carrier separation | [168] |
| | Room-temperature precipitation method | FePPA (phosphonate-based MOF) | 1. Enhanced charge carrier separation<br>2. Enhanced light absorbance range<br>3. Enhanced adsorption of oxygen | [170] |
| | 353 K heating followed by filtration | $Pd_6L_4^{12+}$ (L = ligand) nanocage | 1. Nanoconfinement effect prolongs the lifetime of radicals<br>2. Strong electrostatic field to prepolarize the toluene | [49] |
| | Anti-solvent precipitation method | $Cs_xMA_{3-x}Sb_2Br_9$ | 1. Enhanced electron transfer<br>2. Distortion of perovskite crystals | [166] |

*d*-BiOBr: Defective BiOBr nanosheets; CBB: $Cs_3Bi_2Br_9$; NWs: nanowires; HMNRs: helical microporous nanorods; SAC: single-atom catalyst; PHI: poly(heptazine imides); $sp^2$-c-COFs: $sp^2$ carbon-conjugated covalent organic framework; ROS: reactive oxygen species; MCCT: metal-to-cluster charge transfer; BWO: $Bi_2WO_6$; PCN: polymeric carbon nitride; NPF: Nebraska porous framework; MOF: metal-organic framework.

## MECHANISM INVESTIGATION

### *In situ* characterization techniques

*In situ* characterization techniques, capable of monitoring the dynamic evolution of photocatalysts during simulated/real catalytic reaction processes, are instrumental in designing highly efficient photocatalysts and elucidating related reaction mechanisms. Many excellent review works have highlighted the crucial role of various *in situ* techniques in the field of photocatalysis[180-184]. In this section, we will present and summarize several key applications of *in situ*/operando characterization techniques aimed at selective photocatalytic toluene conversion into benzaldehyde, including probing of chemical structure of photocatalysts, tracking transfer of photogenerated charges, assessing spatial distribution of charge carriers, and most importantly, determining the surface reaction pathways within the reaction environment.

*In situ electron paramagnetic resonance*

Determining the actual reaction pathways and mechanisms is crucial for the rational design and optimization of photocatalytic conversion of toluene towards benzaldehyde. During the process, multiple reactive paramagnetic species with unpaired electrons, such as $^{\bullet}OH$, $^{\bullet}O_2^-$, carbon-centered radicals ($^{\bullet}R$), are generated on the photocatalyst surfaces. To identify the formation and evolution of specific free radicals, *in situ* electron paramagnetic resonance (EPR) or ESR measurement has been developed and employed under simulated reaction conditions, aiding researchers in predicting the ongoing reaction pathways and elucidating reaction mechanisms[185]. Besides, it can also help monitor the generation of unpaired electrons in solid photocatalysts under light irradiation and detect the presence of crystal defects.

Since most free radicals are unstable, highly reactive, and short-lived, their detection is often performed using spin trap agents [e.g., 5,5-dimethyl-1-pyrroline-N-oxide (DMPO), 5-tert-butoxycabony 5-methyl-1-pyrroline-N-oxide (BMPO), and 2,2,6,6-tetramethyl-1-piperidinyloxy (TEMPO)] that selectively react covalently with a highly transient radical to generate a more stable radical (i.e., spin adduct). For instance, Cui *et al.* employed *in situ* EPR spectroscopy to directly confirm the presence of $^{\bullet}O_2$ and $h^+$ during the reaction process by using DMPO and TEMPO as spin traps[110]. As depicted in Figure 8A, four characteristic peaks corresponding to DMPO-$^{\bullet}O_2$ could be detected after 3 min light irradiation. The signals recorded at the same illumination time for $TiO_2$/CBB were much more intense than those for pure $TiO_2$ and CBB, which accounts for the higher photocatalytic activity of $TiO_2$/CBB composite photocatalyst [Figure 8B]. Moreover, three characteristic peaks corresponding to TEMPO-$h^+$ with similar intensities could be observed among the $TiO_2$, CBB, and $TiO_2$/CBB photocatalysts under dark conditions. However, the signals for $TiO_2$/CBB were much lower than those for $TiO_2$ and CBB after 5 min of light irradiation, indicating that more holes were consumed in $TiO_2$/CBB in the same period [Figure 8C and D]. The *in situ* EPR results revealed that the synergistic effect between $^{\bullet}O_2$ and $h^+$ promotes the selective conversion of toluene, demonstrating

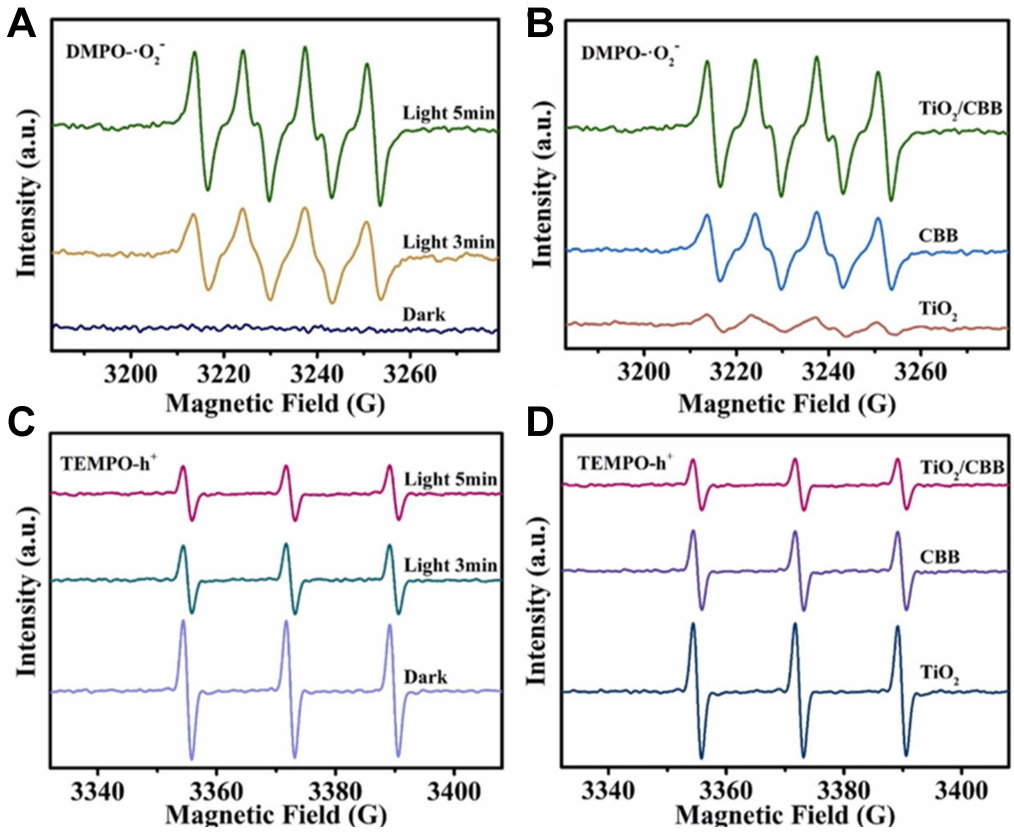


**Figure 8.** *In situ* ESR spectra of radical adducts captured by (A) DMPO ($^{\bullet}O_2^-$) and (C) TEMPO ($h^+$) in $TiO_2$/CBB dispersion under both dark and light irradiation conditions. A comparison of the ESR signal intensities for (B) DMPO ($^{\bullet}O_2^-$) and (D) TEMPO ($h^+$) in $TiO_2$, CBB and $TiO_2$/CBB photocatalysts after the same exposure to light. Reproduced with permission, Copyright 2023, Elsevier[110]. ESR: Electron spin resonance; DMPO: 5,5-dimethyl-1-pyrroline-N-oxide; TEMPO: 2,2,6,6-tetramethyl-1-piperidinyloxy; CBB: $Cs_3Bi_2Br_9$.

an efficient separation of photogenerated charge carriers over the $TiO_2$/CBB.

Besides identifying the exact radical species, *in situ* EPR measurements allow for the direct observation and monitoring of the paramagnetic active species within solid photocatalysts during photocatalytic processes. For example, Xu *et al.* utilized *in situ* EPR techniques to investigate the electron transfer mechanism within the obtained Fe-UiO-66 under light irradiation[150]. The EPR peak at g = 4.0, corresponding to Fe(III) with a high-spin state, decreased after light irradiation, accompanied by the presence of a new peak at g = 2.02. This new peak corresponds to the reduction product of $^{\bullet}O_2$ adsorbed onto Zr-oxo clusters. Upon adding methanol as a hole sacrificial agent, the signal at g = 2.00, representing oxygen-centered active sites in Zr-oxo clusters that accept electrons from Fe(III), became evident under light irradiation upon $N_2$ injection. This observation demonstrates the efficient electron transfer from Fe(III) sites to Zr-oxo clusters (i.e., MCCT process) in Fe-UiO-66.

Although EPR is highly sensitive to unpaired electrons and can detect changes of paramagnetic centers under light irradiation, its application often requires the use of a spin trap and/or low temperatures to ensure the detection of these unstable, low-yield, short-lived, reactive species with unpaired electrons. Due to these limitations, the application of EPR in photocatalysis under operando conditions remains scarce.

*In situ FTIR spectroscopy*

FTIR spectroscopy has been widely used for both quantitative and qualitative identification of the molecular structure in various organic and inorganic materials. Nevertheless, conventional FTIR is limited to offline analysis, making it challenging to monitor intermediates and dynamic changes of catalytically active sites over photocatalysts in real time. With the advent of high-sensitivity detectors, *in situ* FTIR has rapidly advanced, allowing for real-time exploration of the evolution of adsorbed molecules and reaction intermediates during photocatalytic reactions[186-191]. Additionally, it facilitates real-time visualization of reactant adsorption and specific product desorption, two crucial steps in the photocatalytic process, thereby deepening the understanding towards the superior activity and selectivity of certain photocatalysts, offering insights that drive the development of more efficient and targeted photocatalytic systems.

For instance, Zhang *et al.* utilized *in situ* FTIR spectroscopy to investigate the adsorption of toluene and the formation of various oxygenated intermediates over the as-prepared amorphous FePPA photocatalyst [Figure 9A][170]. As depicted in Figure 9B, typical signals (3,120-3,040, 1,550-1,440, and 1,603 $cm^{-1}$) attributed to C–H bonds and aromatic rings, along with signals (2,970-2,830 and 1,420-1,360 $cm^{-1}$) assigned to the stretching and bending vibration of C–H bonds within the methyl group, both increased on prolonging the irradiation time, demonstrating effective adsorption of toluene on the catalyst surface. With extended light irradiation, peaks associated with the aldehyde group (1,698 $cm^{-1}$ for C=O bonds and 2,733 $cm^{-1}$ for C–H bonds) emerged and gradually intensified, indicating the generation of benzaldehyde. Additionally, the peak at 1,176 $cm^{-1}$ could be ascribed to the peroxide intermediate, which was formed through the interaction between the $^{\bullet}O_2^-$ radical and the $^{\bullet}R$ radical. Furthermore, two weak peaks at 1,652 and 1,243 $cm^{-1}$ were identified, corresponding to water generated during the dehydration of the peroxide intermediate and the by-product benzyl alcohol, respectively.

Diffuse reflectance FTIR spectroscopy (DRIFTS), which enables the direct use of powdered photocatalysts and thus mitigates the inconvenience of external transport compared to transmission IR, has become an increasingly popular tool for investigating heterogeneous photocatalysts and screening the photocatalytic reaction processes in the *in situ*/operando mode[192-194]. For example, Xue *et al.* employed *in situ* DRIFTS to elucidate the mechanism of the photooxidation of toluene over the two photocatalysts: pristine $TiO_2$ and $TiO_2$ supported yttrium single atom photocatalyst ($Y_1/TiO_2$) [Figure 9C and D][60]. For toluene adsorption over $TiO_2$ photocatalyst, strong adsorption bands corresponding to the stretching vibrations of C–H bonds (3,079 and 3,025 $cm^{-1}$) and the C=C bonds (1,600 and 1,494 $cm^{-1}$) of the aromatic ring were detected [Figure 9E]. In contrast, only weak adsorption bands were observed for the C–H stretching vibrations (2,926 and 2,876 $cm^{-1}$) and $CH_3$ bending vibrations (1,460 and 1,380 $cm^{-1}$) of the methyl group, indicating that pristine $TiO_2$ prefers to adsorb the benzene ring rather than the methyl group of toluene. For the $Y_1/TiO_2$ catalyst, distinctive C=O stretching vibrations (1,687 and 1,280 $cm^{-1}$) attributed to the aldehyde group of benzaldehyde were detected [Figure 9F]. Concurrently, the bending vibrations of O–H bonds (1,326 $cm^{-1}$) decreased with prolonged irradiation, indicating the oxidation of benzyl alcohol to benzaldehyde. The comparison between $TiO_2$ and $Y_1/TiO_2$ reveals that toluene undergoes partial oxidation to benzaldehyde via a lattice oxygen oxidation process over $Y_1/TiO_2$, as evidenced by *in situ* DRIFTS measurements performed under Ar conditions. To establish a plausible reaction mechanism for the selective photooxidation of toluene over the two photocatalysts, *in situ* time-resolved DRIFTS were further conducted under the simulated photocatalytic reaction conditions. In the case of pristine $TiO_2$, characteristic bands corresponding to $CO_2$ increased with the irradiation time, suggesting the overoxidation of toluene into $CO_2$ over $TiO_2$ [Figure 9G]. However, for the as-prepared $Y_1/TiO_2$, the absence of $CO_2$ bands suggests an effective inhibition of toluene overoxidation, affirming the high selectivity over $Y_1/TiO_2$. Moreover, the stretching band of C=O bond corresponding to benzaldehyde adsorption over $Y_1/TiO_2$ was blue-shifted as compared

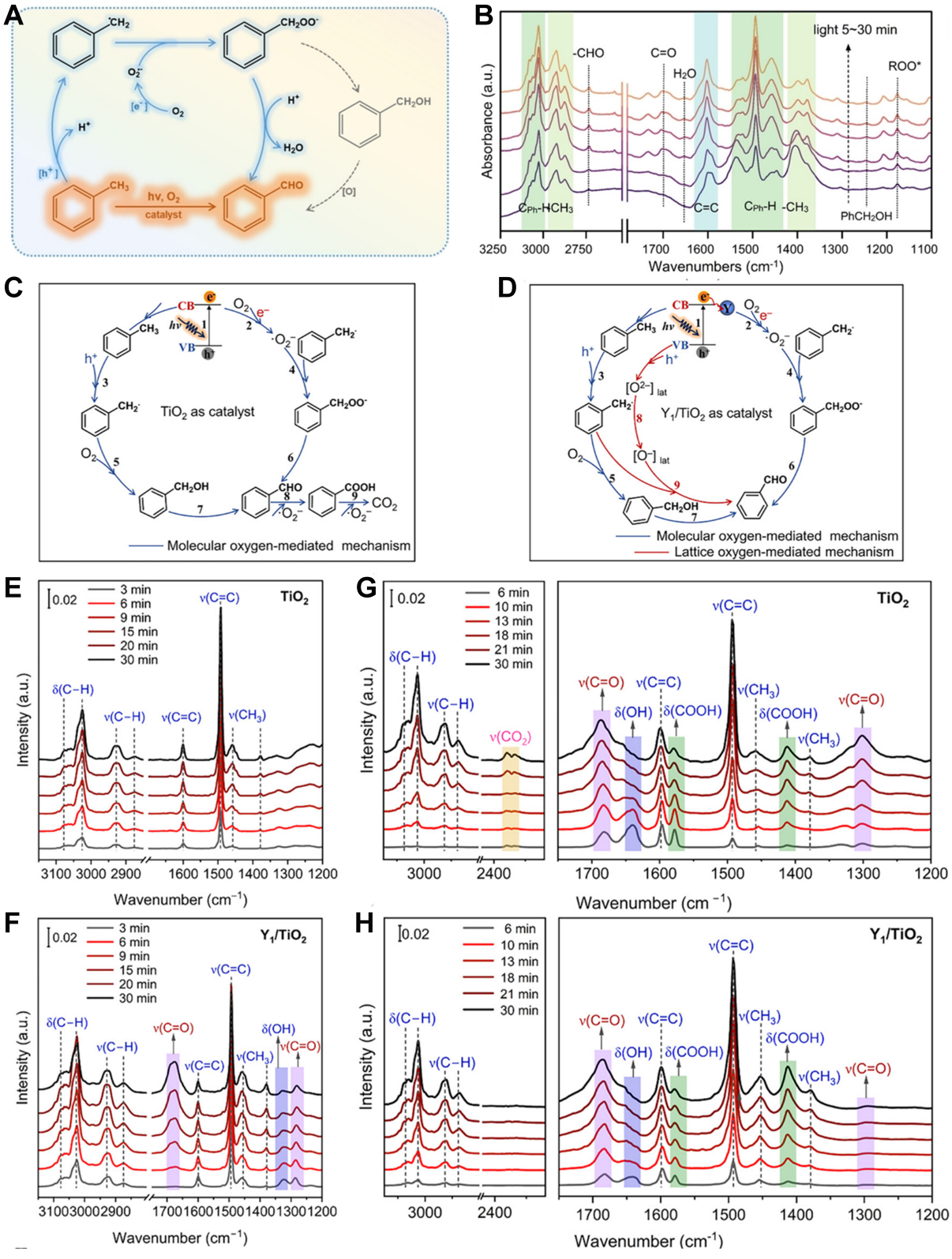


**Figure 9.** (A) Proposed mechanism for photocatalytic toluene oxidation using the FePPA photocatalyst; (B) *In situ* FTIR spectra showing the photocatalytic toluene oxidation using a-FePPA. Reprinted with permission, Copyright 2024, Wiley-VCH[170]. Proposed reaction pathways for (C) pristine $TiO_2$ and (D) $Y_1/TiO_2$ photocatalysts. *In situ* DRIFTS spectra of toluene adsorbed on (E) pure $TiO_2$ and (F) $Y_1/$

$TiO_2$ during a 30-minute Ar flushing procedure. *In situ* DRIFTS spectra of toluene oxidation over (G) pure $TiO_2$ and (H) $Y_1/TiO_2$. Reprinted with permission, Copyright 2024, American Chemical Society[60]. FTIR: Fourier transform infrared; DRIFTS: diffuse reflectance FTIR spectroscopy.

to pristine $TiO_2$, indicating a relatively weak adsorption of aldehyde group in the benzaldehyde product, further illustrating the inhibition of benzaldehyde overoxidation [Figure 9H].

*In situ X-ray photoelectron spectroscopy*

X-ray photoelectron spectroscopy (XPS), known for its high sensitivity to the chemical and electronic states of most elements, has been applied to the mechanistic elucidation of several catalytic processes[195-198]. With *in situ* light illumination, the transfer and migration of photogenerated electrons and holes under simulated light irradiation could be visualized through the shifts of binding energies, as the dynamics of photogenerated charge carriers could alter the chemical and electron environment of the targeted elements during photocatalytic processes[199-202]. The construction of heterojunctions by coupling two different semiconductors with suitable band structures has long been regarded as an effective strategy to improve the performance of the photocatalytic system. However, the band alignment could vary significantly among diverse types of heterojunction structures (e.g., type-II and Z-scheme heterostructures). To characterize the specific type of heterojunction structure within a fabricated photocatalyst, *in situ* XPS measurements have been employed, providing robust and direct evidence.

For instance, Bai *et al.* investigated the charge transfer behavior over the CBB/*d*-BiOBr photocatalyst through *in situ* XPS under visible light irradiation[178]. As depicted in Figure 10A, two peaks in the O *1s* XPS spectra underwent a slight positive shift of 0.07 eV upon light irradiation, indicating a decrease in electron density of *d*-BiOBr component. Meanwhile, two characteristic peaks in Cs *3d* XPS spectra underwent a negative shift of 0.2 eV, indicating the accumulation of electrons in the CBB component [Figure 10B]. Since the Fermi level of CBB is higher than that of *d*-BiOBr, when the two components come into close contact, free electrons in CBB would spontaneously transfer toward *d*-BiOBr to reach a new equilibrium state. This electron migration results in the alignment of the Fermi levels of CBB and *d*-BiOBr, with CBB becoming positively charged and *d*-BiOBr negatively charged. Consequently, an internal built-in E-field directed from CBB to *d*-BiOBr is formed at the composite interface. The photogenerated electrons in the CB of *d*-BiOBr would migrate to the VB of CBB and recombine with the photogenerated holes. Therefore, the charge transfer follows a direct Z-scheme structure within CBB/*d*-BiOBr, rather than a type-II one, as evidenced by *in situ* XPS. Similarly, with the aid of *in situ* light irradiation XPS measurements, a distinct S-scheme heterostructure was identified in the $W_{18}O_{49}/CsPbBr_3$ composite photocatalyst, which was found to demonstrate improved photocatalytic activity for selective toluene oxidation[117].

*In situ/operando XAS*

XAS is an effective technique for providing detailed electronic and geometric information of active sites over photocatalysts, including inter-atomic distances, types of chemical bonds, coordination numbers, and structural disorder[203-205]. Generally, XAS can be divided into two parts: X-ray absorption near edge structure (XANES) and EXAFS. XANES extends to approximately 50 eV above the absorption edge and is highly sensitive to the electronic and geometric configuration of the absorbing atom. It reflects the density of electronic states near the Fermi level, thereby revealing the oxidation states, local symmetry, and chemical bonding of the absorbing atom. The region of EXAFS follows XANES, beginning at roughly 50 eV above the absorption edge and extending to thousands of electron volts beyond it, reflecting the coordination number, coordination distance, and types of atoms surrounding the target atom. *In situ*/operando time-resolved XAS can monitor the charge transfer, evolution of geometric and electronic structures of selected

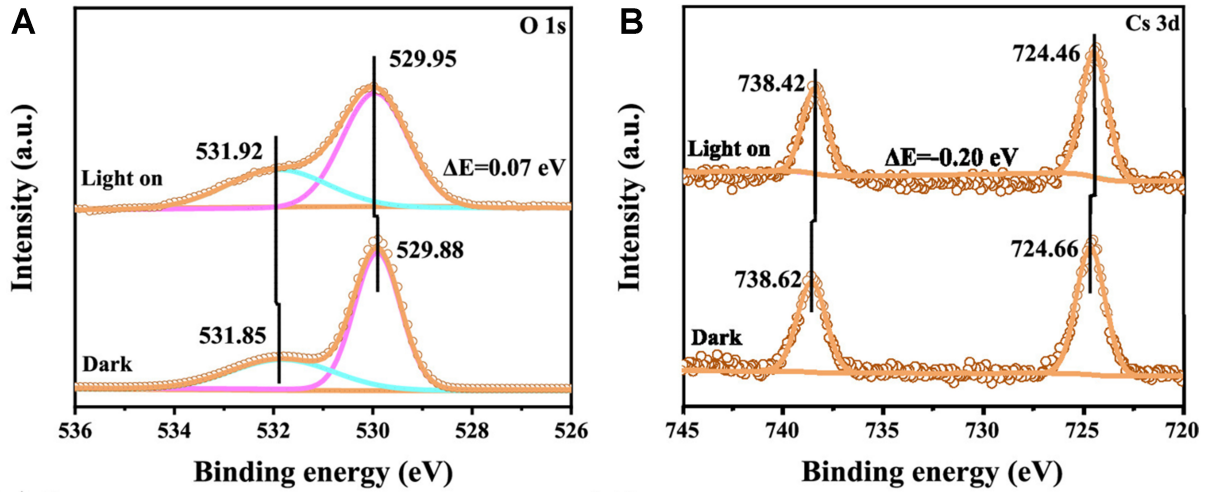


**Figure 10.** Operando XPS spectra (A) O 1s and (B) Cs 3d of CBB(1.7)/*d*-BiOBr in both dark and visible light irradiation conditions. Reproduced with permission, Copyright 2022, American Chemical Society[178]. XPS: X-ray photoelectron spectroscopy; CBB: $Cs_3Bi_2Br_9$; *d*-BiOBr: defective BiOBr nanosheets.

atomic components, offering valuable insights into the relationship between structure and catalytic performance in photocatalytic systems under simulated or realistic reaction conditions[206].

For example, the oxidation of Mn and Fe sites into active high-valent oxo species during photocatalysis was investigated by the use of operando XAS measurements, as reported by da Silva *et al.*[151]. The XAS spectrum of the dehydrated Mn-PHI photocatalyst at 250 °C in flowing He is fully consistent with the presence of only the Mn(II) oxidation state [Figure 11A]. At the same temperature, when exposed to oxygen, water, and light illumination, a notable increase in the spectral weight can be observed in the high-energy regions, specifically between 640 and 645 eV [Figure 11B and C]. Furthermore, under these conditions, a noticeable shift towards higher energies could be detected for the main peak at ca. 640 eV. These changes were reversible upon repeated cycling of light on and off, also indicating the generation of Mn in higher oxidation states, possibly Mn(IV), induced by light irradiation [Figure 11D-F]. Similar results were observed at the Fe $L_{2,3}$-edges for the Fe-PHI catalyst, suggesting that both Fe and Mn atoms interact with photogenerated holes to produce high-valent species, which act as active centers for the selective photooxidation of toluene.

## DFT calculations

DFT calculations are extensively used to supplement the experimental findings in the field of photocatalysis[207-209]. Specifically, leveraging DFT calculations provides useful information to probe the mechanism of toluene photooxidation, encompassing substrate adsorption, C–H bond activation, intermediate migration, and product desorption[134,210,211]. This theoretical approach contributes to a deeper understanding of the reaction mechanism and also aids in the design of novel photocatalysts with improved performance. In this section, we will present several representative works that employ DFT calculations for toluene photooxidation over various photocatalysts, aiming to elucidate essential theoretical aspects that researchers should consider when investigating the selective photooxidation of toluene.

### *$O_2$ adsorption on photocatalyst surface*

The generation of ROS plays a crucial role in enhancing the performance of the photocatalyst during the catalytic conversion of toluene into high-value-added benzaldehyde. However, the activation of gaseous

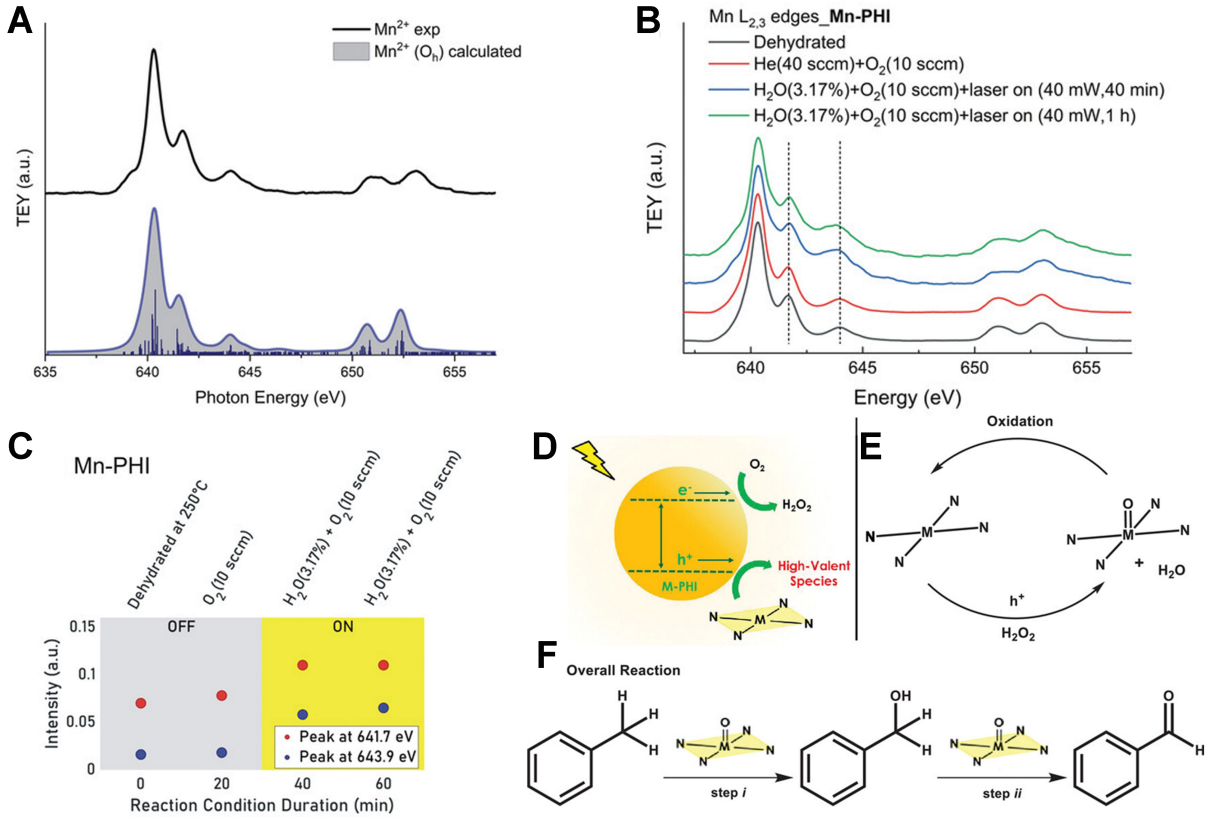


**Figure 11.** (A) XAS spectra for the $L_3$ and $L_2$ edges of Mn-PHI photocatalyst; (B) Operando XAS spectra at the Mn $L_{3,2}$-edges of Mn-PHI under various conditions; (C) Intensity of high-energy peaks at the Mn $L_3$-edges under various conditions, with yellow boxes marking the illumination periods during the photocatalytic reaction; (D) Proposed photocatalytic mechanism for the formation of hydrogen peroxide and high-valent metal species; (E) Mechanism for the generation of metal-oxo species via photogenerated holes and $H_2O_2$; (F) Photocatalytic mechanism for the oxidation of toluene into benzaldehyde through benzyl alcohol, catalyzed by iron- and manganese-oxo species. Reproduced with permission, Copyright 2023, Wiley-VCH[151].XAS: X-ray absorption spectroscopy; PHI: poly(heptazine imides).

oxygen into ROS is strongly dependent on the extent of oxygen adsorption on the photocatalyst surface[212-214]. Therefore, it is of great significance to investigate the adsorption sites of $O_2$ within the as-prepared photocatalyst during photocatalysis and correlate the behavior with the enhanced catalytic performance. Experimentally, temperature-programmed desorption with oxygen ($O_2$-TPD) and the $O_2$ adsorption isotherms are widely applied to investigate the oxygen absorption capacity of the target catalyst[215-219]. In addition to experimental techniques, DFT calculations can also provide insights into the adsorption of oxygen molecules over a simulated photocatalyst model.

For example, Li *et al.* used DFT calculations to reveal the active sites for the adsorption and activation of oxygen molecules over the as-synthesized Pd/BiOBr photocatalyst[88]. First, the adsorption energies of $O_2$ on various optimized photocatalyst models were calculated to demonstrate the likelihood of a selected model adsorbing oxygen molecules. It was revealed that the Pd/BiOBr-Vo model exhibits stronger interactions with both $O_2$ and toluene molecules compared to the BiOBr-Vo model. In the simulated Pd/BiOBr-Vo surface, the interfacial Pd sites show significantly stronger chemical interactions with oxygen compared to the BiOBr-Vo surface. On the Pd/BiOBr-Vo model, oxygen molecules can be adsorbed onto either interfacial or top Pd clusters, enabling more favorable oxygen adsorption on the photocatalyst surface [Figure 12A-C]. Since both $^{\bullet}O_2^-$ and $^1O_2$ are the dominant reactive species reacting with the adsorbed

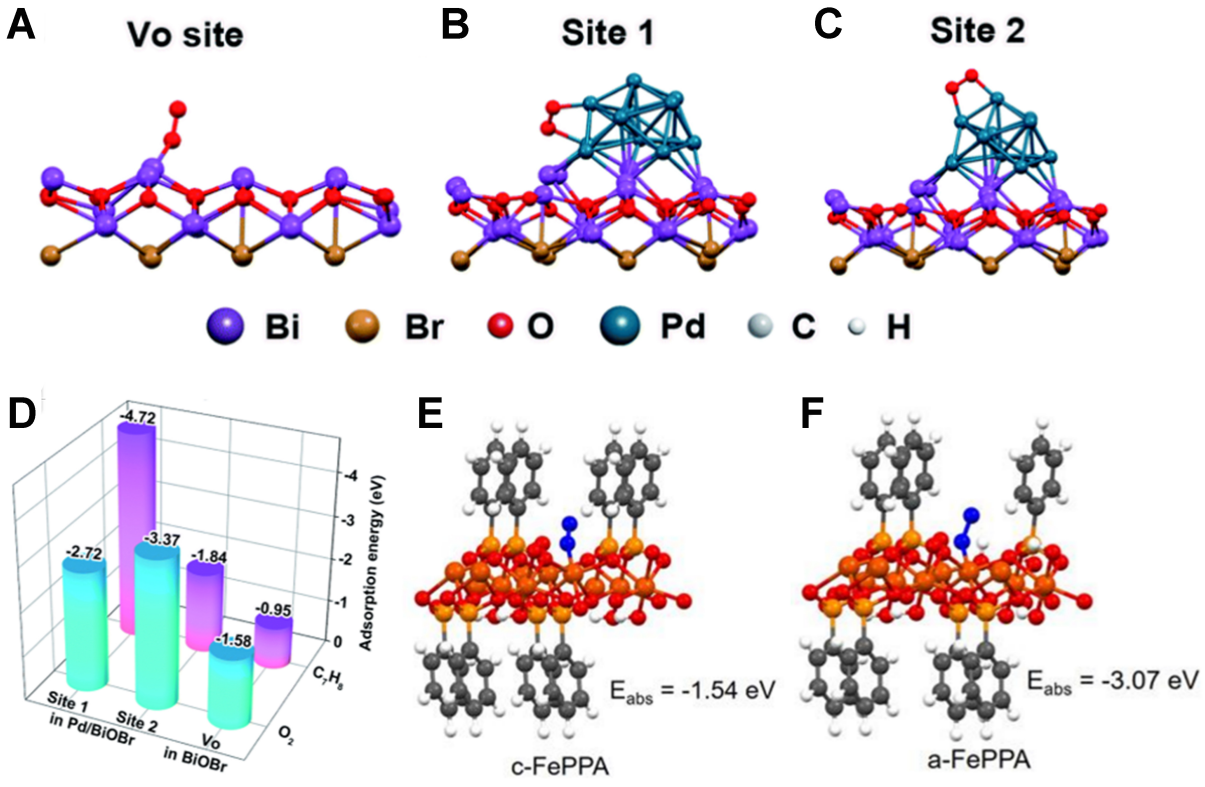


**Figure 12.** DFT-calculated local configurations for $O_2$ molecule adsorbed onto the (A) $V_O$ site in the BiOBr–$V_O$ surface; (B) interfacial Pd site (site 1) and (C) top Pd site (site 2) in the Pd/BiOBr–$V_O$ surface; (D) The adsorption energies (Ead) for $O_2$ and toluene absorbed onto the different sites. Reproduced with permission, Copyright 2020, Royal Society of Chemistry[88]. The models for $O_2$ adsorption on (E) c-FePPA and (F) a-FePPA (Fe, orange; C, gray; P, yellow; H, white; O, red; adsorbed O, blue). Reproduced with permission, Copyright 2024, Wiley-VCH[170]. DFT: Density functional theory.

toluene molecules during the photocatalytic conversion process, it is reasonable to consider that the two adsorption modes of $O_2$ on the interfacial Pd site and top Pd site exist simultaneously, which could facilitate the formation of both $^{\bullet}O_2^-$ and $^1O_2$ through the transfer of photogenerated electrons and energy, respectively. According to the calculated results, the introduction of Pd nanoparticles onto the BiOBr surfaces could enhance the chemical adsorption of $O_2$ molecules on the composite photocatalyst, ensuring efficient electron and energy transfer between the reactants and the Pd/BiOBr photocatalyst [Figure 12D].

Another study showed that the amorphization of phosphonate-based MOF photocatalysts would enhance oxygen adsorption and promote its activation for the subsequent oxidation process, as reported by Zhang *et al.*[170]. The $O_2$ adsorption isotherms revealed that a-FePPA exhibits both a higher maximum $O_2$ adsorption amount (3.13 $cm^3 \cdot g^{-1}$) and $O_2$ adsorption amount per unit of specific surface area (0.036 $cm^3 \cdot m^{-2}$) compared to c-FePPA (maximum $O_2$ adsorption amounts = 1.66 $cm^3 \cdot g^{-1}$ and $O_2$ adsorption amount per unit of specific surface area = 0.032 $cm^3 \cdot m^{-2}$). DFT calculations were performed to further evidence the experimental results [Figure 12E and F]. The model of a-FePPA, featuring distorted Fe-oxo clusters, demonstrated a greater adsorption energy of -3.07 eV as compared to the c-FePPA model (-1.54 eV), confirming that $O_2$ molecules are more readily adsorbed on the simulated a-FePPA model. The combined experimental and computational results suggested that amorphization could efficiently facilitate the adsorption of oxygen and its further activation to initiate the photooxidation process.

*Toluene adsorption on photocatalyst surface*

Efficient adsorption of toluene molecules onto the photocatalyst surface is a prerequisite for C–H bond activation. This adsorption process can be influenced by various factors, including the catalyst's surface charge distribution, surface area, and its affinity towards toluene[29,34,43]. For instance, Zhou *et al.* investigated the adsorption behavior of toluene on different facets of BiOBr semiconductor materials using DFT calculations[124]. Two computational models, where toluene molecules were placed on the surfaces of (001) and (110) facets of BiOBr, were simulated via DFT calculations. The surface sizes of photocatalyst computational models were kept consistent, measuring 24.7 × 16.72 Å (five layers) for the 001 facet and 23.65 × 15.76 Å (five layers) for the (110) facet. Since transmission electron microscopy (TEM) images could not provide direct evidence of the surface exposed atoms on the BiOBr surfaces, computational models with different terminated atoms were calculated to predict the most likely surface structure of the BiOBr photocatalyst. The calculation results showed that the (001) surface terminated with a single layer of Br atoms exhibited the lowest surface energy, suggesting this as the most likely practical surface structure for the BiOBr-(001) facet. For the BiOBr-(110) facets, the surface terminated with Bi and Br atoms exhibited the lowest surface energy, indicating the most practical surface. Therefore, the (110) facets of BiOBr are expected to expose more Bi atoms compared to the (001) facets. Charge density difference calculations were subsequently conducted to demonstrate the adsorption behavior of toluene on both facets. The results indicated a more pronounced charge distribution in the toluene adsorption model on the (110) facet, suggesting a stronger interaction between toluene molecules and the (110) facets. Moreover, it was revealed that the benzene ring in toluene is more likely to be absorbed on the Bi atoms, while the adsorption sites for its methyl group are closer to the O and Br atoms. Given that the top of the VB of BiOBr, from which the photogenerated holes originate, is primarily contributed by Br 4p and O 2p orbitals, the configuration of toluene absorbed on the (110) facets of BiOBr facilitates direct transfer of electrons from the C–H bond to the photogenerated holes, thereby achieving efficient C–H bond activation.

Similarly, Cui *et al.* used DFT calculations to investigate the adsorption of toluene over CBB and $TiO_2$/CBB photocatalysts[110]. The calculated adsorption energies of toluene on CBB and $TiO_2$/CBB were found to be -0.09 and -4.68 eV, respectively, indicating that the fabrication of the heterostructure was more favorable for toluene adsorption. Additionally, $TiO_2$/CBB exhibited a larger Brunauer-Emmett-Teller (BET) specific surface area compared to pristine CBB, thereby offering more sites for the adsorption of toluene, which was beneficial for the activation of C–H bond in the adsorbed toluene molecules and its subsequent interaction with photogenerated carriers to form reaction intermediates. Using DFT calculations, Li *et al.* established two BWO semiconductor models, one with Bi defect sites and one without, and further investigated their interactions with toluene[158]. The absorption energies of toluene were calculated to be -1.607 eV for the bulk BWO (BT) and -2.174 eV for the BT-48 photocatalysts, respectively. The enhancement in absorption energy could be attributed to the introduction of Bi defect sites within BWO materials, which strengthen the interaction between the O atom in BT-48 and the H atom from toluene, as evidenced by the reduced bond length of O–H bond.

*C–H bond activation on the photocatalyst surface*

It is widely acknowledged that the rate-limiting step in the oxidation of toluene to yield benzaldehyde is the dissociation of C($sp^3$)–H bond within toluene molecules. To estimate the ease of C($sp^3$)–H bond on various photocatalyst active sites, dissociation energy of C($sp^3$)–H bond ($E_{C\text{-}H}$) was calculated by DFT calculations. For instance, Li *et al.* used DFT calculations to investigate the dissociation of C($sp^3$)–H bond in toluene on the simulated (001) surfaces of $Cs_2AgBiBr_6$ (CABB), 3.13% Fe-CABB, and 1.56% Zn-CABB by measuring the $E_{C\text{-}H}$ values in these three computational models [Figure 13A-C][220]. Without light irradiation (i.e., no photogenerated holes produced on the photocatalyst surfaces), the $E_{C\text{-}H}$ values were determined to be 3.23,

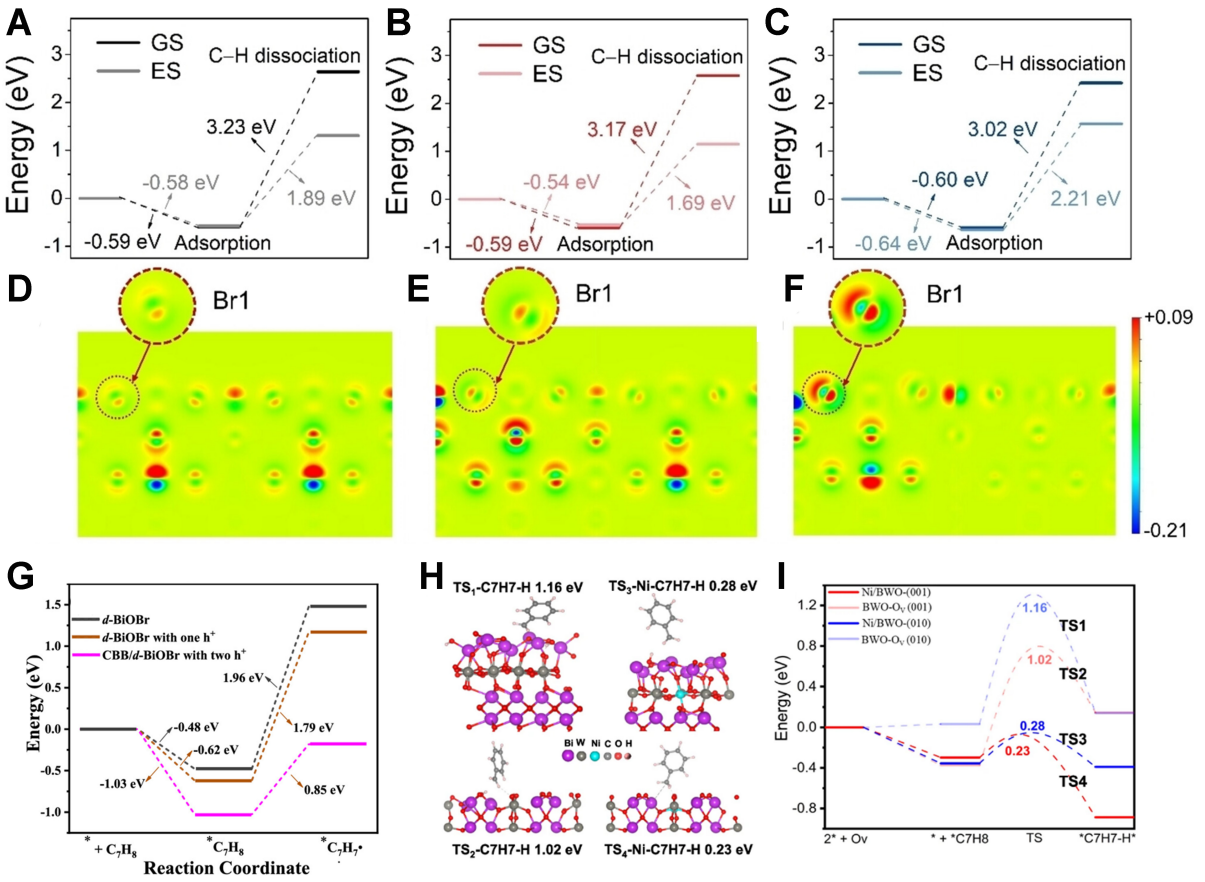


**Figure 13.** DFT calculations showing the energy changes associated with toluene adsorption and C($sp^3$)–H bond dissociation for the GS and ES of (A) CABB, (B) 1.56% Zn-CABB and (C) 3.13% Fe-CABB; The electron density colored along the (010) plane based on the density difference between the GS and ES, as depicted in (D) CABB, (E) 1.56% Zn-CABB and (F) Fe-CABB. Red circles indicate Br atoms adjacent to the substituent. Reproduced with permission, Copyright 2023, Wiley-VCH[220]; (G) DFT calculations showing the influence of surface-localized holes on toluene adsorption ($E_{ads}$) and C($sp^3$)–H bond dissociation. Reproduced with permission, Copyright 2022, American Chemical Society[178]; (H) Geometries and energies of transition state models (TS1, TS2, TS3, and TS4); (I) Calculated energy profiles of toluene adsorbed on different structure models. Reproduced with permission, Copyright 2024, Springer Nature[36]. DFT: Density functional theory; GS: ground state; ES: excited state; CABB: $Cs_2AgBiBr_6$; TS: transition state.

3.17, and 3.02 eV for CABB, 1.56% Zn-CABB, and 3.13% Fe-CABB, respectively. Such high $E_{C-H}$ values indicated that efficient C($sp^3$)–H bond activation and dissociation would not occur in the absence of photogenerated holes. In order to simulate the photocatalyst behavior under light irradiation, one electron was manually transferred from the highest occupied orbital of the catalyst system to the lowest unoccupied orbital for each k-point, thus creating a hole in the VB. The $E_{C-H}$ values were calculated as 1.89, 1.69, and 2.21 eV for CABB, 1.56% Zn-CABB, and 3.13% Fe-CABB under light irradiation, which are significantly lower compared to those under dark conditions. Among the three models, 1.56% Zn-CABB exhibited the lowest $E_{C-H}$, indicating its superior capability for the activation of C($sp^3$)–H bond in toluene, further facilitating the generation of benzyl radical, thereby accelerating the overall photooxidation process. To understand the role of active $Br^-$ sites in generating photogenerated holes and facilitating the dissociation of C($sp^3$)–H bond in toluene molecules, the electron densities of the surface $Br^-$ were modulated over diverse photocatalyst systems, and the electron density differences ($\Delta\rho$) between the excited state and ground state were subsequently analyzed [Figure 13D-F]. According to the computational results, the surface electron density at the selected Br1 site in 1.56% Zn-CABB was revealed to be significantly lower than at the Br1 sites in both the 3.13% Fe-CABB and the pristine CABB in their excited states. Benefiting from its lower surface

electron density in the excited state, the Br1 in 1.56% Zn-CABB demonstrated a stronger oxidation capability in dissociating the C($sp^3$)–H bonds under light irradiation, thereby yielding the lowest $E_{C-H}$ value and achieving the highest toluene conversion rate.

To elucidate the superior oxidation capability of Z-scheme CBB/*d*-BiOBr compared to pristine *d*-BiOBr, Bai *et al.* employed DFT calculations to explore the impact of accumulated photogenerated holes on the photocatalytic performance[178]. Two computational models were first simulated: one for *d*-BiOBr with one hole and another for CBB/*d*-BiOBr with two photogenerated holes. Then, the energy barriers for the rate-limiting step (i.e., $^*C_7H_8 + h^+ \rightarrow {}^*C_7H_7 + H^+$) were calculated on the constructed photocatalyst models [Figure 13G]. In the case of *d*-BiOBr with no holes, the energy barrier was determined to be 1.96 eV, suggesting that the activation of C($sp^3$)–H bond is rather challenging under dark conditions. For the *d*-BiOBr model with one hole, the energy barrier is only slightly reduced to 1.79 eV, indicating that the step is still not significantly promoted. In contrast, for the CBB/*d*-BiOBr model with two holes, the energy barrier was dramatically lowered to 0.85 eV, significantly lower than that of the *d*-BiOBr under the conditions. This substantial reduction in the energy barrier demonstrates that the transfer of photogenerated holes to the catalyst surface effectively facilitates the dissociation of C($sp^3$)–H bond in toluene molecules.

Similarly, Shi *et al.* prepared Ni-doped BWO (Ni/BWO) photocatalyst oxidation via a facile solvothermal method for efficient photocatalytic oxidation of toluene[36]. DFT calculations were employed to demonstrate the superiority of the as-synthesized Ni/BWO over the pristine BWO in terms of C–H bond activation in toluene molecules. As shown in Figure 13H and I, four computational models including Ni/BWO (001), Ni/BWO (010), BWO-$O_v$ (001), and BWO-$O_v$ (010) were established for calculating the activation path of C–H bond in toluene. The energy barriers for the dehydrogenation of toluene on the four models were calculated to be 0.23, 0.28, 1.02, and 1.16 eV for Ni/BWO (001), Ni/BWO (010), BWO-$O_v$ (001), and BWO-$O_v$ (010), respectively, indicating that the Ni/BWO photocatalysts exhibit higher activity due to the integration of Ni dopants on the BWO substrates. Notably, toluene dehydrogenation was more easily achieved on the Ni/BWO (001) model, which can be explained by the formation of Bi···C and O···H coordination between frustrated Lewis pairs (FLP) and the C–H bond. The transient charge density difference image of transition state (TS)-4 showed that the coordination led to the transfer of electrons from the H atoms in the C–H bond to the O atoms and from the Bi atoms to the C atoms, resulting in effective activation of C–H bonds.

*Screening of intermediates during toluene photooxidation process*

To elucidate the photooxidation pathways and intermediates involved in the photocatalytic conversion of toluene to benzaldehyde, DFT calculations were conducted to offer valuable atomistic insights into the mechanisms underlying the photocatalytic oxidation process over certain photocatalysts. For instance, Zhou *et al.* employed DFT calculations to simulate the potential reaction pathways following the dissociation of C–H bonds over EC-BiOBr, based on the detection of intermediate products[124]. As illustrated in Figure 14A and B, the oxidation of absorbed benzyl radical ($^*PhCH_2^\bullet$) to $^*PhCH_2OO^-$ by $^\bullet O_2^-$ was exothermic (ΔG = -0.82 eV), while its oxidation to $^*PhCH_2OO^\bullet$ was endothermic by $O_2$ (ΔG = 2.0 eV) under standard conditions (atmospheric pressure and room temperature). Subsequently, $^*PhCH_2OO^-$ could spontaneously form $^*PhCH_2OOH$ (ΔG = -1.76 eV), whereas the reaction between $^*PhCH_2OO^\bullet$ and toluene to generate $^*PhCH_2OOH$ appeared to be challenging (ΔG = 0.89 eV). Following the formation of $^*PhCH_2OOH$, it undergoes an autonomous conversion into benzaldehyde (ΔG = -2.90 eV). However, the production of benzaldehyde and benzyl alcohol from $^*PhCH_2OOH$ was calculated to be highly unfavorable (ΔG = 27.31 eV). The obtained results indicate that $^\bullet O_2^-$ was the primary oxidizing species for the conversion of benzyl radical to benzaldehyde, rather than $O_2$ molecules.

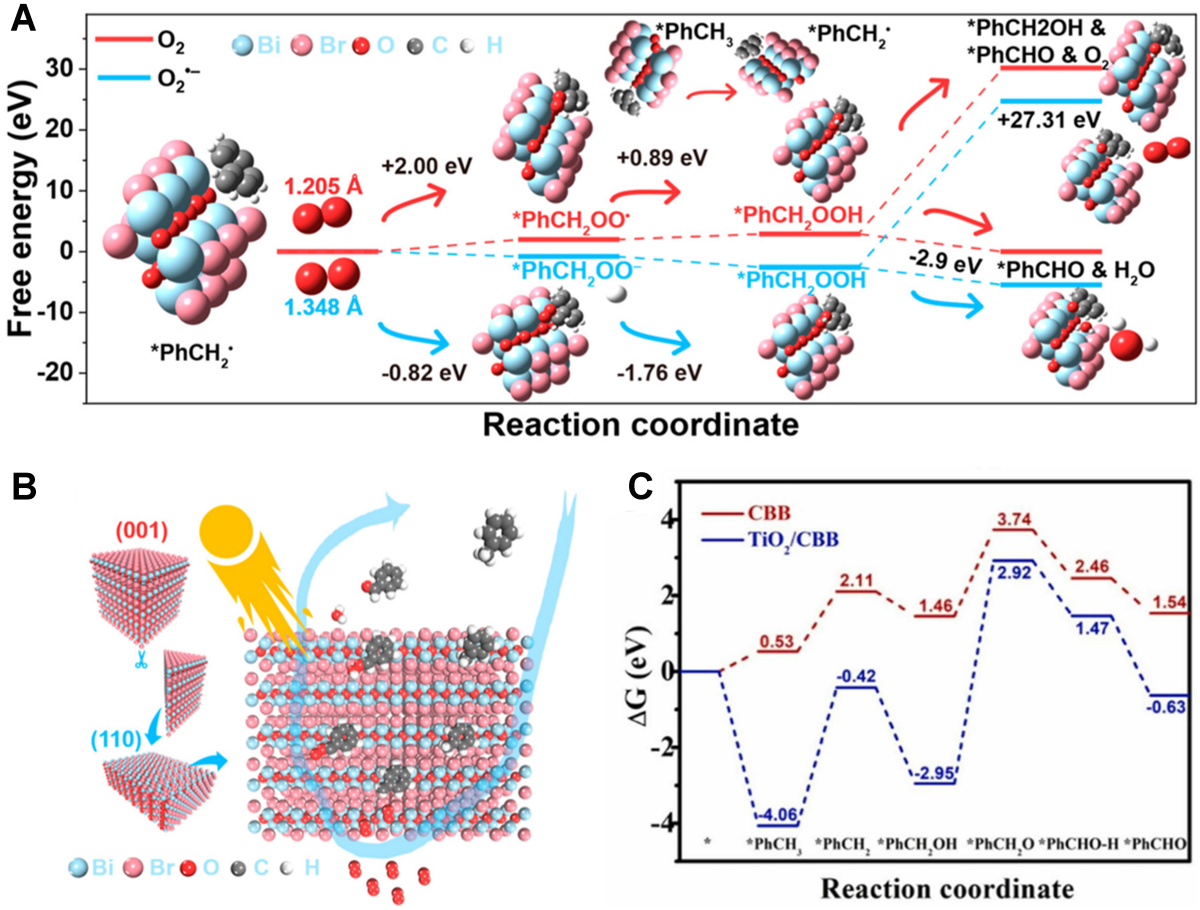


**Figure 14.** (A) Proposed reaction mechanism of benzyl radical oxidation over EC-BiOBr according to DFT calculations. The asterisk (*) denotes the adsorption site on the substrate; (B) Schematic illustrating the toluene oxidation mechanism over EC-BiOBr photocatalyst. Reproduced with permission, Copyright 2024, American Chemical Society[124]; (C) Gibbs free energy profiles of photocatalytic toluene oxidation over pure CBB and $TiO_2$/CBB. Reproduced with permission, Copyright 2023, Elsevier[110]. EC: (110) facet-exposed; DFT: density functional theory; CBB: $Cs_3Bi_2Br_9$.

Cui *et al.* used DFT calculations to model the interactions of CBB and $TiO_2$/CBB with each intermediate during the photocatalytic conversion of toluene[110]. The Gibbs free energy (ΔG) for each reaction step, as shown in Figure 14C, was calculated. The results indicated that the formation of benzyl radicals derived from toluene is the rate-determining step during the photocatalytic toluene conversion reaction, with $TiO_2$/CBB exhibiting a lower benzyl formation energy than that over pristine CBB. After dehydrogenation, the benzyl radical reacted with the generated $^{\bullet}O_2^-$ to form $^*PhCH_2OH$ intermediates. Benzaldehyde was then produced from $^*PhCH_2OH$ intermediates via two successive dehydrogenation steps, involving the dissociation of the O–H bond within the -OH structure and the C–H bond within the methyl structure.

*Desorption of benzaldehyde products over photocatalyst surface*

In addition to the efficient adsorption of reactants and the rapid generation of intermediates over the photocatalyst surface, the desorption of products is another key factor determining the catalytic performance of certain photocatalysts. Experimentally, benzaldehyde-TPD is generally considered an effective technique for characterizing the affinity of catalysts for benzaldehyde. As demonstrated by Wang *et al.*, the broad desorption peak (m/z = 51, 106) observed at low temperatures (100 to 300 °C) corresponds to the chemisorption of benzaldehyde on the photocatalysts[159]. In contrast, the desorption peak (m/z = 51) at

high temperatures (over 400 °C) can be ascribed to the decarbonylation of benzaldehyde to benzene over the catalysts. The rapid desorption of benzaldehyde from the photocatalysts can prevent the overoxidation of benzaldehyde, thereby explaining the high selectivity for benzaldehyde during the photocatalytic process. To complement the experimental results, DFT calculations are carried out to offer insights into the desorption of benzaldehyde over the computational models by providing the desorption energy of benzaldehyde.

For example, Zhou *et al.* prepared a $Cs_3Bi_2Br_{9-x}$@AgBr core-shell heterojunction photocatalysts via an *in situ* light-assisted $Ag^+$ insertion procedure[111]. To investigate the desorption profiles of $Cs_3Bi_2Br_{9-x}$@AgBr and pristine CBB photocatalysts, DFT calculations were conducted to determine the benzaldehyde desorption energies for both photocatalyst models. The results showed that $V_{Br}$-CBB exhibited a lower desorption energy of benzaldehyde compared to pristine CBB (1.59 *vs.* 1.65 eV), indicating that the introduction of bromide-vacancy sites could effectively prevent the overoxidation of benzaldehyde by facilitating the desorption of benzaldehyde over the active sites. Similarly, Shi *et al.* introduced Ni dopants into the monolayered BWO, creating cascaded active sites that consist of unsaturated W atoms and Bi/O FLP within the resulting Ni/BWO photocatalysts[36]. Experimentally, the as-prepared Ni/BWO exhibited higher toluene conversion rate and increased selectivity for benzaldehyde compared to the pristine BWO. DFT results revealed that the benzaldehyde desorption energies for Ni/BWO-(001) and BWO-(001) were 0.41 and 0.69 eV, respectively, indicating a more facile desorption process on the Ni/BWO-(001) model. The finding offered a plausible explanation for the enhanced selectivity towards benzaldehyde using the optimized 1.8Ni/BWO photocatalyst over the undoped BWO.

## CONCLUSION AND OUTLOOK

In light of the advancements in photocatalytic toluene oxidation, this review highlights the intricate mechanisms underlying C–H bond activation and the role of ROS in optimizing photocatalytic efficiency. We also provide a thorough analysis of strategies developed to enhance the selectivity and activity of specific photocatalysts under reaction conditions. Additionally, theoretical perspectives have been concluded to provide valuable insights into the energetics and reaction mechanisms governing the photocatalytic processes. Despite significant progress, the overall conversion of toluene under visible light irradiation still requires enhancement, and a comprehensive understanding of the reaction mechanisms remains elusive, emphasizing the ongoing need for innovative approaches to catalyst design and advanced characterization.

Future research should prioritize the development of novel photocatalysts that can effectively harness the dynamics of photogenerated charge carriers while minimizing limitations related to efficiency and selectivity. By integrating experimental findings with theoretical insights, researchers can address the existing gaps in knowledge and drive the evolution of photocatalytic systems. Ultimately, this review aims to foster new directions in the field, paving the way for more efficient and sustainable photocatalytic applications, as outlined below.

### Machine learning in novel photocatalyst discovery

Machine learning (ML) is driving transformative advancements in material science, particularly in the realm of discovering and optimizing novel photocatalysts[40,221,222]. This technology optimizes the entire process, from collecting and preparing data to selecting features, training models, making predictions, and testing performance. By efficiently navigating the expansive chemical space, ML stands to significantly reduce the time and costs traditionally associated with identifying new photocatalysts. However, several challenges remain unsolvable. Ensuring the quality and quantity of data across the research community is crucial for improving model accuracy and reproducibility. Additionally, developing interpretable ML models is

essential for gaining deeper insights into the intricate mechanisms underlying photocatalytic activity, thereby facilitating knowledge transfer and innovation. Integrating ML seamlessly into experimental workflows to create automated systems that continuously refine predictions through feedback loops is another critical challenge. Moreover, enhancing the ability of ML models to generalize knowledge across different photocatalytic systems through techniques such as transfer learning promises to broaden their applicability and impact. Despite these challenges, ML holds immense promise in revolutionizing the discovery and optimization of photocatalysts, enabling researchers to accelerate the development of next-generation materials that offer superior performance and sustainability benefits.

### Development of novel *In situ* photocatalytic characterization techniques

*In situ* characterization techniques represent pivotal tools in the quest to unravel the intricate dynamics occurring on photocatalyst surfaces during chemical reactions[180,223,224]. These methods provide invaluable real-time insights into reaction mechanisms, the formation of intermediate species, and the behavior of catalysts under diverse operational conditions. By offering a direct view into the complexities of photocatalytic processes, these techniques are indispensable for guiding the development and optimization of photocatalysts aimed at achieving enhanced efficiency and stability.

The current landscape of *in situ* characterization, while highly impactful, faces notable challenges, particularly in its ability to monitor catalytic processes at the atomic and molecular scales. This limitation underscores a pressing need for more advanced and versatile methodologies. Advanced techniques such as *in situ* scanning/transmission electron microscopy (STEM/TEM), XAS, and vibrational spectroscopy (e.g., infrared and Raman spectroscopy) are increasingly recognized as essential for achieving finer spatial and temporal resolution. These tools enable researchers not only to observe catalysts in action but also to probe the intricate details of their surface chemistry and electronic structure with unprecedented precision.

By bridging the gap between static characterization techniques and real-time, atomic-scale observations, ongoing advancements in *in situ* characterization technologies promise to catalyze significant innovation in photocatalysis. They facilitate a deeper understanding of fundamental processes such as charge carrier dynamics, surface adsorption-desorption kinetics, and interface reactions, which are pivotal for optimizing photocatalytic performance. Moreover, these techniques play a crucial role in addressing critical challenges facing photocatalysis, including improving selectivity, durability, and overall efficiency in energy conversion and environmental remediation applications. Looking forward, the continued evolution and integration of advanced *in situ* characterization techniques are poised to transform the field of photocatalysis. By empowering researchers to tailor the properties and functionalities of photocatalysts with unprecedented precision, these technologies hold immense potential for advancing sustainable energy technologies and addressing pressing global challenges related to clean water, air quality, and renewable energy production. As such, investments in further research and development of these methodologies are crucial for unlocking the full promise of photocatalysis in the pursuit of a more sustainable future.

### The reaction mechanism of toluene selective oxidation remains unclear

Although researchers have now demonstrated that ROS are important reactive intermediates and thus involved in the reaction, more details of the reaction remain obscure[35,51,225]. The selective oxidation of toluene molecules to yield benzaldehyde or benzoic acid is a complex process governed by the interaction between toluene molecules and metal oxide catalysts. Catalysts such as titanium and molybdenum oxides play a crucial role in activating molecular oxygen, which initiates the oxidation sequence[159]. Initially, toluene adsorbs onto the catalyst surface, where it undergoes activation through interactions with the metal centers. The oxidation process typically begins with the abstraction of a hydrogen atom from the methyl group of toluene, forming benzyl radicals or benzyl cations as key intermediates. These reactive species then

react with oxygen species adsorbed on the catalyst surface, resulting in the formation of benzyl peroxides. The fate of these peroxides determines the final products: benzaldehyde can be formed directly through the decomposition of the benzyl peroxides, while further oxidation steps can yield benzoic acid.

The selectivity of these transformations depends on several factors, including the catalyst composition, structure, and surface properties, as well as the reaction conditions such as temperature, pressure, and the partial pressures of toluene and oxygen. Catalysts are often tailored to enhance specific reaction pathways, aiming to maximize yields of desired products while minimizing the formation of by-products such as benzyl alcohol and carbon dioxide. Understanding and controlling these mechanisms are critical for optimizing the efficiency and selectivity of toluene oxidation processes in industrial applications, where these chemicals are vital for pharmaceuticals, fragrances, and other fine chemical manufacturing. Advanced spectroscopic and computational techniques play a significant role in elucidating these complex mechanisms and guiding catalyst design and process optimization efforts.

### Development of additional tandem/coupling reactions based on oxidation

The development of tandem/coupling reactions based on toluene oxidation represents a promising area of research in synthetic organic chemistry. Toluene can undergo various oxidative transformations to yield valuable intermediates for further chemical reactions[226,227]. These reactions include oxidative cross-coupling, oxidative cyclization, and one-pot oxidation and coupling.

For example, benzyl alcohol obtained from the oxidation of toluene can be coupled with amines to form secondary amines or imines using metal or organocatalysts[228]. Benzaldehyde, derived from toluene oxidation, can participate in aldol reactions with ketones or other aldehydes to form β-hydroxy ketones or aldehydes[229]. Additionally, direct oxidation of toluene to benzyl alcohol, followed by coupling with aryl halides using Ni catalysts, can form diarylmethane structures in a single pot[230]. Despite significant progress, several challenges remain in the development of tandem/coupling reactions based on toluene oxidation. Achieving high selectivity and precise control over oxidation states and product distribution is a major hurdle. Research needs to focus on sustainable catalysis, developing environmentally friendly systems using non-toxic oxidants and renewable energy sources such as visible light. A deeper mechanistic understanding of these reactions will aid in designing more efficient catalytic systems. Additionally, applying these reactions to the synthesis of complex natural products, pharmaceuticals, and materials will demonstrate their practical utility and drive further advancements. Addressing these challenges will enable continued progress and new opportunities for efficient and selective synthesis in organic chemistry.

### Promoting the industrialization of photocatalytic reactions

Promoting the industrialization of photocatalytic reactions involves several critical steps to bridge the gap between laboratory research and large-scale industrial applications. The first principle is the improvement of photocatalyst efficiency, which includes material innovation, nanostructuring, and doping and the formation of composites. Second, reaction conditions should be optimized for industrial methods, such as reactor design, light source optimization, and operational parameters. Third, scalability and process integration should be firmly organized in industrial processes. Pilot plants should be established to test the scalability of photocatalytic processes and address any unforeseen issues that may arise during scaling up. Meanwhile, photocatalytic processes should be integrated with existing industrial systems to utilize waste streams and existing infrastructure. Fourth, economic viability is an important indicator of business investment. Reducing the cost of photocatalyst production and the overall process can be achieved through material innovations, efficient manufacturing processes, and economies of scale. Moreover, comprehensive techno-economic analyses should be performed to evaluate the feasibility and profitability of the industrialized processes.

## DECLARATIONS

### Authors' contributions

Prepared and revised the manuscript: Gao S, Wang B
Revised the manuscript: Bai L, Gan T, Wang B

### Availability of data and materials

A chart comparing the catalytic performance of various photocatalysts in photocatalytic toluene oxidation is available in the Supplementary Materials. No new data was generated in this article.

### Financial support and sponsorship

This work was supported by the National Natural Science Foundation of China (22205073).

### Conflicts of interest

All authors declared that there are no conflicts of interest.

### Ethical approval and consent to participate

Not applicable.

### Consent for publication

Not applicable.



## REFERENCES

1. Mu, Y.; Williams, P. T. Recent advances in the abatement of volatile organic compounds (VOCs) and chlorinated-VOCs by non-thermal plasma technology: a review. *Chemosphere* **2022**, *308*, 136481. DOI PubMed
2. Mangotra, A.; Singh, S. K. Volatile organic compounds: a threat to the environment and health hazards to living organisms - a review. *J. Biotechnol.* **2024**, *382*, 51-69. DOI PubMed
3. Siu, B.; Chowdhury, A. R.; Yan, Z.; Humphrey, S. M.; Hutter, T. Selective adsorption of volatile organic compounds in metal-organic frameworks (MOFs). *Coord. Chem. Rev.* **2023**, *485*, 215119. DOI
4. Sheng, Y.; Wang, M.; Dong, Q. Gas-particle two-phase adsorption of toluene and ultrafine particles on activated carbon studied by molecular simulation. *Sci. Total. Environ.* **2023**, *891*, 164591. DOI
5. Huang, S.; Deng, W.; Zhang, L.; et al. Adsorptive properties in toluene removal over hierarchical zeolites. *Micropor. Mesopor. Mat.* **2020**, *302*, 110204. DOI
6. Bal'zhinimaev, B. S.; Paukshtis, E. A.; Toktarev, A. V.; et al. Effect of water on toluene adsorption over high silica zeolites. *Micropor. Mesopor. Mat.* **2019**, *277*, 70-7. DOI
7. Wang, R.; Luan, X.; Yaseen, M.; et al. Swellable array strategy based on designed flexible double hypercross-linked polymers for synergistic adsorption of toluene and formaldehyde. *Environ. Sci. Technol.* **2023**, *57*, 6682-94. DOI
8. Wu, P.; Jin, X.; Qiu, Y.; Ye, D. Recent progress of thermocatalytic and photo/thermocatalytic oxidation for VOCs purification over manganese-based oxide catalysts. *Environ. Sci. Technol.* **2021**, *55*, 4268-86. DOI PubMed
9. Li, A.; Zhang, Q.; Zhao, S.; et al. A dual plasmonic core - shell Pt/[TiN@$TiO_2$] catalyst for enhanced photothermal synergistic catalytic activity of VOCs abatement. *Nano. Res.* **2022**, *15*, 7071-80. DOI
10. Luo, Y.; Chi, Z.; Zhang, J.; Tian, B. Photothermocatalytic system designed by facet-heterojunction to enhance the synergistic effect of toluene oxidation. *ChemCatChem* **2022**, *14*, e202101958. DOI
11. Zhang, Y.; Wu, M.; Wang, Y.; et al. Fluorinated $TiO_2$ coupling with α-$MnO_2$ nanowires supported on different substrates for photocatalytic VOCs abatement under vacuum ultraviolet irradiation. *Appl. Catal. B. Environ.* **2021**, *280*, 119388. DOI
12. Stucchi, M.; Bianchi, C.; Pirola, C.; et al. Surface decoration of commercial micro-sized $TiO_2$ by means of high energy ultrasound: a way to enhance its photocatalytic activity under visible light. *Appl. Catal. B. Environ.* **2015**, *178*, 124-32. DOI
13. Zhang, L.; Peng, Y.; Zhang, J.; Chen, L.; Meng, X.; Xiao, F. Adsorptive and catalytic properties in the removal of volatile organic compounds over zeolite-based materials. *Chinese. J. Catal.* **2016**, *37*, 800-9. DOI
14. Guo, Y.; Wen, M.; Li, G.; An, T. Recent advances in VOC elimination by catalytic oxidation technology onto various nanoparticles catalysts: a critical review. *Appl. Catal. B. Environ.* **2021**, *281*, 119447. DOI
15. He, C.; Cheng, J.; Zhang, X.; Douthwaite, M.; Pattisson, S.; Hao, Z. Recent advances in the catalytic oxidation of volatile organic

compounds: a review based on pollutant sorts and sources. *Chem. Rev.* **2019**, *119*, 4471-568. DOI

16. Vandenbroucke, A. M.; Morent, R.; De, G. N.; Leys, C. Non-thermal plasmas for non-catalytic and catalytic VOC abatement. *J. Hazard. Mater.* **2011**, *195*, 30-54. DOI PubMed
17. Chen, H. L.; Lee, H. M.; Chen, S. H.; Chang, M. B.; Yu, S. J.; Li, S. N. Removal of volatile organic compounds by single-stage and two-stage plasma catalysis systems: a review of the performance enhancement mechanisms, current status, and suitable applications. *Environ. Sci. Technol.* **2009**, *43*, 2216-27. DOI PubMed
18. Chung, W.; Mei, D.; Tu, X.; Chang, M. Removal of VOCs from gas streams via plasma and catalysis. *Catal. Rev.* **2019**, *61*, 270-331. DOI
19. Lapa, H. M.; Martins, L. M. D. R. S. Toluene oxidation: $CO_2$ vs benzaldehyde: current status and future perspectives. *ACS. Omega.* **2024**, *9*, 26780-804. DOI PubMed PMC
20. Loch, C.; Reusch, H.; Ruge, I.; et al. Benzaldehyde in cherry flavour as a precursor of benzene formation in beverages. *Food. Chem.* **2016**, *206*, 74-7. DOI
21. Kesavan, L.; Tiruvalam, R.; Ab, R. M. H.; et al. Solvent-free oxidation of primary carbon-hydrogen bonds in toluene using Au-Pd alloy nanoparticles. *Science* **2011**, *331*, 195-9. DOI PubMed
22. Huang, X. Q.; Li, R.; Fu, J.; Dudareva, N. A peroxisomal heterodimeric enzyme is involved in benzaldehyde synthesis in plants. *Nat. Commun.* **2022**, *13*, 1352. DOI PubMed PMC
23. Li, H.; Meng, Y.; Shu, C.; Li, X.; Kiss, A. A.; Gao, X. Innovative reactive distillation process for the sustainable synthesis of natural benzaldehyde. *ACS. Sustain. Chem. Eng.* **2018**, *6*, 14114-24. DOI
24. Zhu, D.; Hai, J.; Wang, L.; Long, X. A study on the oxidation of toluene to benzaldehyde by air catalyzed by polyoxometalate loaded on activated carbon. *Mol. Catal.* **2023**, *551*, 113626. DOI
25. Huang, H.; Fan, H.; Ge, Y.; et al. Solvent-free oxidation of toluene to benzaldehyde using electron-rich Au clusters confined in silicalite-1. *Chem. Eng. J.* **2023**, *458*, 141446. DOI
26. Wu, X.; Deng, Z.; Yan, J.; Zhang, F.; Zhang, Z. Effect of acetic anhydride on the oxidation of toluene to benzaldehyde with metal/bromide catalysts. *Ind. Eng. Chem. Res.* **2014**, *53*, 14601-6. DOI
27. Cao, X.; Han, T.; Peng, Q.; Chen, C.; Li, Y. Modifications of heterogeneous photocatalysts for hydrocarbon C-H bond activation and selective conversion. *Chem. Commun.* **2020**, *56*, 13918-32. DOI PubMed
28. Chengula, P. J.; Charles, H.; Pawar, R. C.; Lee, C. S. Current trends on dry photocatalytic oxidation technology for BTX removal: viable light sources and highly efficient photocatalysts. *Chemosphere* **2024**, *351*, 141197. DOI PubMed
29. Chen, R.; Li, J.; Wang, H.; et al. Photocatalytic reaction mechanisms at a gas–solid interface for typical air pollutant decomposition. *J. Mater. Chem. A.* **2021**, *9*, 20184-210. DOI
30. Yang, Y.; Zhao, S.; Cui, L.; et al. Recent advancement and future challenges of photothermal catalysis for VOCs elimination: from catalyst design to applications. *Green. Energy. Environ.* **2023**, *8*, 654-72. DOI
31. Ge, H.; Chen, G.; Yuan, Q.; Li, H. Gas phase partial oxidation of toluene over modified $V_2O_5/TiO_2$ catalysts in a microreactor. *Chem. Eng. J.* **2007**, *127*, 39-46. DOI
32. Genuino, H. C.; Dharmarathna, S.; Njagi, E. C.; Mei, M. C.; Suib, S. L. Gas-phase total oxidation of benzene, toluene, ethylbenzene, and xylenes using shape-selective manganese oxide and copper manganese oxide catalysts. *J. Phys. Chem. C.* **2012**, *116*, 12066-78. DOI
33. Brückner, A. A new approach to study the gas-phase oxidation of toluene: probing active sites in vanadia-based catalysts under working conditions. *Appl. Catal. A. Gen.* **2000**, *200*, 287-97. DOI
34. Zhang, Y.; Wang, Y.; Xie, R.; et al. Photocatalytic oxidation for volatile organic compounds elimination: from fundamental research to practical applications. *Environ. Sci. Technol.* **2022**, *56*, 16582-601. DOI
35. Xiong, L.; Tang, J. Strategies and challenges on selectivity of photocatalytic oxidation of organic substances. *Adv. Energy. Mater.* **2021**, *11*, 2003216. DOI
36. Shi, Y.; Li, P.; Chen, H.; et al. Photocatalytic toluene oxidation with nickel-mediated cascaded active units over $Ni/Bi_2WO_6$ monolayers. *Nat. Commun.* **2024**, *15*, 4641. DOI PubMed PMC
37. Zhang, L.; Zhang, J.; Yu, H.; Yu, J. Emerging S-scheme photocatalyst. *Adv. Mater.* **2022**, *34*, e2107668. DOI
38. Chai, Z. Heterogeneous photocatalytic strategies for $C(sp^3)$-H activation. *Angew. Chem. Int. Ed. Engl.* **2024**, *63*, e202316444. DOI PubMed
39. He, T.; Zhao, Y. Covalent organic frameworks for energy conversion in photocatalysis. *Angew. Chem. Int. Ed. Engl.* **2023**, *62*, e202303086. DOI PubMed
40. Mai, H.; Le, T. C.; Chen, D.; Winkler, D. A.; Caruso, R. A. Machine learning for electrocatalyst and photocatalyst design and discovery. *Chem. Rev.* **2022**, *122*, 13478-515. DOI
41. Chen, H.; Nanayakkara, C. E.; Grassian, V. H. Titanium dioxide photocatalysis in atmospheric chemistry. *Chem. Rev.* **2012**, *112*, 5919-48. DOI PubMed
42. da Costa Filho BM, Vilar VJ. Strategies for the intensification of photocatalytic oxidation processes towards air streams decontamination: a review. *Chem. Eng. J.* **2020**, *391*, 123531. DOI
43. Liang, C.; Li, C.; Zhu, Y.; et al. Recent advances of photocatalytic degradation for BTEX: materials, operation, and mechanism. *Chem. Eng. J.* **2023**, *455*, 140461. DOI
44. MiarAlipour, S.; Friedmann, D.; Scott, J.; Amal, R. $TiO_2$/porous adsorbents: recent advances and novel applications. *J. Hazard.*

*Mater.* **2018**, *341*, 404-23. DOI PubMed
45. Wu, J.; Alipouri, Y.; Luo, H.; Zhong, L. Ultraviolet photocatalytic oxidation technology for indoor volatile organic compound removal: a critical review with particular focus on byproduct formation and modeling. *J. Hazard. Mater.* **2022**, *421*, 126766. DOI PubMed
46. Zheng, Y.; Fu, K.; Yu, Z.; Su, Y.; Han, R.; Liu, Q. Oxygen vacancies in a catalyst for VOCs oxidation: synthesis, characterization, and catalytic effects. *J. Mater. Chem. A.* **2022**, *10*, 14171-86. DOI
47. Cao, X.; Chen, Z.; Lin, R.; et al. A photochromic composite with enhanced carrier separation for the photocatalytic activation of benzylic C–H bonds in toluene. *Nat. Catal.* **2018**, *1*, 704-10. DOI
48. Teng, Z.; Zhang, Z.; Yang, H.; Zhang, Q.; Ohno, T.; Su, C. Atomically isolated $Sb(CN)_3$ on $sp^2$-c-COFs with balanced hydrophilic and oleophilic sites for photocatalytic C-H activation. *Sci. Adv.* **2024**, *10*, eadl5432. DOI PubMed PMC
49. Das, A.; Mandal, I.; Venkatramani, R.; Dasgupta, J. Ultrafast photoactivation of C-H bonds inside water-soluble nanocages. *Sci. Adv.* **2019**, *5*, eaav4806. DOI PubMed PMC
50. Li, F.; Tian, D.; Fan, Y.; et al. Chiral acid-catalysed enantioselective C-H functionalization of toluene and its derivatives driven by visible light. *Nat. Commun.* **2019**, *10*, 1774. DOI PubMed PMC
51. Nosaka, Y.; Nosaka, A. Y. Generation and detection of reactive oxygen species in photocatalysis. *Chem. Rev.* **2017**, *117*, 11302-36. DOI PubMed
52. Wang, H.; Chen, S.; Yong, D.; et al. Giant electron-hole interactions in confined layered structures for molecular oxygen activation. *J. Am. Chem. Soc.* **2017**, *139*, 4737-42. DOI
53. He, W.; Kim, H. K.; Wamer, W. G.; Melka, D.; Callahan, J. H.; Yin, J. J. Photogenerated charge carriers and reactive oxygen species in ZnO/Au hybrid nanostructures with enhanced photocatalytic and antibacterial activity. *J. Am. Chem. Soc.* **2014**, *136*, 750-7. DOI PubMed
54. Yuan, J. P.; Guan, Z. J.; Lin, H. Y.; et al. Modeling the enzyme specificity by molecular cages through regulating reactive oxygen species evolution. *Angew. Chem. Int. Ed. Engl.* **2023**, *62*, e202303896. DOI PubMed
55. Gao, K.; Cheng, Y.; Zhang, Z.; et al. Guest-regulated generation of reactive oxygen species from porphyrin-based multicomponent metallacages for selective photocatalysis. *Angew. Chem. Int. Ed. Engl.* **2024**, *63*, e202319488. DOI PubMed
56. Zhang, N.; Ciriminna, R.; Pagliaro, M.; Xu, Y. J. Nanochemistry-derived $Bi_2WO_6$ nanostructures: towards production of sustainable chemicals and fuels induced by visible light. *Chem. Soc. Rev.* **2014**, *43*, 5276-87. DOI PubMed
57. Ponseca, C. S. J.; Chábera, P.; Uhlig, J.; Persson, P.; Sundström, V. Ultrafast electron dynamics in solar energy conversion. *Chem. Rev.* **2017**, *117*, 10940-1024. DOI PubMed
58. Zhang, P.; Wang, T.; Chang, X.; Gong, J. Effective charge carrier utilization in photocatalytic conversions. *Acc. Chem. Res.* **2016**, *49*, 911-21. DOI PubMed
59. Li, X.; Yu, J.; Jaroniec, M. Hierarchical photocatalysts. *Chem. Soc. Rev.* **2016**, *45*, 2603-36. DOI
60. Xue, Z.; Yang, J.; Ma, L.; et al. Efficient benzylic C–H bond activation over single-atom yttrium supported on $TiO_2$ *via* facilitated molecular oxygen and surface lattice oxygen activation. *ACS. Catal.* **2024**, *14*, 249-61. DOI
61. Chen, X.; Tian, X.; Shin, I.; Yoon, J. Fluorescent and luminescent probes for detection of reactive oxygen and nitrogen species. *Chem. Soc. Rev.* **2011**, *40*, 4783-804. DOI
62. Hayyan, M.; Hashim, M. A.; AlNashef, I. M. Superoxide ion: generation and chemical implications. *Chem. Rev.* **2016**, *116*, 3029-85. DOI PubMed
63. Zhang, H.; Zhong, W.; Gong, Q.; et al. Photo-driven iron-induced non-oxidative coupling of methane to ethane. *Angew. Chem. Int. Ed. Engl.* **2023**, *62*, e202303405. DOI
64. Li, M.; Yu, S.; Huang, H.; et al. Unprecedented eighteen-faceted BiOCl with a ternary facet junction boosting cascade charge flow and photo-redox. *Angew. Chem. Int. Ed. Engl.* **2019**, *58*, 9517-21. DOI
65. Huang, H.; Tu, S.; Zeng, C.; Zhang, T.; Reshak, A. H.; Zhang, Y. Macroscopic polarization enhancement promoting photo- and piezoelectric-induced charge separation and molecular oxygen activation. *Angew. Chem. Int. Ed. Engl.* **2017**, *56*, 11860-4. DOI PubMed
66. Cao, X.; Huang, A.; Liang, C.; et al. Engineering lattice disorder on a photocatalyst: photochromic BiOBr nanosheets enhance activation of aromatic C-H bonds via water oxidation. *J. Am. Chem. Soc.* **2022**, *144*, 3386-97. DOI PubMed
67. Zhao, X.; He, S.; Wang, J.; et al. Near-infrared self-assembled hydroxyl radical generator based on photoinduced cascade electron transfer for hypoxic tumor phototherapy. *Adv. Mater.* **2023**, *35*, e2305163. DOI
68. Luo, L.; Luo, J.; Li, H.; et al. Water enables mild oxidation of methane to methanol on gold single-atom catalysts. *Nat. Commun.* **2021**, *12*, 1218. DOI PubMed PMC
69. Song, H.; Meng, X.; Wang, S.; et al. Direct and selective photocatalytic oxidation of $CH_4$ to oxygenates with $O_2$ on cocatalysts/ZnO at room temperature in water. *J. Am. Chem. Soc.* **2019**, *141*, 20507-15. DOI PubMed
70. Huang, Z.; Luo, N.; Zhang, C.; Wang, F. Radical generation and fate control for photocatalytic biomass conversion. *Nat. Rev. Chem.* **2022**, *6*, 197-214. DOI PubMed
71. Zhou, Y.; Zhang, L.; Wang, W. Direct functionalization of methane into ethanol over copper modified polymeric carbon nitride via photocatalysis. *Nat. Commun.* **2019**, *10*, 506. DOI PubMed PMC
72. Lin, G.; Ding, H.; Chen, R.; Peng, Z.; Wang, B.; Wang, C. 3D porphyrin-based covalent organic frameworks. *J. Am. Chem. Soc.* **2017**, *139*, 8705-9. DOI

73. Chen, X.; Addicoat, M.; Jin, E.; et al. Locking covalent organic frameworks with hydrogen bonds: general and remarkable effects on crystalline structure, physical properties, and photochemical activity. *J. Am. Chem. Soc.* **2015**, *137*, 3241-7. DOI
74. Tachikawa, T.; Majima, T. Single-molecule, single-particle fluorescence imaging of $TiO_2$-based photocatalytic reactions. *Chem. Soc. Rev.* **2010**, *39*, 4802-19. DOI PubMed
75. Gao, Y.; Wu, T.; Yang, C.; et al. Activity trends and mechanisms in peroxymonosulfate-assisted catalytic production of singlet oxygen over atomic metal-N-C catalysts. *Angew. Chem. Int. Ed. Engl.* **2021**, *60*, 22513-21. DOI PubMed
76. Sun, Y.; Guo, S.; Fan, L.; Cai, J.; Han, W.; Zhang, F. Molecular oxygen activation in photocatalysis: generation, detection and application. *Surf. Interface.* **2024**, *46*, 104033. DOI
77. Wang, Y.; Lin, Y.; He, S.; Wu, S.; Yang, C. Singlet oxygen: properties, generation, detection, and environmental applications. *J. Hazard. Mater.* **2024**, *461*, 132538. DOI
78. Cheng, J.; Wan, S.; Cao, S. Promoting solar-driven hydrogen peroxide production over thiazole-based conjugated polymers via generating and converting singlet oxygen. *Angew. Chem. Int. Ed. Engl.* **2023**, *62*, e202310476. DOI PubMed
79. Dimitrijevic, N. M.; Rozhkova, E.; Rajh, T. Dynamics of localized charges in dopamine-modified $TiO_2$ and their effect on the formation of reactive oxygen species. *J. Am. Chem. Soc.* **2009**, *131*, 2893-9. DOI PubMed
80. Li, J.; Liu, K.; Xue, J.; et al. CQDS preluded carbon-incorporated 3D burger-like hybrid ZnO enhanced visible-light-driven photocatalytic activity and mechanism implication. *J. Catal.* **2019**, *369*, 450-61. DOI
81. Wang, Q. Y.; Liu, J.; Cao, M.; et al. Aminal-linked porphyrinic covalent organic framework for rapid photocatalytic decontamination of mustard-gas simulant. *Angew. Chem. Int. Ed. Engl.* **2022**, *61*, e202207130. DOI
82. Wang, H.; Jiang, S.; Chen, S.; et al. Enhanced singlet oxygen generation in oxidized graphitic carbon nitride for organic synthesis. *Adv. Mater.* **2016**, *28*, 6940-5. DOI
83. Jiang, M.; Wang, Y.; Liu, H.; Yu, S.; Niu, K.; Xing, L. Construction of a novel pyrene-based two-dimensional supramolecular organic framework and the selective regulation of reactive oxygen species for photocatalysis. *J. Mater. Chem. A.* **2024**, *12*, 4752-60. DOI
84. Suleman, S.; Zhang, Y.; Qian, Y.; et al. Turning on singlet oxygen generation by outer-sphere microenvironment modulation in porphyrinic covalent organic frameworks for photocatalytic oxidation. *Angew. Chem. Int. Ed. Engl.* **2024**, *63*, e202314988. DOI
85. Keum, Y.; Kim, B.; Byun, A.; Park, J. Synthesis and photocatalytic properties of titanium-porphyrinic aerogels. *Angew. Chem. Int. Ed. Engl.* **2020**, *59*, 21591-6. DOI PubMed
86. Huang, T.; Tian, F.; Wen, Z.; Li, G.; Liang, Y.; Chen, R. Synergistic mediation of metallic bismuth and oxygen vacancy in Bi/$Bi_2WO_{6-x}$ to promote $^1O_2$ production for the photodegradation of bisphenol A and its analogues in water matrix. *J. Hazard. Mater.* **2021**, *403*, 123661. DOI PubMed
87. Long, R.; Huang, H.; Li, Y.; Song, L.; Xiong, Y. Palladium-based nanomaterials: a platform to produce reactive oxygen species for catalyzing oxidation reactions. *Adv. Mater.* **2015**, *27*, 7025-42. DOI PubMed
88. Li, X.; Wang, T.; Tao, X.; Qiu, G.; Li, C.; Li, B. Interfacial synergy of Pd sites and defective BiOBr for promoting the solar-driven selective oxidation of toluene. *J. Mater. Chem. A.* **2020**, *8*, 17657-69. DOI
89. Luo, L.; Zhang, T.; Wang, M.; Yun, R.; Xiang, X. Recent advances in heterogeneous photo-driven oxidation of organic molecules by reactive oxygen species. *ChemSusChem* **2020**, *13*, 5173-84. DOI PubMed
90. Bicalho, H. A.; Quezada-Novoa, V.; Howarth, A. J. Metal–organic frameworks for the generation of reactive oxygen species. *Chem. Phys. Rev.* **2021**, *2*, 041301. DOI
91. Waiskopf, N.; Ben-Shahar, Y.; Banin, U. Photocatalytic hybrid semiconductor-metal nanoparticles; from synergistic properties to emerging applications. *Adv. Mater.* **2018**, *30*, e1706697. DOI PubMed
92. Lee, S.; Bae, H. S.; Choi, W. Selective control and characteristics of water oxidation and dioxygen reduction in environmental photo(electro)catalytic systems. *Acc. Chem. Res.* **2023**, *56*, 867-77. DOI PubMed PMC
93. Jiang, Z.; Xu, X.; Ma, Y.; et al. Filling metal-organic framework mesopores with $TiO_2$ for $CO_2$ photoreduction. *Nature* **2020**, *586*, 549-54. DOI
94. Zhou, P.; Luo, M.; Guo, S. Optimizing the semiconductor-metal-single-atom interaction for photocatalytic reactivity. *Nat. Rev. Chem.* **2022**, *6*, 823-38. DOI PubMed
95. Ju, L.; Ma, Y.; Tan, X.; Kou, L. Controllable electrocatalytic to photocatalytic conversion in ferroelectric heterostructures. *J. Am. Chem. Soc.* **2023**, *145*, 26393-402. DOI
96. Xu, X.; Dai, S.; Xu, S.; Zhu, Q.; Li, Y. Efficient photocatalytic cleavage of lignin models by a soluble perylene diimide/carbon nitride S-scheme heterojunction. *Angew. Chem. Int. Ed. Engl.* **2023**, *62*, e202309066. DOI
97. Dey, A.; Pradhan, J.; Biswas, S.; Ahamed, R. F.; Biswas, K.; Maji, T. K. COF-topological quantum material nano-heterostructure for $CO_2$ to syngas production under visible light. *Angew. Chem. Int. Ed. Engl.* **2024**, *63*, e202315596. DOI PubMed
98. Yang, Y.; Jia, H.; Hu, N.; et al. Construction of gold/rhodium freestanding superstructures as antenna-reactor photocatalysts for plasmon-driven nitrogen fixation. *J. Am. Chem. Soc.* **2024**, *146*, 7734-42. DOI
99. Xu, Q.; Zhang, L.; Cheng, B.; Fan, J.; Yu, J. S-scheme heterojunction photocatalyst. *Chem* **2020**, *6*, 1543-59. DOI
100. He, J.; Chen, L.; Ding, D.; et al. Facile fabrication of novel $Cd_3(C_3N_3S_3)_2$/CdS porous composites and their photocatalytic performance for toluene selective oxidation under visible light irradiation. *Appl. Catal. B. Environ.* **2018**, *233*, 243-9. DOI
101. Tan, Y. X.; Chai, Z. M.; Wang, B. H.; et al. Boosted photocatalytic oxidation of toluene into benzaldehyde on $CdIn_2S_4$-CdS: synergetic effect of compact heterojunction and S-vacancy. *ACS. Catal.* **2021**, *11*, 2492-503. DOI

102. Gao, S.; Wang, B.; Chen, F.; et al. Confinement of $CsPbBr_3$ perovskite nanocrystals into extra-large-pore zeolite for efficient and stable photocatalytic hydrogen evolution. *Angew. Chem. Int. Ed. Engl.* **2024**, *63*, e202319996. DOI
103. Cortés-Villena, A.; Bellezza, D.; Cunha, C.; et al. Engineering metal halide perovskite nanocrystals with BODIPY dyes for photosensitization and photocatalytic applications. *J. Am. Chem. Soc.* **2024**, *146*, 14479-92. DOI PubMed PMC
104. Lee, J.; Kumar, A.; Tüysüz, H. Solar-light-driven photocatalytic oxidative coupling of phenol derivatives over bismuth-based porous metal halide perovskites. *Angew. Chem. Int. Ed. Engl.* **2024**, *63*, e202404496. DOI PubMed
105. Lopes, J. C.; Albero, J.; Sampaio, M. J.; Silva, C. G.; García, H.; Faria, J. L. Selective oxidative coupling of amines through light-activated bismuth halide perovskites. *ChemCatChem* **2024**, *16*, e202301432. DOI
106. Mondal, S.; Banerjee, S.; Bera, S.; et al. $CsPbBr_3$ perovskite polyhedral nanocrystal photocatalysts for decarboxylative alkylation via $C_{sp3}$–H bond activation of unactivated ethers. *ACS. Catal.* **2024**, *14*, 6633-43. DOI
107. Song, J.; Zhang, C.; Zhang, H.; et al. In situ growth of lead-free perovskite $Cs_2AgBiBr_6$ on a flexible ultrathin carbon nitride sheet for highly efficient photocatalytic benzylic $C(sp^3)$−H bond activation. *Chem. Eng. J.* **2023**, *453*, 139748. DOI
108. Bai, Z. J.; Mao, Y.; Wang, B. H.; et al. Tuning photocatalytic performance of $Cs_3Bi_2Br_9$ perovskite by g-$C_3N_4$ for $C(sp^3)$-H bond activation. *Nano. Res.* **2023**, *16*, 6104-12. DOI
109. Zhao, Y.; Dai, Y.; Wang, Q.; et al. Anions-exchange-induced efficient carrier transport at $CsPbBr_xCl_{3-x}/TiO_2$ interface for photocatalytic activation of $C(sp^3)$−H bond in toluene oxidation. *ChemCatChem* **2021**, *13*, 2592-8. DOI
110. Cui, Z.; Zhang, Q.; Fu, H.; et al. Composite of lead-free halide perovskite $Cs_3Bi_2Br_9$ with $TiO_2$ as an efficient photocatalyst for $C(sp^3)$ −H bond activation. *Appl. Catal. B. Environ.* **2023**, *333*, 122812. DOI
111. Zhou, B.; Fan, K.; Chong, Y.; et al. Modulating adsorption–redox sites and charge separation of $Cs_3Bi_2Br_{9-x}$@AgBr core–shell heterostructure for selective toluene photooxidation. *ACS. Energy. Lett.* **2024**, *9*, 1743-52. DOI
112. Chai, Z.; Wang, B.; Tan, Y.; et al. Enhanced photocatalytic activity for selective oxidation of toluene over cubic–hexagonal CdS phase junctions. *Ind. Eng. Chem. Res.* **2021**, *60*, 11106-16. DOI
113. Deng, J.; Xu, D.; Zhang, J.; et al. $Cs_3Bi_2Br_9$/BiOBr S-scheme heterojunction for selective oxidation of benzylic C-H bonds. *J. Mater. Sci. Technol.* **2024**, *180*, 150-9. DOI
114. Wongthep, S.; Pluengphon, P.; Tantraviwat, D.; et al. New visible-light-driven $Bi_2MoO_6/Cs_3Sb_2Br_9$ heterostructure for selective photocatalytic oxidation of toluene to benzaldehyde. *J. Colloid. Interface. Sci.* **2024**, *655*, 32-42. DOI
115. Cheng, C.; Zhang, J.; Zhu, B.; Liang, G.; Zhang, L.; Yu, J. Verifying the charge-transfer mechanism in S-scheme heterojunctions using femtosecond transient absorption spectroscopy. *Angew. Chem. Int. Ed. Engl.* **2023**, *62*, e202218688. DOI
116. Li, F.; Yue, X.; Liao, Y.; Qiao, L.; Lv, K.; Xiang, Q. Understanding the unique S-scheme charge migration in triazine/heptazine crystalline carbon nitride homojunction. *Nat. Commun.* **2023**, *14*, 3901. DOI PubMed PMC
117. Jiang, X.; Chen, Z.; Shu, Y.; et al. In-situ assembled S-scheme heterojunction of $CsPbBr_3$ nanocrystals and $W_{18}O_{49}$ ultrathin nanowires for enhanced bifunctional photocatalysis. *Appl. Catal. B. Environ.* **2024**, *348*, 123840. DOI
118. Bai, S.; Wang, L.; Li, Z.; Xiong, Y. Facet-engineered surface and interface design of photocatalytic materials. *Adv. Sci.* **2017**, *4*, 1600216. DOI PubMed PMC
119. Liu, G.; Yang, H. G.; Pan, J.; Yang, Y. Q.; Lu, G. Q.; Cheng, H. M. Titanium dioxide crystals with tailored facets. *Chem. Rev.* **2014**, *114*, 9559-612. DOI
120. Sajan, C. P.; Wageh, S.; Al-ghamdi, A. A.; Yu, J.; Cao, S. $TiO_2$ nanosheets with exposed {001} facets for photocatalytic applications. *Nano. Res.* **2016**, *9*, 3-27. DOI
121. Xiao, C.; Lu, B.; Xue, P.; et al. High-index-facet- and high-surface-energy nanocrystals of metals and metal oxides as highly efficient catalysts. *Joule* **2020**, *4*, 2562-98. DOI
122. Yang, X.; Li, X.; Zhang, B.; Liu, T.; Chen, Z. Facet-dependent $Bi_2MoO_6$ for highly efficient photocatalytic selective oxidation of $sp^3$ C–H bonds using $O_2$ as an oxidant. *Catal. Sci. Technol.* **2023**, *13*, 1996-2000. DOI
123. Li, C.; Gu, S.; Xiao, Y.; et al. Single-crystal oxygen-rich bismuth oxybromide nanosheets with highly exposed defective {10-1} facets for the selective oxidation of toluene under blue LED irradiation. *J. Colloid. Interface. Sci.* **2024**, *668*, 426-36. DOI PubMed
124. Zhou, G.; Lei, B.; Dong, F. Lewis acid sites in (110) facet-exposed BiOBr promote C–H activation and selective photocatalytic toluene oxidation. *ACS. Catal.* **2024**, *14*, 4791-8. DOI
125. Zhu, H.; Fu, Y.; Meng, F.; et al. Lead halide perovskite nanowire lasers with low lasing thresholds and high quality factors. *Nat. Mater.* **2015**, *14*, 636-42. DOI
126. Zhou, N.; Bekenstein, Y.; Eisler, C. N.; et al. Perovskite nanowire-block copolymer composites with digitally programmable polarization anisotropy. *Sci. Adv.* **2019**, *5*, eaav8141. DOI PubMed PMC
127. Zhang, G.; Liu, G.; Wang, L.; Irvine, J. T. Inorganic perovskite photocatalysts for solar energy utilization. *Chem. Soc. Rev.* **2016**, *45*, 5951-84. DOI
128. Wang, W.; Tadé, M. O.; Shao, Z. Research progress of perovskite materials in photocatalysis- and photovoltaics-related energy conversion and environmental treatment. *Chem. Soc. Rev.* **2015**, *44*, 5371-408. DOI PubMed
129. Katan, C.; Mercier, N.; Even, J. Quantum and dielectric confinement effects in lower-dimensional hybrid perovskite semiconductors. *Chem. Rev.* **2019**, *119*, 3140-92. DOI PubMed
130. Wang, H.; Liu, W.; He, X.; Zhang, P.; Zhang, X.; Xie, Y. An excitonic perspective on low-dimensional semiconductors for photocatalysis. *J. Am. Chem. Soc.* **2020**, *142*, 14007-22. DOI PubMed
131. Zhang, K.; Chen, H.; Liu, Y.; et al. Two-dimensional $Bi_2WxMo_{1-x}O_6$ solid solution nanosheets for enhanced photocatalytic toluene

oxidation to benzaldehyde. *Appl. Cataly. B. Environ.* **2022**, *315*, 121545. DOI

132. Bai, Z.; Xiong, J.; Mao, Y.; et al. Lead-free Dion-Jacobson layered double perovskite as a photocatalyst for toluene oxidation. *Cell. Rep. Phys. Sci.* **2023**, *4*, 101591. DOI
133. Mai, H.; Li, X.; Lu, J.; et al. Synthesis of layered lead-free perovskite nanocrystals with precise size and shape control and their photocatalytic activity. *J. Am. Chem. Soc.* **2023**, *145*, 17337-50. DOI
134. Dai, Y.; Poidevin, C.; Ochoa-Hernández, C.; Auer, A. A.; Tüysüz, H. A supported bismuth halide perovskite photocatalyst for selective aliphatic and aromatic C-H bond activation. *Angew. Chem. Int. Ed. Engl.* **2020**, *59*, 5788-96. DOI PubMed PMC
135. Zhang, H.; Zhou, Z.; Dong, Y.; Zhang, L.; Chen, H.; Kuang, D. Constructing a $Cs_3Sb_2Br_9$/g-$C_3N_4$ hybrid for photocatalytic aromatic C($sp^3$)-H bond activation. *Solar. RRL.* **2021**, *5*, 2100559. DOI
136. Yi, J.; Ke, S.; Lu, S.; et al. High-efficiency visible-light-driven oxidation of primary C-H bonds in toluene over a $CsPbBr_3$ perovskite supported by hierarchical $TiO_2$ nanoflakes. *Nanoscale* **2023**, *15*, 14584-94. DOI
137. Guo, Y.; Chen, J.; Zhao, Y.; Lou, Y. In-situ anchoring Pb-free $Cs_3Bi_2Br_9$@BiOBr quantum dots on $NH_x$-rich silica with enhanced blue emission and satisfactory stability for photocatalytic toluene oxidation. *ChemSusChem* **2022**, *15*, e202200793. DOI
138. Yu, B.; Zhang, S.; Wang, X. Helical Microporous nanorods assembled by polyoxometalate clusters for the photocatalytic oxidation of toluene. *Angew. Chem. Int. Ed. Engl.* **2021**, *60*, 17404-9. DOI
139. Liu, L.; Corma, A. Metal catalysts for heterogeneous catalysis: from single atoms to nanoclusters and nanoparticles. *Chem. Rev.* **2018**, *118*, 4981-5079. DOI PubMed PMC
140. Gao, C.; Low, J.; Long, R.; Kong, T.; Zhu, J.; Xiong, Y. Heterogeneous single-atom photocatalysts: fundamentals and applications. *Chem. Rev.* **2020**, *120*, 12175-216. DOI
141. Su, L.; Wang, P.; Ma, X.; Wang, J.; Zhan, S. Regulating local electron density of iron single sites by introducing nitrogen vacancies for efficient photo-fenton process. *Angew. Chem. Int. Ed. Engl.* **2021**, *60*, 21261-6. DOI PubMed
142. Liu, Y.; Sun, J.; Huang, H.; et al. Improving $CO_2$ photoconversion with ionic liquid and Co single atoms. *Nat. Commun.* **2023**, *14*, 1457. DOI PubMed PMC
143. Rocha, G. F. S. R.; da, S. M. A. R.; Rogolino, A.; et al. Carbon nitride based materials: more than just a support for single-atom catalysis. *Chem. Soc. Rev.* **2023**, *52*, 4878-932. DOI
144. Therrien, A. J.; Hensley, A. J. R.; Marcinkowski, M. D.; et al. An atomic-scale view of single-site Pt catalysis for low-temperature CO oxidation. *Nat. Catal.* **2018**, *1*, 192-8. DOI
145. Lu, Y.; Wang, J.; Yu, L.; et al. Identification of the active complex for CO oxidation over single-atom Ir-on-$MgAl_2O_4$ catalysts. *Nat. Catal.* **2019**, *2*, 149-56. DOI
146. Han, G. F.; Li, F.; Rykov, A. I.; et al. Abrading bulk metal into single atoms. *Nat. Nanotechnol.* **2022**, *17*, 403-7. DOI
147. Zhang, H.; Wei, J.; Dong, J.; et al. Efficient visible-light-driven carbon dioxide reduction by a single-atom implanted metal-organic framework. *Angew. Chem. Int. Ed. Engl.* **2016**, *55*, 14310-4. DOI PubMed
148. Dolgopolova, E. A.; Rice, A. M.; Martin, C. R.; Shustova, N. B. Photochemistry and photophysics of MOFs: steps towards MOF-based sensing enhancements. *Chem. Soc. Rev.* **2018**, *47*, 4710-28. DOI PubMed
149. Wang, Q.; Astruc, D. State of the art and prospects in metal-organic framework (MOF)-based and MOF-derived nanocatalysis. *Chem. Rev.* **2020**, *120*, 1438-511. DOI PubMed
150. Xu, C.; Pan, Y.; Wan, G.; et al. Turning on visible-light photocatalytic C-H oxidation over metal-organic frameworks by introducing metal-to-cluster charge transfer. *J. Am. Chem. Soc.* **2019**, *141*, 19110-7. DOI PubMed
151. da, S. M. A. R.; Tarakina, N. V.; Filho, J. B. G.; et al. Single-atoms on crystalline carbon nitrides for selective C-H photooxidation: a bridge to achieve homogeneous pathways in heterogeneous materials. *Adv. Mater.* **2023**, *35*, e2304152. DOI PubMed
152. Xie, J.; Li, X.; Guo, J.; et al. Highly selective oxidation of benzene to phenol with air at room temperature promoted by water. *Nat. Commun.* **2023**, *14*, 4431. DOI PubMed PMC
153. Bai, S.; Zhang, N.; Gao, C.; Xiong, Y. Defect engineering in photocatalytic materials. *Nano. Energy.* **2018**, *53*, 296-336. DOI
154. Pastor, E.; Sachs, M.; Selim, S.; Durrant, J. R.; Bakulin, A. A.; Walsh, A. Electronic defects in metal oxide photocatalysts. *Nat. Rev. Mater.* **2022**, *7*, 503-21. DOI
155. Wang, Z.; Xiao, M.; You, J.; Liu, G.; Wang, L. Defect engineering in photocatalysts and photoelectrodes: from small to big. *Acc. Mater. Res.* **2022**, *3*, 1127-36. DOI
156. Zafar, Z.; Yi, S.; Li, J.; et al. Recent development in defects engineered photocatalysts: an overview of the experimental and theoretical strategies. *Energy. Environ. Mater.* **2022**, *5*, 68-114. DOI
157. Zhang, N.; Gao, C.; Xiong, Y. Defect engineering: a versatile tool for tuning the activation of key molecules in photocatalytic reactions. *J. Energy. Chem.* **2019**, *37*, 43-57. DOI
158. Li, X.; Luo, L.; Guo, H.; et al. Tailoring bismuth defects in $Bi_2WO_6$ nanosheets for photocatalytic C–H activation. *J. Mater. Chem. A.* **2024**, *12*, 11841-7. DOI
159. Wang, H.; Cao, C.; Li, D.; et al. Achieving high selectivity in photocatalytic oxidation of toluene on amorphous BiOCl nanosheets coupled with $TiO_2$. *J. Am. Chem. Soc.* **2023**, *145*, 16852-61. DOI
160. Huang, H.; Verhaeghe, D.; Weng, B.; et al. Metal halide perovskite based heterojunction photocatalysts. *Angew. Chem. Int. Ed. Engl.* **2022**, *61*, e202203261. DOI
161. Xu, D.; Zhang, S. N.; Chen, J. S.; Li, X. H. Design of the synergistic rectifying interfaces in mott-schottky catalysts. *Chem. Rev.* **2023**, *123*, 1-30. DOI PubMed

162. Su, K.; Liu, H.; Zeng, B.; et al. Visible-light-driven selective oxidation of toluene into benzaldehyde over nitrogen-modified $Nb_2O_5$ nanomeshes. *ACS. Catal.* **2020**, *10*, 1324-33. DOI
163. Ding, Y. F.; Yin, S. F.; Cai, M. Q. Enhanced photocatalytic toluene oxidation performance induced by two types of cooperative fluorine doping in polymeric carbon nitride with the first-principles calculations. *J. Colloid. Interface. Sci.* **2023**, *630*, 452-9. DOI PubMed
164. Chen, R.; Shi, J. L.; Ma, Y.; Lin, G.; Lang, X.; Wang, C. Designed synthesis of a 2D Porphyrin-based $sp^2$ carbon-conjugated covalent organic framework for heterogeneous photocatalysis. *Angew. Chem. Int. Ed. Engl.* **2019**, *58*, 6430-4. DOI
165. Zhang, P.; Sui, X.; Wang, Y.; et al. Surface Ru-H bipyridine complexes-grafted $TiO_2$ nanohybrids for efficient photocatalytic $CO_2$ methanation. *J. Am. Chem. Soc.* **2023**, *145*, 5769-77. DOI
166. Zhang, Z.; Yang, Y.; Wang, Y.; et al. Revealing the A-site effect of lead-free $A_3Sb_2Br_9$ perovskite in photocatalytic C($sp^3$)-H bond activation. *Angew. Chem. Int. Ed. Engl.* **2020**, *59*, 18136-9. DOI
167. Fu, H.; Xu, Y.; Qiu, D.; et al. A library of rare earth oxide ultrathin nanowires with polymer-like behaviors. *Angew. Chem. Int. Ed. Engl.* **2022**, *61*, e202212251. DOI PubMed
168. Khoo, R. S. H.; Fiankor, C.; Yang, S.; et al. Postsynthetic modification of the nonanuclear node in a zirconium metal-organic framework for photocatalytic oxidation of hydrocarbons. *J. Am. Chem. Soc.* **2023**, *145*, 24052-60. DOI PubMed PMC
169. Zhang, Q.; An, B.; Lei, Y.; et al. $Cl_2^{\cdot-}$ mediates direct and selective conversion of inert C($sp^3$)-H bonds into aldehydes/ketones. *Angew. Chem. Int. Ed. Engl.* **2023**, *62*, e202304699. DOI PubMed
170. Zhang, H.; Liu, S.; Zheng, A.; et al. Enhanced charge transfer process and photocatalytic activity over a phosphonate-based MOF via amorphization strategy. *Angew. Chem. Int. Ed. Engl.* **2024**, *63*, e202400965. DOI
171. Yoshizawa, M.; Miyagi, S.; Kawano, M.; Ishiguro, K.; Fujita, M. Alkane oxidation via photochemical excitation of a self-assembled molecular cage. *J. Am. Chem. Soc.* **2004**, *126*, 9172-3. DOI
172. Furutani, Y.; Kandori, H.; Kawano, M.; Nakabayashi, K.; Yoshizawa, M.; Fujita, M. In situ spectroscopic, electrochemical, and theoretical studies of the photoinduced host-guest electron transfer that precedes unusual host-mediated alkane photooxidation. *J. Am. Chem. Soc.* **2009**, *131*, 4764-8. DOI PubMed
173. Gera, R.; Das, A.; Jha, A.; Dasgupta, J. Light-induced proton-coupled electron transfer inside a nanocage. *J. Am. Chem. Soc.* **2014**, *136*, 15909-12. DOI PubMed
174. Zhang, Z.; Liang, Y.; Huang, H.; et al. Stable and highly efficient photocatalysis with lead-free double-perovskite of $Cs_2AgBiBr_6$. *Angew. Chem. Int. Ed. Engl.* **2019**, *58*, 7263-7. DOI
175. Romani, L.; Speltini, A.; Ambrosio, F.; et al. Water-stable $DMASnBr_3$ lead-free perovskite for effective solar-driven photocatalysis. *Angew. Chem. Int. Ed. Engl.* **2021**, *60*, 3611-8. DOI
176. Zhou, P.; Chen, H.; Chao, Y.; et al. Single-atom Pt-$I_3$ sites on all-inorganic $Cs_2SnI_6$ perovskite for efficient photocatalytic hydrogen production. *Nat. Commun.* **2021**, *12*, 4412. DOI PubMed PMC
177. Wu, Y.; Wu, Q.; Zhang, Q.; et al. An organometal halide perovskite supported Pt single-atom photocatalyst for $H_2$ evolution. *Energy. Environ. Sci.* **2022**, *15*, 1271-81. DOI
178. Bai, Z.; Tian, S.; Zeng, T.; et al. $Cs_3Bi_2Br_9$ nanodots stabilized on defective BiOBr nanosheets by interfacial chemical bonding: modulated charge transfer for photocatalytic C($sp^3$)–H bond activation. *ACS. Catal.* **2022**, *12*, 15157-67. DOI
179. Dai, Y.; Tüysüz, H. Rapid acidic media growth of $Cs_3Bi_2Br_9$ halide perovskite platelets for photocatalytic toluene oxidation. *Solar. RRL.* **2021**, *5*, 2100265. DOI
180. Mu, C.; Lv, C.; Meng, X.; Sun, J.; Tong, Z.; Huang, K. In situ characterization techniques applied in photocatalysis: a review. *Adv. Mater. Interfaces.* **2023**, *10*, 2201842. DOI
181. Zhang, H.; Wang, Z.; Zhang, J.; Dai, K. Metal-sulfide-based heterojunction photocatalysts: principles, impact, applications, and in-situ characterization. *Chinese. J. Catal.* **2023**, *49*, 42-67. DOI
182. Bie, C.; Yu, H.; Cheng, B.; Ho, W.; Fan, J.; Yu, J. Design, fabrication, and mechanism of nitrogen-doped graphene-based photocatalyst. *Adv. Mater.* **2021**, *33*, e2003521. DOI
183. Shen, H.; Yang, M.; Hao, L.; Wang, J.; Strunk, J.; Sun, Z. Photocatalytic nitrogen reduction to ammonia: insights into the role of defect engineering in photocatalysts. *Nano. Res.* **2022**, *15*, 2773-809. DOI
184. Yang, W.; Prabhakar, R. R.; Tan, J.; Tilley, S. D.; Moon, J. Strategies for enhancing the photocurrent, photovoltage, and stability of photoelectrodes for photoelectrochemical water splitting. *Chem. Soc. Rev.* **2019**, *48*, 4979-5015. DOI PubMed
185. Bonke, S. A.; Risse, T.; Schnegg, A.; Brückner, A. In situ electron paramagnetic resonance spectroscopy for catalysis. *Nat. Rev. Method. Prime.* **2021**, *1*, 33. DOI
186. Zhao, Z. J.; Wu, T.; Xiong, C.; et al. Hydroxyl-mediated non-oxidative propane dehydrogenation over VO*x*/γ-$Al_2O_3$ catalysts with improved stability. *Angew. Chem. Int. Ed. Engl.* **2018**, *57*, 6791-5. DOI
187. Qi, Z.; Chen, L.; Zhang, S.; Su, J.; Somorjai, G. A. Mechanism of methanol decomposition over single-site $Pt_1/CeO_2$ catalyst: a DRIFTS study. *J. Am. Chem. Soc.* **2021**, *143*, 60-4. DOI
188. Wang, X.; Rosspeintner, A.; Ziarati, A.; Zhao, J.; Bürgi, T. Insight into the transient inactivation effect on $Au/TiO_2$ catalyst by in-situ DRIFT and UV-vis spectroscopy. *Nat. Commun.* **2022**, *13*, 5458. DOI PubMed PMC
189. Paul, R.; Das, R.; Das, N.; et al. Tweaking photo $CO_2$ reduction by altering lewis acidic sites in metalated-porous organic polymer for adjustable $H_2$/CO ratio in syngas production. *Angew. Chem. Int. Ed. Engl.* **2023**, *62*, e202311304. DOI
190. Li, Y.; Chen, B.; Liu, L.; Zhu, B.; Zhang, D. Water-resistance-based S-scheme heterojunction for deep mineralization of toluene.

*Angew. Chem. Int. Ed. Engl.* **2024**, *63*, e202319432. DOI

191. Zhou, E.; Wang, F.; Zhang, X.; Hui, Y.; Wang, Y. Cyanide-based covalent organic frameworks for enhanced overall photocatalytic hydrogen peroxide production. *Angew. Chem. Int. Ed. Engl.* **2024**, *63*, e202400999. DOI
192. Meunier, F. C. Pitfalls and benefits of in situ and operando diffuse reflectance FT-IR spectroscopy (DRIFTS) applied to catalytic reactions. *React. Chem. Eng.* **2016**, *1*, 134-41. DOI
193. Meunier, F. C. Hydrogenation of CO and $CO_2$: contributions of IR *operando* studies. *Catal. Today.* **2023**, *423*, 113863. DOI
194. Zaera, F. New advances in the use of infrared absorption spectroscopy for the characterization of heterogeneous catalytic reactions. *Chem. Soc. Rev.* **2014**, *43*, 7624-63. DOI PubMed
195. Duan, M.; Hu, C.; Li, H.; et al. Synergizing inter and intraband transitions in defective tungsten oxide for efficient photocatalytic alcohol dehydration to alkenes. *JACS. Au.* **2022**, *2*, 1160-8. DOI PubMed PMC
196. Wang, K.; Kong, X.; Xie, H.; Li, S.; Wang, M.; Jin, Z. In-situ XPS reveals the interfacial engineering of Co/Ce-BDC with graphdiyne ($C_nH_{2n-2}$) for effective photocatalytic $H_2$ evolution. *J. Alloys. Compd.* **2024**, *982*, 173757. DOI
197. Feng, N.; Wang, Q.; Zheng, A.; et al. Understanding the high photocatalytic activity of (B, Ag)-codoped $TiO_2$ under solar-light irradiation with XPS, solid-state NMR, and DFT calculations. *J. Am. Chem. Soc.* **2013**, *135*, 1607-16. DOI
198. Zhang, F.; Li, Y.; Ding, B.; Shao, G.; Li, N.; Zhang, P. Electrospinning photocatalysis meet in situ irradiated XPS: recent mechanisms advances and challenges. *Small* **2023**, *19*, e2303867. DOI
199. Xu, F.; Zhang, L.; Cheng, B.; Yu, J. Direct Z-scheme $TiO_2$/NiS core–shell hybrid nanofibers with enhanced photocatalytic $H_2$-production activity. *ACS. Sustain. Chem. Eng.* **2018**, *6*, 12291-8. DOI
200. Wang, L.; Li, Y.; Ai, Y.; et al. Tracking heterogeneous interface charge reverse separation in $SrTiO_3$/NiO/NiS nanofibers with in situ irradiation XPS. *Adv. Funct. Mater.* **2023**, *33*, 2306466. DOI
201. Wang, R.; Wang, Z.; Qiu, Z.; Wan, S.; Ding, J.; Zhong, Q. Nanoscale 2D g-$C_3N_4$ decorating 3D hierarchical architecture LDH for artificial photosynthesis and mechanism insight. *Chem. Eng. J.* **2022**, *448*, 137338. DOI
202. Zhang, N.; Xiong, Y. Dynamic characterization for artificial photosynthesis through in situ X-ray photoelectron spectroscopy. *Curr. Opin. Green. Sust.* **2023**, *41*, 100796. DOI
203. Oversteeg CH, Doan HQ, de Groot FM, Cuk T. In situ X-ray absorption spectroscopy of transition metal based water oxidation catalysts. *Chem. Soc. Rev.* **2017**, *46*, 102-25. DOI PubMed
204. Singh, J.; Lamberti, C.; van, B. J. A. Advanced X-ray absorption and emission spectroscopy: in situ catalytic studies. *Chem. Soc. Rev.* **2010**, *39*, 4754-66. DOI PubMed
205. Timoshenko, J.; Roldan, C. B. In situ/operando electrocatalyst characterization by X-ray absorption spectroscopy. *Chem. Rev.* **2021**, *121*, 882-961. DOI PubMed PMC
206. Lin, S. C.; Chang, C. C.; Chiu, S. Y.; et al. Operando time-resolved X-ray absorption spectroscopy reveals the chemical nature enabling highly selective $CO_2$ reduction. *Nat. Commun.* **2020**, *11*, 3525. DOI PubMed PMC
207. Samanta, B.; Morales-García, Á.; Illas, F.; et al. Challenges of modeling nanostructured materials for photocatalytic water splitting. *Chem. Soc. Rev.* **2022**, *51*, 3794-818. DOI
208. Ong, W. J.; Tan, L. L.; Ng, Y. H.; Yong, S. T.; Chai, S. P. Graphitic carbon nitride (g-$C_3N_4$)-based photocatalysts for artificial photosynthesis and environmental remediation: are we a step closer to achieving sustainability? *Chem. Rev.* **2016**, *116*, 7159-329. DOI PubMed
209. Majek, M.; Jacobi, W. A. Mechanistic perspectives on organic photoredox catalysis for aromatic substitutions. *Acc. Chem. Res.* **2016**, *49*, 2316-27. DOI PubMed
210. Wu, M.; Chen, S.; Xiang, W. Oxygen vacancy induced performance enhancement of toluene catalytic oxidation using $LaFeO_3$ perovskite oxides. *Chem. Eng. J.* **2020**, *387*, 124101. DOI
211. Wang, P.; Wang, J.; An, X.; et al. Generation of abundant defects in Mn-Co mixed oxides by a facile agar-gel method for highly efficient catalysis of total toluene oxidation. *Appl. Catal. B. Environ.* **2021**, *282*, 119560. DOI
212. Yang, W.; Sun, K.; Wan, J.; et al. Dual-site oxygen activation for enhanced photocatalytic aerobic oxidation by S-scheme $Ni_2P/Bi_3O_4$ Br-OVs heterojunction. *Chem. Eng. J.* **2023**, *452*, 139425. DOI
213. Qian, H.; Hou, Q.; Zhang, W.; et al. Construction of electron transport channels and oxygen adsorption sites to modulate reactive oxygen species for photocatalytic selective oxidation of 5-hydroxymethylfurfural to 2,5-diformylfuran. *Appl. Catal. B. Environ.* **2022**, *319*, 121907. DOI
214. Liu, L.; Jing, G.; Xu, C.; et al. Exceptional formaldehyde oxidation at room temperature on Co single-atom functionalized $TiO_2$ nanowires via highly effective $O_2$ activation. *Appl. Catal. B. Environ.* **2024**, *344*, 123634. DOI
215. DeCoste, J. B.; Weston, M. H.; Fuller, P. E.; et al. Metal-organic frameworks for oxygen storage. *Angew. Chem. Int. Ed. Engl.* **2014**, *53*, 14092-5. DOI
216. Murray, L. J.; Dinca, M.; Yano, J.; et al. Highly-selective and reversible $O_2$ binding in $Cr_3$(1,3,5-benzenetricarboxylate)$_2$. *J. Am. Chem. Soc.* **2010**, *132*, 7856-7. DOI PubMed
217. Popczun, E. J.; Tafen, D. N.; Natesakhawat, S.; et al. Temperature tunability in $Sr_{1-x}CaxFeO_{3-\delta}$ for reversible oxygen storage: a computational and experimental study. *J. Mater. Chem. A.* **2020**, *8*, 2602-12. DOI
218. Ma, J.; Li, X.; Zhang, C.; Ma, Q.; He, H. Novel $CeMn_aO_x$ catalyst for highly efficient catalytic decomposition of ozone. *Appl. Catal. B. Environ.* **2020**, *264*, 118498. DOI
219. Liu, H.; Fan, Z.; Sun, C.; et al. Improved activity and significant $SO_2$ tolerance of samarium modified $CeO_2$-$TiO_2$ catalyst for NO

selective catalytic reduction with $NH_3$. *Appl. Catal. B. Environ.* **2019**, *244*, 671-83. DOI

220. Li, X.; Mai, H.; Lu, J.; et al. Rational atom substitution to obtain efficient, lead-free photocatalytic perovskites assisted by machine learning and DFT calculations. *Angew. Chem. Int. Ed. Engl.* **2023**, *62*, e202315002. DOI
221. Masood, H.; Toe, C. Y.; Teoh, W. Y.; Sethu, V.; Amal, R. Machine learning for accelerated discovery of solar photocatalysts. *ACS. Catal.* **2019**, *9*, 11774-87. DOI
222. Ge, L.; Ke, Y.; Li, X. Machine learning integrated photocatalysis: progress and challenges. *Chem. Commun.* **2023**, *59*, 5795-806. DOI
223. Zhang, C.; Firestein, K. L.; Fernando, J. F. S.; Siriwardena, D.; von, T. J. E.; Golberg, D. Recent progress of in situ transmission electron microscopy for energy materials. *Adv. Mater.* **2020**, *32*, e1904094. DOI PubMed
224. Zhao, B.; Sun, M.; Chen, F.; et al. Unveiling the activity origin of iron nitride as catalytic material for efficient hydrogenation of $CO_2$ to $C_{2+}$ hydrocarbons. *Angew. Chem. Int. Ed. Engl.* **2021**, *60*, 4496-500. DOI
225. Twilton, J.; Le, C.; Zhang, P.; Shaw, M. H.; Evans, R. W.; Macmillan, D. W. C. The merger of transition metal and photocatalysis. *Nat. Rev. Chem.* **2017**, *1*, BFs415700170052. DOI
226. Qi, M.; Li, Z.; Zhang, Z.; Gao, Y.; Wang, Q. Controllable synthesis of $MnO_2$/iron mesh monolithic catalyst and its significant enhancement for toluene oxidation. *Chinese. Chem. Lett.* **2023**, *34*, 107437. DOI
227. Zhou, J.; Wang, Q.; Liu, H.; Bao, M.; Wang, J. VMoNb/$CeO_2$ as an efficient catalyst for the gas-phase selective oxidation of toluene to benzaldehyde. *Mol. Catal.* **2024**, *569*, 114570. DOI
228. Rawlings, A. J.; Diorazio, L. J.; Wills, M. C-N bond formation between alcohols and amines using an iron cyclopentadienone catalyst. *Org. Lett.* **2015**, *17*, 1086-9. DOI PubMed
229. Pazo-Carballo, C.; Blanco, E.; Camu, E.; et al. Theoretical and experimental study for cross-coupling aldol condensation over mono- and bimetallic UiO-66 nanocatalysts. *ACS. Appl. Nano. Mater.* **2023**, *6*, 5422-33. DOI
230. Suga, T.; Ukaji, Y. Nickel-catalyzed cross-electrophile coupling between benzyl alcohols and aryl halides assisted by titanium co-reductant. *Org. Lett.* **2018**, *20*, 7846-50. DOI PubMed

**Shiqin Gao**

Shiqin Gao is pursuing a PhD in inorganic chemistry at the State Key Laboratory of Inorganic Synthesis and Preparative Chemistry, Jilin University, China. His main research focuses on the exploitation and fabrication of novel zeolite-based nanomaterials for catalytic applications.

**Lisu Bai**

Lisu Bai received his bachelor's degree from Jilin University in 2024 and is currently a Ph.D. student under the supervision of Prof. Jihong Yu at Jilin University. His research interests lie in the design of host-guest assemblies based on zeolite and their applications in photocatalysis.

**Gan Tao**

Gan Tao received his B.S. and Ph. D. degrees from the College of Chemistry, Jilin University, in 2015 and 2020, respectively, under the supervision of Prof. Wenxiang Zhang and Prof. Gang Liu. He then conducted postdoctoral research at the Department of Chemistry, Tsinghua University, with Prof. Yadong Li and Prof. Dingsheng Wang. In 2023, he joined the Shanghai Synchrotron Radiation Facility, Chinese Academy of Sciences. His research interests focus on the synthesis, assembly, and catalytic applications of nanomaterials, clusters, and isolated single-atom sites, as well as related synchrotron radiation studies.

**Bolun Wang**

Bolun Wang received his Ph.D. degree from Jilin University in 2021 and is now a research assistant at the State Key Laboratory of Inorganic Synthesis and Preparative Chemistry, Jilin University. His research interest centers on designing syntheses of host-guest assemblies based on porous materials and their applications in optics, energy conversion, and other areas.